

**Development and Characterization of
Metal/Carbon Nanomaterial Composite Coating
Prepared by Electrodeposition Technique**

Thesis

Submitted in partial fulfillment of the requirement for degree of

DOCTOR OF PHILOSOPHY

by

K DIVYA BHARATHI

(Registration Number: 177104MT005)



**DEPARTMENT OF METALLURGICAL AND MATERIALS
ENGINEERING**

**NATIONAL INSTITUTE OF TECHNOLOGY KARNATAKA
SURATHKAL, MANGALORE – 575025**

OCTOBER, 2023

**Development and Characterization of
Metal/Carbon Nanomaterial Composite Coating
Prepared by Electrodeposition Technique**

Thesis

Submitted in partial fulfillment of the requirement for degree of

DOCTOR OF PHILOSOPHY

by

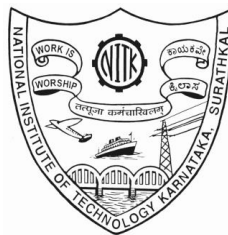
K DIVYA BHARATHI

(Registration Number: 177104MT005)

Under the Guidance of

Dr. MOHAMMED RIZWANUR RAHMAN

ASSOCIATE PROFESSOR



**DEPARTMENT OF METALLURGICAL AND MATERIALS
ENGINEERING**

NATIONAL INSTITUTE OF TECHNOLOGY KARNATAKA

SURATHKAL, MANGALORE – 575025

OCTOBER, 2023

DECLARATION

By the Ph.D. Research Scholar

I hereby declare that the Research Thesis entitled “**Development and Characterization Of Metal/Carbon Nanomaterial Composite Coating Prepared By Electrodeposition Technique**” which is being submitted to the National Institute of Technology Karnataka, Surathkal in partial fulfillment of the requirements for the award of the Degree of Doctor of Philosophy in Metallurgical and Materials Engineering, is a bonafide report of the research work carried out by me. The material contained in this Research Thesis has not been submitted to any university or Institution for the award of any degree.

.....

K DIVYA BHARATHI

Reg. NO.:177104MT005

Department of Metallurgical and Materials Engineering

Place: **NITK - Surathkal**

Date:

CERTIFICATE

This is to certify that the Research Thesis entitled “**Development And Characterization Of Metal/Carbon Nanomaterial Composite Coating Prepared By Electrodeposition Technique**” submitted by Mrs. K DIVYA BHARATHI (Register Number: 177104MT005), as the record of the research work carried out by her, is accepted as the Research Thesis submission in partial fulfillment of the requirements for the award of the Degree of Doctor of Philosophy in Metallurgical and Materials Engineering.

Research Guide

Dr. Mohammad Rizwanur Rahman

Associate professor

Department of Metallurgical and Materials Engineering

NITK, Surathkal

Chairman-DRPC

Department of Metallurgical and Materials Engineering

NITK, Surathkal

***This thesis is dedicated to my beloved parents and my husband
for their endless love, support and encouragement***

ACKNOWLEDGEMENT

The research work, which is presented in this dissertation, is more of teamwork and I would like to thank many who have contributed their time and energy for the study.

First and foremost, I am grateful to my advisor **Dr. Mohammad Rizwanur Rahman**, Department of Metallurgical and Materials Engineering, National Institute of Technology Karnataka, Surathkal (NITK) as he consistently kept me motivated and instilled good thoughts not only for research but for life as well. His constant and enthusiastic support throughout is the root cause for the research work to see its logical end.

I wish to thank all the members of the Research Program Assessment Committee (RPAC) including **Dr. Jagannatha Nayak**, Professor, Department of Metallurgical and Materials Engineering, NITK, Surathkal and **Dr. M. R. Ramesh**, Professor, Department of Mechanical Engineering, NITK, Surathkal for their unbiased appreciation, support and suggestions provided during the various discussions which has certainly helped in the betterment of this research work.

I am thankful to **Dr. Ravishankar K S**, Head & DRPC Chairman, Department of Metallurgical and Materials Engineering, NITK, Surathkal. I extend my gratitude to the authorities of NITK, Surathkal, Staff and Research scholars of Department of Metallurgical and Materials Engineering for their help which ensured the satisfactory progress of my research work.

I would like to express my deepest gratitude to my parents, **K Venkat Swamy** and **K. Prameela**, who were always there to support me in my endeavors. I am grateful to my husband **J. Shameek Nandan** for his encouragement and support throughout the journey. Their confidence in my ability to succeed was the impetus I needed to move forward and confront obstacles.

My special thanks to staff of Metallurgical and Materials Engineering Department for their kind support in executing the experiments. Then, I would like to thank all my

research group members **Mohanraj G T, Aruna M N, Arun Kumar D S, K V Swaroop and Mohammed Mohiuddin** for their continuous support. I would like to thank my dearest friends always supported me to carry out my research work.

I acknowledge with gratitude to all others who have helped directly or indirectly in completing my thesis successfully. Finally, I am greatly indebted to almighty, all my family members, relatives and teachers who supported me throughout my life, providing me the opportunity and made me reach this stage.

K Divya Bharathi

ABSTRACT

The carbon nanomaterials (CNMs) such as CNTs and graphene have shown remarkable utility and immense potential for high performance engineering materials due to its exceptional physical properties at nanoscale. CNTs and graphene have incredible scope in preparing nanocomposites and promising substitutes for many applications. In this study, Metal/Carbon nanomaterial composites (Cu/CNT and Zn/GO) were successfully prepared by reinforcing carbon nanomaterials (CNT/GO) using electrodeposition technique. Samples were characterized by using the scratch test, X-ray diffractometry (XRD), Transmission electron microscope (TEM), Field emission scanning electron microscopy (FESEM), Energy-dispersive X-ray spectroscopy (EDS), and Raman spectroscopy to confirm the presence and homogeneity of carbon nanomaterials (CNT/GO) in the metal matrix (Cu/Zn).

The Cu/CNT nanocomposites are prepared by varying the diameter and concentrations of the CNT and are characterized by tensile test, hardness and corrosion and heat transfer rate. Maximum 24.63% and 47% higher tensile strength and hardness were observed for 450 mgL⁻¹ compared to copper coating. Higher tensile strength in the composite coated on the Cu substrate signifies that good bonding between the Cu and CNT at atomic level is achieved by using electrodeposition technique. The Cu/MWCNT composite coatings have lower corrosion rate than pure Cu coating because the CNTs provide physical barrier to the corrosion medium. The overall heat transfer phenomena of Cu/CNT nanocomposite due to the preferential deposition of CNTs in the Cu matrix. The heat transfer rate is optimized and increased by 41.08% and 46.91% in natural and forced convection respectively compared to pure Cu coating. The reason is attributed to the better alignment, the optimum concentration of CNT in the composite, and the homogeneously placed CNTs network in the composite.

The aim of Zn/GO nanocomposites is to report cohesion strength and impact strength with respect to temperature using electrodeposition technique. The Zn/GO composite focused on the evaluation of cohesion strength using a scratch test from RT to 350 °C, and residual stresses of the hybrid films deposited on the stainless steel substrate using different concentrations of GO and varying GO/surfactant ratios. Scratch tests revealed that Zn/GO hybrid films produced using 40 mgL⁻¹ GO had 70.54% increase in cohesion strength (L_{C1}) when compared to pure Zn films

deposited with 30 minutes of coating time at a ratio of 1:2 GO:CTAB. In this study investigates the impact performance of Zn/GO nanocomposites under various gun pressure (2 bar, 2.5 bar, 3 bar, 3.5 bar and 4 bar) and temperature (100°C, 200°C and 300°C) conditions using Split Hopkinson Pressure Bar experiments (SHPB). These findings motivated exploratory research for determining the behavior of structures in defence, aerospace, and nuclear power plant sectors subjected to the combined fire and impact. The Zn/GO nanocomposites were prepared using 40 mgL⁻¹ concentration of GO through electrodeposition technique and characterized to maximum stress and toughness measurements. Test results show that the true stress–true strain responses are sensitive to the gun pressure and temperature. Zn/GO composite shows that 10.7% increase in compressive strength and 22.9% higher toughness at 4 bar in comparison with uncoated sample. The presences of few layered GO flakes in the coating which makes composite stronger and tougher. Because of this reason, considerable improvement in high maximum stress and higher toughness observed under high impact loading in Zn/GO composite. The maximum stress and toughness of Zn/GO nanocomposites declines with temperature from RT to 300°C. The residual stresses were measured by using the X-Ray diffraction (XRD) - $\sin^2\psi$ method using Co-K α radiation. The magnitude of the residual stress diminishes as the GO concentration increases in films due to the effect of the kinetic movement of particles while deposition. Overall, experimentally measured cohesion strength values of Zn/GO hybrid films have correlated with residual stress values.

TABLE OF CONTENTS

CONTENTS	PAGE NO.
ACKNOWLEDGEMENT	i-ii
ABSTRACT	iii
TABLE OF CONTENTS	v
LIST OF FIGURES	ix
LIST OF TABLES	xiv
CHAPTER 1 INTRODUCTION	1-13
1.1 Composite	1
1.2 Carbon Nanomaterials	2
1.2.1 Graphene	3
1.2.2 Carbon Nanotubes (CNTs)	3
1.3 Nano Composite	4
1.3.1 Powder technology	6
1.3.2 Melting and solidification	7
1.3.3 Thermal spraying	8
1.3.4 Electrochemical deposition	9
1.3.5 Other techniques	11
1.4 Challenges in preparation of MMCs	13
1.5 Outline of thesis	13

CHAPTER 2	LITERATURE REVIEW	15-33
2.1	Fabrication of Metal/Carbon Nanostructure Composite	15
2.2	Mechanical properties of Metal/Carbon Nano structure Composite	16
2.3	Mechanical properties of Cu/CNT Composite	16
2.3.1	Tensile test	19
2.3.2	Hardness	19
2.3.3	Corrosion study	21
2.3.4	Thermal conductivity	22
2.4	Mechanical properties of Zn/GO composite	24
2.4.1	Cohesion strength	24
2.4.2	Impact strength	27
2.4.3	Residual stress	30
2.5	Research Gap	32
2.6	Objectives	33
CHAPTER 3	METHODOLOGY	34-44
3.1	Materials	34
3.2	Electrodeposition Technique	34
3.3	Characterization of Cu/CNT Composites	37
3.3.1	Microstructural Study	37
3.3.2	X-Ray Diffraction	37
3.3.3	Tensile test	38
3.3.4	Micro hardness	38
3.3.5	Corrosion study	39
3.3.6	Thermal experiments	39

3.4	Characterization of Zn/GO Composites	41
3.4.1	Scratch tests	41
3.4.2	Impact tests	42
3.4.3	Residual stresses	44
CHAPTER 4	RESULTS AND DISCUSSION	45-76
4.1	Cu/CNT nano composites	45
4.1.1	TEM and FESEM micrographs	45
4.1.2	SEM Micrographs	45
4.1.3	XRD	49
4.1.4	Tensile test	49
4.1.5	Micro hardness test	51
4.1.6	Corrosion study	52
4.1.6.1	AC-impedance measurements	52
4.1.6.2	Tafel polarization studies	54
4.1.7	Heat transfer rate experiments	55
4.1.7.1	Experiments using Cu fins	55
4.1.7.2	Experiments using Cu Pipe	57
4.2	Zn/GO nano composites	60
4.2.1	FESEM Micrographs	60
4.2.2	XRD	61
4.2.3	Raman spectroscopy	62
4.2.4	Scratch test results	64
4.2.5	Impact strength	70
4.2.5.1	Deformation under varying pressure	70
4.2.5.2	Deformation under varying temperature	73

	4.2.5.3 Microstructural study of the Zn/GO coating after impact	74
	4.2.6 Residual stresses	76
CHAPTER	5 CONCLUSIONS AND SCOPE OF FUTURE WORK	79-92
	5.1 Conclusions	79
	5.2 Scope of future work	80
	LIST OF PUBLICATIONS	81
	REFERENCES	82
	BIO-DATA	92

LIST OF FIGURES

Fig. No.	Description	Page No.
1.1	List of publications on polymer/metal/ceramic matrix composites during 1997–2020 (Iris Carneiro and Sonia Simoes, 2021)	2
1.2	Lattice thermal conductivity of SWCNTs at various diameters, (Inset) cross-sectional view of atomic structure of SWCNT (Zhou et al. 2015)	4
1.3	Flowchart of various processing techniques for preparation of Metal matrix composites (Ashutosh singh et al., 2017)	6
1.4	Schematic diagram of metal/CNMs nanocomposites preparation through powder technology technique	7
1.5	Schematic diagram of metal composites preparation through infiltration technique	8
1.6	Schematic diagram of Metal/CNMs composite preparation through thermal spray technique	9
1.7	Schematic view of deposition process of (a) electrodeposition and (b) electroless deposition techniques	10
2.1	(a) A typical tensile stress – strain curve for the as- deposited CNT/Cu nano composite sample as comparison with that of a pure Cu sample (b) SEM micrographs of textured fracture morphology in Cu/CNT nano composite	17
2.2	Tensile Stress-Strain curve of (a) Pure Ni, Ni/SWCNT and Ni/MWCNT composites (b) pure copper and Cu/CNT composites with outside diameter of CNT	19
2.3	Effect of CNT volume fraction on the hardness of Cu/CNT Nano composite	20
2.4	Variation of the corrosion rate (mass loss) with immersion time in 3.5wt% NaCl solution	21

2.5	Relative density and Thermal conductivity of CNT/Cu composites versus CNT volume fraction	23
2.6	(a) Schematic diagram of the thermal conductivity measurement setup and an optical image of the Pt heater (inset) (b) Thermal conductivity (W/m-K) of CNT-Cu composites Vs. concentration of CNT (mgL^{-1}) in electrolyte	24
2.7	Friction force and load force as a function of scratch length for (a) Ta_xO_y (b) ZnO- Ta_xO_y coatings on Ti alloy along with Scratch starting position	25
2.8	The friction coefficient of the nickel/GO composite coatings under the different concentrations of GO (0.1 ~ 0.4 g/L)	26
2.9	(a) Penetration process of the composite and the pure Cu sample at different times at 3 km/s. (b) Final penetration morphology at 100 ps of 4 km/s and (c) 5 km/s. Atoms are colored by structure types. The spall length is defined by the distance of graphene and lower Cu matrix surface. A, B, C, and D corresponds to the beginning, maximum, recover and final states of the spall length, respectively	28
2.10	(a) Strength Vs. Fiber volume fraction (b) Stress-strain curves of GFRP and matrix under impact loading (strain rate $\sim 10^3\text{s}^{-1}$)	29
2.11	(a) Setup of specimen heating from the two thermocouples located in the specimen (b) Compressive Stress-strain curves of an AlSi-PE abradable from room temperature to 360 °C for a strain rate of 1200 s^{-1}	30
2.12	Residual stresses of WC-Co coating on different substrates	31
3.1	The schematic diagram of electrodeposition technique setup and the cross sectional view of Cu fins and Cu pipe samples	35
3.2	Schematic diagram of setup of electrodeposition technique along with the cross sectional view of samples	36

3.3	(a) ASTM standard (E8-EM) Tensile Sample dimensions, mm. (b) Prepared tensile test samples	38
3.4	Schematic diagrams of setup of the Heat transfer using (a) Cu fins (b) Cu pipe in axial & transverse direction along with original images	40
3.5	Schematic arrangement of SHPB experiment setup	43
4.1	(a) FESEM image of SWCNT, TEM micrographs of (b) MWCNT1 and (c) MWCNT2	45
4.2	SEM images of Cu/MWCNT2 (a) 150 mgL ⁻¹ , (b) 300 mgL ⁻¹ , (c) 450 mgL ⁻¹ , (d) 600 mgL ⁻¹ , and (e) 750 mgL ⁻¹	46
4.3	The FESEM micrographs of (a) Pure Cu, (b) Cu/SWCNT, (c) Cu/MWCNT1 and (d) Cu/MWCNT2 at 300 mgL ⁻¹ concentration at same deposition parameters	47
4.4	FESEM images of cross section view of Cu/MWCNT1 coating (a) coating thickness (b) CNTs alignment in Cu matrix (c) Schematic view of CNT deposition	48
4.5	Representative XRD profiles of Cu and Cu/MWCNT2 composite	49
4.6	Stress strain curve of pure Cu and different concentrations of Cu/MWCNT composites at 150 mgL ⁻¹ , 300 mgL ⁻¹ and 450 mgL ⁻¹	50
4.7	The Microhardness values variation with content of MWCNT in electrolyte	51
4.8	(a) Nyquist plots (b) log (Freq/Hz) vs. log Z/ohm Bode plot of a pure copper coating and Cu/CNT samples in 3.5wt%NaCl solution	53
4.9	Equivalent circuits for curve fitting of Pure Cu and Cu/CNT composites	54
4.10	Tafel polarisation plots of pure Cu and Cu/MWCNT coatings	54
4.11	The cooling rate curves of Cu, SWCNT, MWCNT1 and MWCNT 2 coated on copper pipe (a) without fan and (b) with fan	56

4.12	The heat transfer rate curves of Cu/MWCNT2 at different concentrations of (a) 150 mgL ⁻¹ , (b) 300 mgL ⁻¹ , (c) 450 mgL ⁻¹ , (d) 600 mgL ⁻¹ and (e) 750 mgL ⁻¹ coated on copper pipe without fan and with fan	58
4.13	The Q_{CNT}/Q_{Cu} values of Cu/MWCNT2 coatings at various concentrations of CNT in natural and forced convection	58
4.14	Schematic diagram of Cu/MWCNT2 composite at (a) 150 mgL ⁻¹ , (b) 450 mgL ⁻¹ concentrations of CNT (c) 750 mgL ⁻¹ , CNT-CNT contact region and its thermal conduction mechanism	59
4.15	FESEM micrographs of (a) Pure Zn and (b) Zn/GO nanocomposites of 4 mgL ⁻¹ GO with 1:2 of GO:CTAB	60
4.16	EDS Spectra of Zn/GO composite along with elements with micrograph image	61
4.17	X-Ray Diffraction profiles of (a) pure GO (b) pure Zn coating and Zn/GO nanocomposites at various concentrations of GO and 1:2 of GO:CTAB	61
4.18	The diffraction peak shift of Zn/GO composite at various concentrations of GO	62
4.19	Raman spectrums of (a) pure GO and (b) Zn/GO composite coatings	63
4.20	(a) Frictional force during progressive scratch on Zn/GO nanocomposite of 4 mgL ⁻¹ GO with 10 min coating time (b) inset in (a) showing area of no flaking and chipping (c) Macrograph of 5 mm length of scratch (d) Optical image of coating cracks in the scratch track at 200X	64
4.21	L_C values of Pure Zn and Zn/GO composites of GO concentration of 4 mgL ⁻¹ , 8 mgL ⁻¹ , 20 mgL ⁻¹ and 40 mgL ⁻¹ with (a) 1:1 (b) 1:2 ratio of GO:CTAB	65
4.22	The critical load (L_c) values for Zn/GO composites with different GO concentration and 1:2 ratio of GO and CTAB at RT, 100°C, 200°C, 300°C & 350°C	67

4.23	Curves of coefficient of friction with an increase of Scratch length for Zn/GO composites of increasing GO concentration with 1:1 & 1:2 ratio of GO:CTAB of coating time of 30 minutes	68
4.24	Coefficient of Friction variation with (a) coating time and (b) temperature at 40 mgL ⁻¹ concentration of GO	69
4.25	True stress-true strain plots obtained from uncoated and Zn/GO coated stainless steel samples at various pressures	71
4.26	Strain rate vs. time plots obtained from uncoated and Zn/GO coated stainless steel samples at various pressures	73
4.27	The true stress-true strain plots of Zn/GO coated samples at gun pressure of (a) 2bar (b) 3bar and (c) 4bar respectively by varying the temperature	74
4.28	The (a) visual picture and (b) microstructure of Zn/GO coating on stainless steel after SHPB experiment	75
4.29	The FESEM microstructures of (a) unimpacted (b) impacted stainless steel (c) Zn/GO coated stainless steel (d) at 300°C samples after the impact pressure of 4bar	76

LIST OF TABLES

Table No.	Description	Page No.
1.1	Physical properties of CNT and graphene nano materials	5
2.1	Tensile properties obtained of the pure copper and Cu/CNT composite	19
2.2	The Hardness of CNT/Cu composite by different group of researchers	20
2.3	Summary of studies on corrosion properties that used CNT	22
2.4	Summary of studies on Thermal conductivity that used CNT	24
3.1	Deposition parameters of Cu/CNT composites	35
3.2	Composition and Deposition parameters of Zn/GO composites	37
4.1	FESEM-EDS data of (a) Cu/SWCNT, (b) Cu/MWCNT1 and (c) Cu/MWCNT2 nanocomposites	48
4.2	Tensile Strength values of pure Cu and different concentrations of Cu/MWCNT nano composites	50
4.3	Hardness values of pure Cu and different concentrations of Cu/MWCNT composites	52
4.4	Electrochemical AC impedance studies of pure Cu and Cu/MWCNT	53
4.5	Corrosion current density and corrosion potential of pure Cu and Cu-MWCNTs composite coating obtained from Tafel Polarization studies in 3.5%NaCl Solution	55
4.6	The heat transfer rate values of Cu, SWCNT, MWCNT 1 and MWCNT2 composites	56

4.7	The critical load (L_{C1}) values for Zn/GO composites with different GO concentration, time and ratio of surfactant	66
4.8	The L_C values for Zn/GO composites with different GO concentration and 1:2 ratio of GO and CTAB	67
4.9	The maximum stress and toughness values for uncoated and Zn/GO coated samples under various pressures	72
4.10	The maximum stress values of Zn/GO coated and uncoated stain less steel samples	75
4.11	Residual stress values of Zn/GO composites coatings at various GO concentrations	78

CHAPTER 1

INTRODUCTION

1.1 Composite

In today's society, there is an increase in demand for materials with a variety of property characteristics such as high strength, high electrical and thermal conductivity, toughness, and lightweight etc. Most of the metals and alloys were unable to provide the properties in a single material together, prompting a paradigm shift in the direction of composite materials. In the wide range of applications, high strength materials with lightweight are great on the priority list in the modern era. The design of materials with better specific physical properties helps to use the material in specific applications. In coming advanced composites, it looks possible to improve the physical property of the composite to meet the demand of modern era.

Composites are broadly classified into three categories according to their matrix: (a) metal matrix composites (MMC's), (b) polymer matrix composites (PMC's), and (c) ceramic matrix composites (CMC's). In last 23 years, as per survey, the polymer matrix composites (PMC's) have received a larger number of studies in comparison to MMC's and CMC's, due to their easy processing techniques and their potential in several engineering applications (Ashutosh et al. 2017) as shown in Figure 1.1. However, MMCs are of particular interest because they are used in a variety of applications such as power tools, engines, aircraft brake pads, piston systems, and crank shafts, primarily to improve performance such as scratch resistance, thermal conductivity, with reduced weight (Rawal and Al 2001; Rohatgi 1991). The matrix in MMCs, typically offers high modulus, low/high density, thermal/electrical conductivity, etc. and transfers the loads by holding the reinforcement results the composite with improved characteristics. Whereas the reinforcement in the matrix provides strength, stiffness, impact, resistant to corrosion or other physical properties depending upon the reinforced material physical properties. The reinforcements can be soft, hard, particulate, fibrous or continuous form and improves the

composite physical properties and are used depending on the applications. The incorporating h-BN into polymer/matrix enhances the thermal conductivity (Lin et al. 2014). Hard reinforcements strengthen the soft matrix into stronger composite such as the addition of Al_2O_3 and SiC to the epoxy resin results in a stronger composite than with polyester resin matrix (Rajesh et al. 2014).

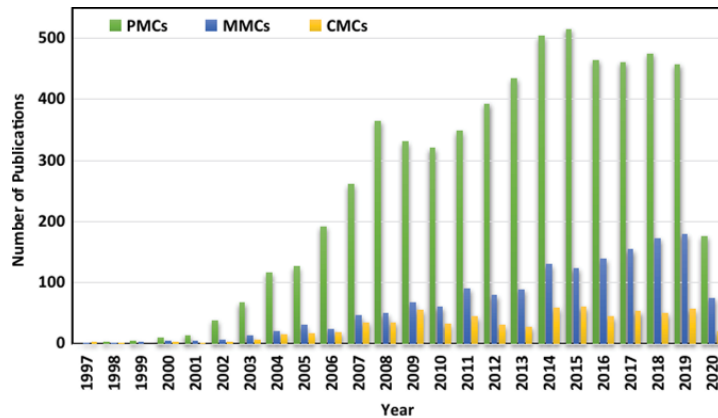


Figure 1.1: List of publications on polymer/metal/ceramic matrix composites during 1997–2020 (Iris Carneiro and Sonia Simoes, 2021)

1.2 Carbon Nano Materials

Carbon has been one of main element which forms strong bonds compare to other materials in various forms due to its special arrangement of electrons in the outer most shell. Carbon has different allotropes due to existence of hybridization in its orbital and categorized based on their dimensionalities and shape. There are mainly 3 types of allotropes of carbon at nanoscale which are (1) Fullerene (0-D, sp^2), (2) Carbon nanotubes (1-D, sp^2 (sp)), (3) Graphene and its derivatives (2-D, sp^2).

Carbon based nano materials includes CNTs, graphene and its derivatives and fullerenes. The carbon nanomaterials (CNMs) have shown remarkable utility and immense potential for high performance engineering materials due to its exceptional physical properties at nanoscale. The CNMs provides an important means for making advanced composite materials with metals. Out of these the CNTs and graphene have been discussed due to their incredible scope in preparing nanocomposites and promising substitutes for many applications.

1.2.1 Graphene

Graphene is a single layer of carbon atoms organized in hexagonal shaped lattice formed by sp^2 -bonded carbon atoms that boost outstanding mechanical and electronic properties. It is considered to be strongest material and widely used as a precursor for the synthesis of other carbon nano materials. Graphite is oxidized and exfoliated to form graphene oxide (GO) which is laced with oxygen containing functional groups. Bulk GO, is cheaper and easier to manufacture than graphene. GO can easily mixed in water or different organic solvents due to its hydrophilic nature and enhance physical properties of composite materials.

1.2.2 Carbon nanotubes (CNTs)

CNTs are graphene sheets rolled into a cylindrical nano structure that contains one layer of graphene is called single walled carbon nanotube (SWCNT) or however when multi-layer of graphene is rolled in a cylindrical shape is called multi walled carbon nanotubes (MWCNT). Different types of CNTs are categorized as single walled nanotubes (SWCNTs), double walled nanotubes (DWCNT) and multiwall nanotubes (MWCNTs). The CNTs are extensively used as reinforcement material in metal matrix composites to improve its physical properties as well as weight reduction. The characteristic of a CNT can differ with varying lengths, diameters, chirality and number of walls. These above parameters play an important role in defining the properties of CNTs. For example, SWCNT has thermal conductivity upto $6000 \text{ Wm}^{-1}\text{K}^{-1}$ and MWCNT has upto $\sim 3000\text{-}3500 \text{ Wm}^{-1}\text{K}^{-1}$. In Fig. 1.2 shows dependence of lattice thermal conductivity on diameter and chirality of SWCNTs. In this, the dotted line displays the thermal conductivity of graphene. The inset shows cross sectional view of atomic structure of SWCNT at various diameters. It is reported that the chirality (3,3) and diameter 4.07 \AA have the higher thermal conductivity of $14353.14 \text{ Wm}^{-1}\text{K}^{-1}$. While $3578.39 \text{ Wm}^{-1}\text{K}^{-1}$ is displayed with chirality (8,8) and diameter 10.85 \AA . Compared to graphene, the thermal conductivity of SWCNT (2,2) and SWCNT (2,1) is significantly lower (Yue et al. 2015).

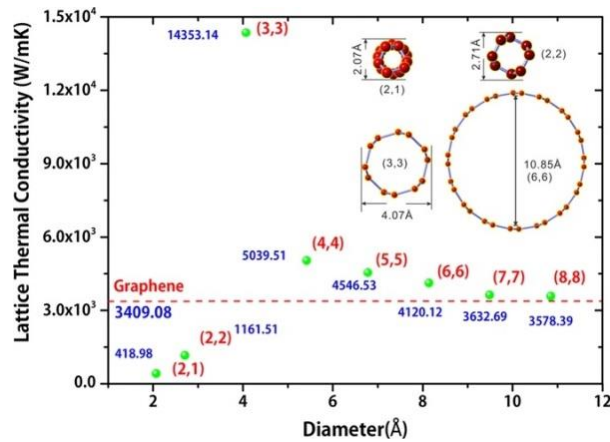


Figure 1.2: Lattice thermal conductivity of SWCNTs at various diameters, (Inset) cross-sectional view of atomic structure of SWCNT (Zhou et al. 2015)

1.3 Nano Composite

Nanomaterials have brought numerous important developments and support to fill new technological needs. A number of important milestones have been marked in the field of the development of nanomaterials such as colloidal crystals (nanocrystals), nanoparticles, nanorods, nanobelts, nanotubes, nanowires, superlattices, etc. (Patzke et al. 2002). The unique feature of small size and large specific surface area of nanoparticles as a result these nano materials exhibit exotic physical and chemical properties that differ from bulk materials. Because of the enhanced properties of nanomaterials, several researchers have incorporated nanosized materials in bulk to enhance the physical properties of engineering materials, and these materials are called **nanocomposites**. For example, incorporating of graphene oxide into Ni matrix by electrodeposition technique improved the tribological properties of nanocomposite.

The discoveries of carbon nanotubes (CNT) and graphene, revolutionized research in the field of carbon nanomaterials (CNMs) reinforced composites. The carbon nanomaterials has extraordinary properties like elastic modulus, tensile strength, thermal/electrical conductivities (as listed in Table 1.1) due to special structural arrangement of carbon atom and stable at nanoscale (Treacy et al. 1996; Salvetat et al. 1999; Berber et al. 2000).

Table 1.1: Physical properties of CNT and graphene nano materials

Properties	CNT	Graphene
Density (gcm^{-3})	1.8	2.26
Elastic Modulus (GPa)	~ 300-1000	1000-2000
Thermal conductivity ($\text{Wm}^{-1}\text{K}^{-1}$)	3000-6000	1-4000
Resistivity ($\Omega \text{ cm}$)	$10^{-7}\sim 10^{-8}$	0.2×10^{-3}

Because of these extraordinary physical properties, researchers have focused on fabricating nanocomposites with carbon nanomaterials (CNMs) as reinforcement in polymer/ceramic/metals. The combination of metal/CNMs will result a better physical property because CNMs has higher thermal, electrical, mechanical and tribological properties. For example CNT has unique thermal conductivity characteristics such as thermal conductivity in axial and transverse direction is around $3000 \text{ Wm}^{-1}\text{K}^{-1}$ and $1\text{-}2 \text{ Wm}^{-1}\text{K}^{-1}$ respectively. Another example, graphene or graphene oxide has high impact strength with the combination of metal because the bilayer or few layer of graphene is much harder than diamond due to its honeycomb structure arrangement of carbon (Slingerland Janet, 2015; Cellini et al. 2018) Since CNMs shows a wide range of physical property, it gives benefit to scientists to play around with different combination of metal/CNMs composite which can be fabricated/prepared using several techniques to achieve suitable and superior physical property of composite for different engineering applications.

The MMCs with carbon nanomaterials (CNMs) can be prepared by several techniques as shown in Fig. 1.3. These techniques are mostly categorized into five groups (1) powder metallurgy technique, (2) melting and solidification (3) Thermal spray (4) Electrochemical deposition and (5) Other techniques such as molecular level mixing, sputtering technique, vapor deposition etc. These techniques are explained in detailed in the following section.

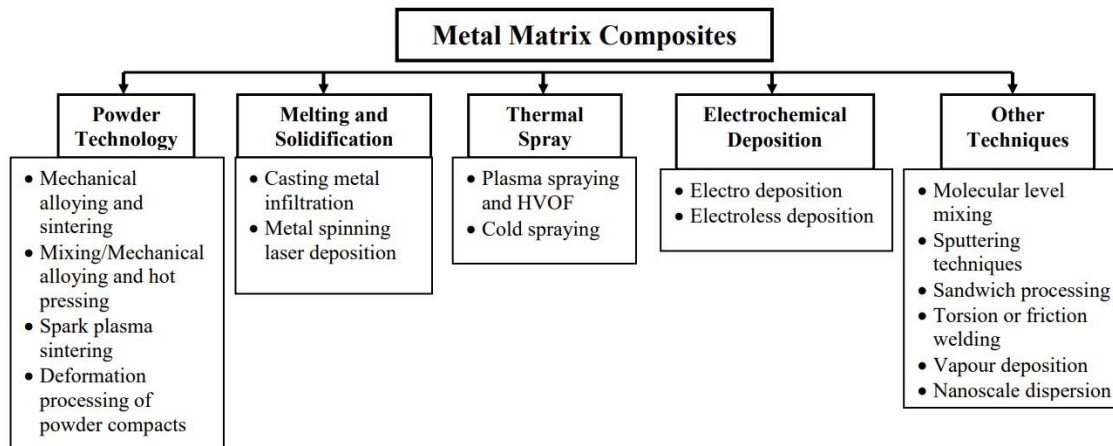


Figure 1.3: Flowchart of various processing techniques for preparation of Metal matrix composites (Ashutosh singh et al., 2017)

1.3.1. Powder technology

Powder technology involves the mixing of metal powders with other CNMs at different compositions which are then cold/hot compacted and sintered to produce solid dense metal/CNMs composites. The process begins with planetary ball milling in which the weighted CNMs and metal powders were mixed using stainless steel balls in a stainless-steel vial and performed under pure vacuum/inert atmosphere to protect from oxidation. Milling is performed to establish decrease in the particle size of powders and thus improve the homogenization of CNMs. By cold or hot pressing, the well-amalgamated metal and CNMs powders were compressed to green cylindrical compacts at room temperature using a cylindrical punch die arrangement. Then followed by vacuum or inert gas sintering (Li et al. 2018; Muxi et al. 2018) at just below the melting point of metal temperatures or plasma sintering (Cheng et al. 2017; Tian et al. 2016) to incorporate the particles and enhance the properties of the produced final composite. The entire process is depicted schematically in Fig. 1.4. Several parameters govern this process, including time period of milling, milling pressure, grain diameter, compaction pressure, sintering temperature, and time (Van Trinha et al. 2011; Delavari et. al. 1970). Dense composites with uniform carbon nanomaterial (CNM) dispersion are produced by carefully selecting the process parameters.

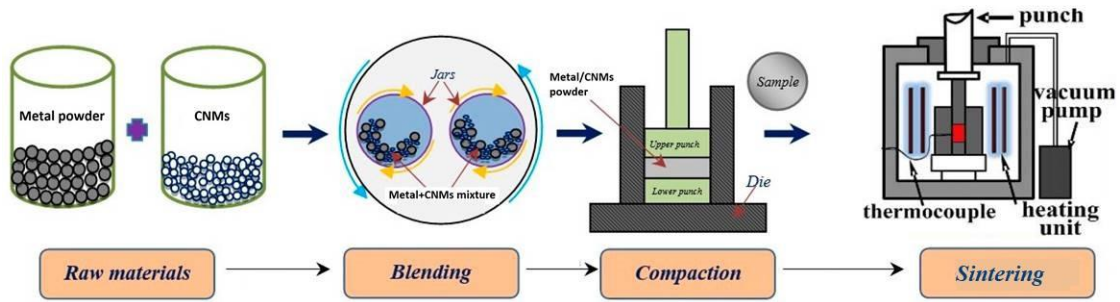


Figure 1.4: Schematic diagram of metal/CNMs nanocomposites preparation through powder technology technique

1.3.2 Melting and solidification

Melting and solidification also called as liquid metal infiltration which is another technique of preparing nanocomposites. Infiltration is a liquid-state fabrication technique, in which a porous preform (reinforcement such as CNTs or graphene or graphene oxide) is impregnated in a molten metal, which occupies the pores between the dispersed-phase inclusions. This process can be divided into several stages, such as (1) placing the preform in a metal die, (2) supplying molten metal to the die, (3) evacuation of the die chamber, and (4) pressurizing the melt chamber by an inert gas.

In this technique, the porous medium is first dispersed with reinforcement (CNMs) by casting method porous preform is prepared. After inserting the preform into the die, liquid metal is injected into the narrow crevices between the CNMs which are arranged in the preform to hold them in place. As the liquid enters between the reinforcement during infiltration, it cools and then solidifies to produce composites as shown in Fig. 1.5 (Zhou et al. 2007; Yang and Schaller et al. 2004). Metal infiltration consists of injecting the molten metal through a porous preform under a nitrogen atmosphere in a pressure less state without any aid of vacuum is called pressure less metal infiltration process. When an externally pressure is applied to get better bonding between the metal and CNMs, the process is called pressure infiltration. The pressure less infiltration process is a spontaneous infiltration of a molten metal into a preform through electromagnetic and centrifugal forces. This method is primarily used for the preparing the Mg/Al-based

composites due to their low melting points (650/660°C). This method is expensive because it uses molten metal, so it difficult for preparing nanocomposites with higher melting point metal. The variables like interfiber spacing, infiltration pressure, infiltration casting speed, metal superheat temperature and undesirable interfacial reactions are governing the evolution of high quality metal/CNMs composites.

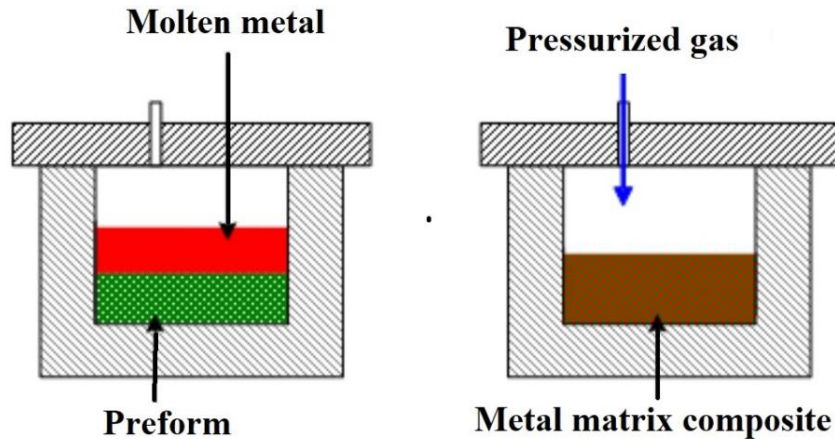


Figure 1.5: Schematic diagram of metal composites preparation through infiltration technique

1.3.3 Thermal spraying

Thermal spraying is a one of the coating process to fabricate metal matrix nanocomposites. In this technique, the metal and CNMs particles mixed together using ball milling techniques and the pass to the high pressure/temperature gun to sprayed onto a substrate in the form of micrometer size coatings. Cold or hot spraying constructs the complete Metal/CNMs structure layer by layer, by the sprayed particles as shown in Fig. 1.6. In the cold spray technique, the sprayed material (metal and CNMs) is converted into fine powder and particles are accelerated to very high speed by carrier gas forced through a converging or diverging type nozzle. Upon impact, solid particles with sufficient kinetic energy deform plastically and bond mechanically on the substrate to form a coating. The critical velocity desirable to form bonding depends on the material property/type of CNMs, powder size. However, in case of cold spray technique it is difficult to get appropriate bonding strength with certain substrates.

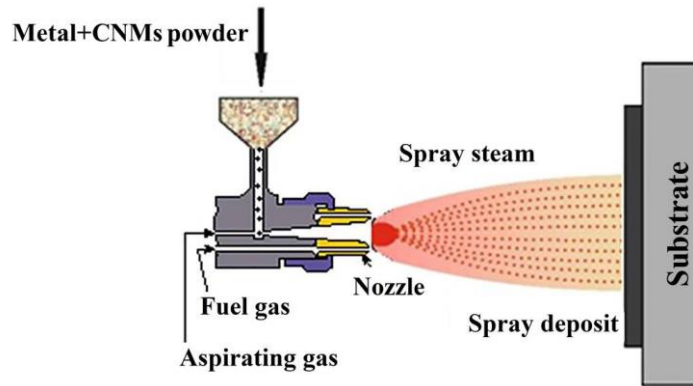


Figure 1.6: Schematic diagram of Metal/CNMs composite preparation through thermal spray technique

Whereas, in hot thermal spraying technique the electric arc discharge is generally used as source of energy to melt the metal and CNMs. To create the composite layer, molten metal (metal and CNMs) is sprayed at high speed onto the substrate using the pressure of high heat gas. Feed material type, gas composition and flow rate, energy input, torch-offset distance, and substrate material are all important process variables in hot spray technique (Fauchais 2004; Burndt et al. 1996). During the hot thermal sprays, CNMs are exposed to high temperatures and high velocity oxygen flow (HVOF), resulting in the damage of CNMs structure and losses its valuable physical properties. In both the above techniques the cost of equipment and skilled labor requirement which is the main drawback of this technique in produce cost effective metal/CNMs composite.

1.3.4 Electrochemical deposition

Electrochemical deposition has emerged as an efficient technique to produce MMCs using nanomaterials. This process can be categorized into two groups such as (1) Electrodeposition (2) Electroless deposition.

In electrodeposition technique, the nanocomposites are produced on conductive substrate surface by electrochemical reduction of metal ions from an electrolyte as shown in Fig. 1.7 (a). The coating thickness depends on based on the current and the time of electroplating. This fabrication technique can produce high quality MMCs with a uniform distribution of CNMs in a metal matrix. For example, Chai et al. (2008) and Wang et al.

(2017) developed Metal/CNMs composites and reported a three to five times increment in yield strength of nanocomposites compared to pure metal by using this technique. They discovered that the bond among the metal and CNMs remained together even after the tensile experiment. These findings suggest that, the electrodeposition process is capable of producing nanocomposites with exceptional interfacial bonding properties caused by atomic level metal ion deposition on substrate in electrolyte solution.

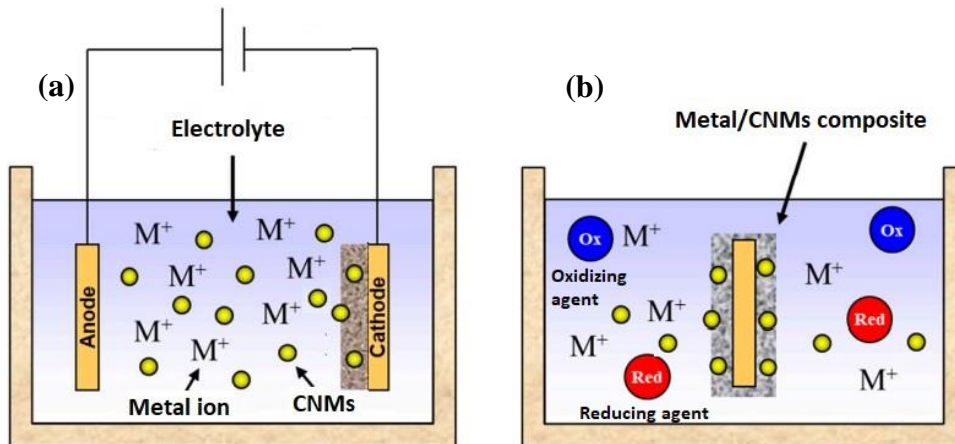


Figure 1.7: Schematic view of deposition process of (a) electrodeposition and (b) electroless deposition techniques

Electroless deposition is another important technique for producing metal nanocomposites. It involves the chemical reduction of metal ions in an aqueous solution and the subsequent deposition of metal/CNMs without the use of an external electrical energy source in order to deposit a coating. The schematic view of the electroless deposition technique has shown in Fig. 1.7 (b). The process involves dipping the substrate in a water solution containing metal salts, oxidizing agent and reducing agents. The powerful reducing agents in the deposition bath ex. formaldehyde, sodium borohydride, sodium hypophosphite, hydrogen peroxide, and ascorbic acid have negative standard potentials that drive the deposition process. The driving force behind electron exchange is the standard electrode potential of the metal and reducing agent. Activators (Ag, Au and Pd nano particles) accelerate the deposition by acting as a catalytic seed on the substrate surface for the final electroless deposition bath metal. During the activation,

the Ag/Au/Pd nanoparticles located at the CNTs/GO surface and these particles are the catalytic nuclei where the metal coating will be deposited (Muench 2021; García-Aguirre et al. 2015). A homogeneous layer of metal deposited on a catalytic surface by the reaction of a complex compound and chemical reducing agents.

1.3.5 Other techniques

In addition to the aforementioned well known conventional methods, some other techniques have emerged which have proven to be beneficial in avoiding agglomerations and homogeneity in the metal matrix. Some of them are discussed further down.

1.3.5.1 Molecular level mixing

Molecular level mixing process is proposed as a novel fabrication technique for the production of metal/CNMs composite powders. This method produces composite powder and then followed by sintering to get the metal/CNMs composites. In this process, the CNMs are first mixed with an acid solution for functionalization of CNMs by carboxyl groups. After the acid treatments, the CNMs washed with distilled water by filtering. The functionalized CNMs are dried at 80°C in vacuum oven for 3-4 hours. The purified CNMs were dispersed in distilled water by sonication. The CNMs solution is mixed with metal salt solution and sonicated for 3-4 hours. The CNMs metal anion precursor is then obtained, after which drying, calcination, and reductions are performed to produce the composite powder. This fabrication method prevents the agglomerations and enhances the adhesion between metal and CNMs. Because of these advantages, the properties of metal/CNMs composites can be improved and observed higher than that of pure metal (Hwang et al. 2013; Lim et al. 2010).

1.3.5.2. Sputtering technique

Sputtering is a technique of producing thin coatings by the phenomenon of sputtering and used for developing metal/CNMs composites by depositing metal over CNMs. This process involves ejecting metal particles from the target and impact energetically onto a substrate at room temperature in ambient conditions. The entire range from high energy

ballistic impact to low energy thermalized motion is accessible by changing the background gas pressure (Tran et al. 2020; Huang et al. 2006). This method is used to deposit the different metals on CNMs. According to reports, some elements exhibit strong interactions with the CNMs while others exhibit poor interfacial bonding. The availability of many process parameters such as sputtering gas, temperature, substrate material, type of the target material that control sputter deposition make it a complex process.

1.3.5.3. Sandwich processing

This technique employs the layers of CNMs and metal are organized one on the other and compacted under high pressure. Wang et al. (2021) have fabricated the Cu/CNT nanocomposite by sandwich processing method using Cu foil and CNT. Hong et al. (2017) have prepared the Au/graphene oxide/Ag sandwich structure coating. The process demonstrates better quality bonding between the matrix and the reinforcement in the composites. Nevertheless, this method is deemed ineffective due to CNT agglomeration at grain boundaries.

1.3.5.4. Vapor deposition

This technique can be divided into two types (1) Physical vapor deposition (PVD) and Chemical vapor deposition (CVD). This method usually employed to obtain composite coatings or powders. The PVD coating also known as thin film coating, is a process in which a solid material is vaporized in a vacuum and deposited onto the surface. CVD is a process in which the substrate is exposed to one or more volatile precursors, which react or decompose on the surface of the substrate to produce the desired thin film deposit. This method has been employed for growing CNMs on Si and Al substrates which have shown improved mechanical properties (Zhang et al. 2007). But these techniques are not preferable for the synthesis of bulk nano composites.

1.4 Challenges in preparation of MMCs

The preparation of MMCs using the powder technology, thermal spray, melting and solidification, sputtering, vapour deposition etc. may damage the carbon nanostructure materials (CNMs) or agglomerated CNMs in the matrix. Currently, there are a number of challenges associated with the production of MMCs using CNMs, including achieving a satisfactory dispersion of CNMs in metal matrix while maintaining a cost effective processing route. However, overcoming challenges with CNMs wetting and agglomeration have thus far prevented effective processing of carbon nanotube composites via cold melting and electrochemical deposition methods. These techniques are attractive methods for the manufacture of these composites, with better homogenous reinforcement and very less damage to CNMs structure also ability of preparing net shape components easily and cheaply. Because of the ability to form a better homogeneous filler in a matrix, CNMs very much used in recent application to achieve a better choice than the any other nano materials.

1.5 Outline of the thesis

In the present work, initially, the received carbon nano materials (CNTs and GO) are subjected to the dispersion using CTAB surfactant. After getting uniform and well dispersed CNMs solution, metal/CNMs composites are fabricated by electrodeposition technique. In this thesis, we have prepared two types of nanocomposites i.e., Cu/CNT (Cu Substrate) and Zn/GO (Stainless Steel Substrate). The morphology of Cu/CNT and Zn/GO samples are characterized using the TEM, and FESEM techniques. However, the presence of CNMs (CNTs and GO) in the Cu/CNT and Zn/GO composites are confirmed by XRD and Raman experiments respectively. The Cu/CNT composites have been characterized by heat rate transfer, tensile, hardness and corrosion. For the Zn/GO composites, the strain rate, cohesion strength and residual stresses measurements have been calculated. All the characterizations of both composites were measured and compared with pure metal coated samples. The thesis has been presented in five chapters

Chapter 1 introduces an overview of carbon nanomaterials (CNMs) and its properties with respect to mechanical, electrical and thermal conductivity. This chapter also, introduces the composite preparation method and the advantage of each method and challenges to get homogeneous dispersion of CNMs. In each method we focused on preparation of CNT/GO metal composites.

Chapter 2 gives a detailed review of the published articles which are relevant to the present study. The literature review presented mainly includes on the characterization of Cu/CNT and Zn/GO composites and improvement in the physical properties of composites with respect to the pure metal coatings. Based on the available literature and research gap, the broad objectives of the present research work were decided.

Chapter 3 describes the methodology which includes material selection, selection of electrode for electrodeposition, surface treatment of material, dispersion of MWCNTs, and experimental procedure for the fabrication of Cu/CNT and Zn/GO composites. Further, characterization techniques for fabricated Cu/CNT and Zn/GO are discussed.

Chapter 4 comprises the results and discussion of characterization studies of fabricated Cu/CNTs (on Cu Substrate) and Zn/GO (on Stainless steel Substrate) nano composites by reinforcing carbon nanomaterials through TEM, FESEM, XRD and Raman Spectroscopy. Then the heat transfer rate experiment, tensile, hardness and corrosion properties measured for Cu/CNT composites. For the Zn/GO composites, the strain rate using split hopkinson pressure bar (SHPB) equipment, cohesion strength and residual stresses measurements have been calculated.

Chapter 5 presents the conclusions drawn from the results obtained in this research work and the future scope of work is also enlisted. The list of references is shown at the end of the dissertation.

CHAPTER 2

LITERATURE REVIEW

This study mainly aims to produce and characterize the metal/CNMs nanocomposites with a family of graphenal materials such as SWCNT, MWCNT and GO. The detailed literature review of published research articles related to characterization studies of metal/CNMs nano composites was reported. This chapter presents the earlier work related to heat transfer rate, tensile, hardness and corrosion using carbon nanomaterials at room temperature in Cu/CNT composites. Whereas in Zn/GO composites, strain rate, cohesion strength and residual measurements were reviewed by various investigators.

2.1 Fabrication of Metal/Carbon Nanostructure Composite

The electrochemical methods are more economical and easy in processing and also produce homogeneous matrix without much damage of CNMs nano structure compare to other techniques. It means the pristine CNTs and GO will preserve its original properties by reinforcing in the Cu/CNT and Zn/GO composites. Among the various composite preparation methods, a simple electrodeposition method is an excellent technique which is used to deposit the Cu/CNT and Zn/GO composite coatings for the production of metal matrix nanocomposite coatings. The most important advantage of this electrodeposition technique is low cost with industrial applicability. Arai et al. (2007) have used surfactant to disperse the CNTs in the electrolyte, in reduction of the grain size the CNTs plays important role because of its large surface area. Cu/CNT composite coating obtained from the electrolyte with moderate CNT concentration 0.12g/L show increment in mechanical properties than pure Cu coating. Md Ali et al. (2021) prepared Graphene/Graphene oxide reinforced aluminum composites and observed improvement in mechanical properties. This improvement in composites is because of the hindrances to the movement of dislocation caused by Graphene/Graphene oxide present in the metal matrix. In this electrodeposition technique by using electric current, the metal ions and positively charged CNMs were deposited on cathode depending on their carrying charge. The morphology of deposition is very much dependent on current density. It is reported

by several researchers that at lower current densities, metal ions ($\text{Cu}^{2+}/\text{Zn}^{2+}$) and CNMs both were co-deposited on cathode. As a result smooth and well dispersed CNMs in the metal matrix were observed because of during deposition process, sufficient nucleation time is required to form a better surface. Whereas at higher current densities, the large amount of metals were deposited on the cathode surface with bumpy features and dendrite morphology.

2.2 Mechanical properties of Metal/Carbon Nano structure Composite

Carbon nano materials (CNMs) improves the mechanical properties, however is has been extremely difficult to turn this potential into a method for practical structural materials. This research demonstrates the excellent performance of graphene in preventing the impact failure and promoting the damage self-healing. In either case, the resulting mechanical properties will depend strongly on the stress transfer between matrix and reinforcement. Transfer of the stress strongly depends on the bonding between matrix and the reinforcement. Sometimes the chemical bond and sometimes only physical van der Waals bond is observed between the matrix and reinforcement. It is obvious to have better stress transfer in chemical bonding. Another factor on which stress transfer depends is the critical reinforcement length (L_c), which is necessary for effective transfer of stress. Critical length of the reinforcement depends on filler diameter d , filler tensile strength σ_f and on the reinforcement matrix bond strength τ_c according to $L_c = (\sigma_f d/2 \tau_c)$ (Wang et al. 2004) (L_c/d ratio is called aspect ratio). The average length of carbon nanotube is much higher than the critical length hence the transfer of the load will be significant and therefore, it is expected to have better mechanical properties in the composite.

2.3 Mechanical properties of Cu/CNT Composite

2.3.1 Tensile test

The addition of small amount of CNT to metals enhances the strength and stiffness of metal/CNT composites. Electrochemical deposition method is used in which coating is deposited from an electrolyte of ions onto a conducting substrate. By this method, uniform distribution of CNTs in copper matrix can be achieved. Chai et al. (2008)

prepared the Cu/CNT composites through this method. The reports have shown that the five times increment in yield strength for Cu/CNT nanocomposites compared to the pure Cu as shown in Figure 2.1a. They have observed that the bonding between the Cu and CNTs existed even after the experiment.

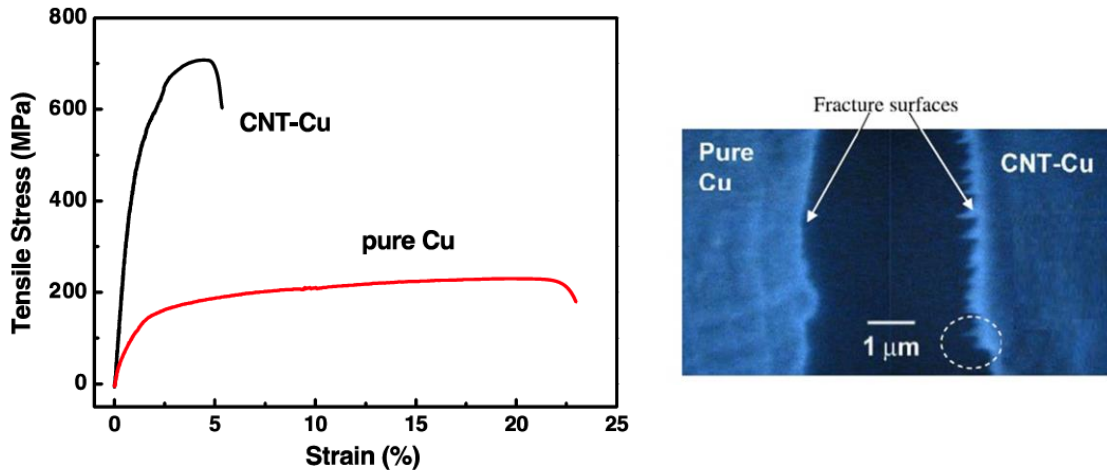


Figure 2.1: (a) A typical tensile stress – strain curve for the as- deposited CNT/Cu nano composite sample as comparison with that of a pure Cu sample (b) SEM micrographs of textured fracture morphology in Cu/CNT nano composite

Figure 2.1b shows that the fracture nature of the pure Cu coating and Cu/CNT nano composite. The composite appear to be significantly different from pure copper. The fracture surface of the Cu/CNT nano composite is characterized by textured deformation, while pure copper does not have textured morphology, means no separation between Cu and CNT can be identified in composite fracture. This means that after deformation, Cu and CNT still maintain good interfacial bonding.

The results clearly say that electrodeposition technique has the ability to produce nano composite with excellent interfacial bonding characteristics due to an atomic level deposition of Cu in aqueous electrolyte. All the available literatures on Cu/CNT composites have concluded that the addition of CNTs shows a significant improvement of the tensile properties of the copper. Daoush et al. (2009) have reported that yield strength of the composite has been increased to 341.2 MPa for 15 vol. % of CNT addition, which is 2.85 times higher than the unreinforced Cu at the cost of ductility.

However, the elastic modulus of the composites has improved to the maximum value of 105.9 GPa for 20 vol. % CNT, which is almost double that of the pure Cu. Chai et al. (2008) prepared Cu/CNT composites and reported high tensile properties by the electrochemical co-deposition. They have reported the yield and ultimate strength of 420 MPa and 710 MPa respectively in the composites which are 5 times and 3 times more than that of pure Cu respectively. They also reported that the addition of CNTs lowers the ductility. However, the ductility values were decreased 2.5% with addition of 5vol% CNT to Cu matrix which is reported by Daoush et al. (2009). The Cu/CNT (vol.10%) composites fabricated by Kim et al. showed the increase of the yield strength by 160 % and an increase of the elastic modulus by almost 100% compared to pure copper (Kim et al. 2006).

In 2013, Chu et al. synthesized the CNT/Cu composite by powder technology route, and they observed that the yield strength of Cu/CNT composite with 10 vol% CNTs, is up to 278 MPa which is 65 % of pure copper. This enhancement in the properties was attributed to the uniform dispersion of the CNT in the copper matrix. Y. Sun et al. (2007) tested stress-strain curves of pure nickel, MWCNT-reinforced nickel composite (Ni/MWCNT), as well as SWCNT-reinforced nickel composite (Ni/SWCNT) are represented in Figure 2.2 (a). The ultimate strengths of the as-deposited pure nickel, Ni/MWCNT and Ni/SWCNT were found to be 625 MPa, 1715 MPa and 1997 MPa respectively, which are higher strengths than that of pure nickel. The good reinforcement of CNTs in metal matrices is attributed to the good interfacial bonding as well as to the stiffer nature of the matrices (Sun et al. 2007).

A similar comparative study was conducted for the effect of outer diameter (OD) of CNTs by Sun et al. (2009). The key results are summarized in Figure 2.2 (b). As the OD decreases, there are more and more strengthening effects from CNTs. A comparison of tensile properties obtained of the pure copper and Cu/CNT composite are shown in Table 2.1. It is clear that tensile strength properties are good for Cu/CNT composite compared to pure copper which are obtained from the extensive literature survey.

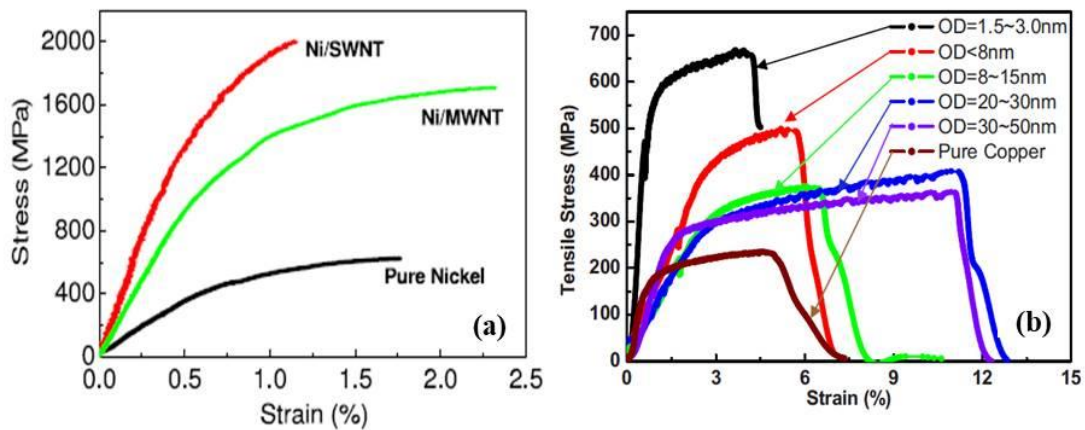


Figure 2.2: Tensile Stress-Strain curve of (a) Pure Ni, Ni/SWCNT and Ni/MWCNT composites (b) pure copper and Cu/CNT composites with outside diameter of CNT

Table 2.1: Tensile properties obtained of the pure copper and Cu/CNT composite

Author	Year	Mechanical Property	
		With CNT	Without CNT
Kim, K. T. et al.	2007	Yield strength = 455 MPa Young's modulus =138GPa	Yield strength = 150MPa Young's modulus =100GPa
Chai, G et al.	2008	Yield strength = 420 MPa Tensile strength = 710 MPa	Yield strength = 75 MPa Tensile strength = 230 MPa
Y. Sun & Q. Chen	2009	with 15 vol.% CNT, Yield strength = 670MPa	Yield strength = 230MPa
Li Y-H. et al.	2007	Yield Strength = 132 GPa Tensile Strength = 361 MPa	Yield Strength = 117 GPa Tensile Strength = 334 MPa
Daoush,W. M.et al.	2009	Yield strength = 350 MPa Young's modulus = 105 GPa	Yield strength = 120MPa Young's modulus = 51.6 GPa

2.3.2 Hardness

Similar to tensile properties, reports on Cu/CNT composites conclude that hardness of the composites increases up to a critical volume fraction and decreases with the further increment in CNT. Tu et al. (2001) have concluded that optimum vol. % of CNT in the Cu matrix composite is 12% at which the hardness of the composite is almost twice that of the pure Cu. Daoush et al. (2009) have showed Vickers hardness of the Cu/CNT

composites has increased from 70 VPN for pure Cu to 130 VPN for Cu/20% CNT as shown in Figure 2.3.

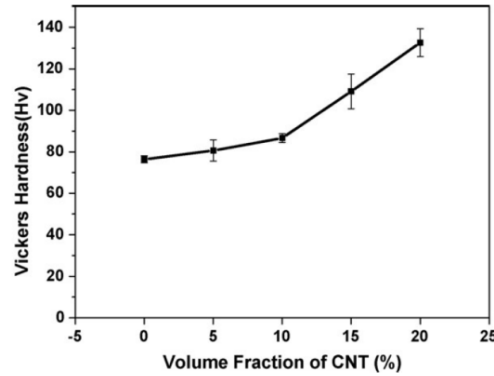


Figure 2.3: Effect of CNT volume fraction on the hardness of Cu/CNT Nano composite
 Yang et al. (2008) also synthesized the CNT reinforced Cu composite by electrochemical-co-deposition and studied the micro-hardness of the composite. A significant enhancement in micro-hardness (1.18 GPa to 1.6 GPa approximately by 36%) was observed in the SWNT/Cu composites. A comparison of hardness properties obtained of the pure copper and Cu/CNT composite are shown in Table 2.2. It is clear that properties are good for Cu/CNT composite due to good interfacial bonding between Cu and CNT reinforcement compared to pure copper.

Table.2.2: The Hardness of CNT/Cu composite by different group of researchers

Author	Year	Mechanical Property	
		With CNT	Without CNT
M. Zhou et al.	2018	With 12 vol.% CNT, Microhardness=155 HV	Microhardness=113 HV
Li, H. et al.	2009	Hardness = 3.5 GPa	Hardness =2.8 GPa
Kim, K. T. et al.	2006	with 10 vol.% CNT, Hardness=1.1 GPa	Hardness =0.8 GPa
Daoush, W. M. et al.	2009	hardness =1.5 GPa	Hardness =0.7 GPa
Yang, Y. L. et al.	2008	with 10 vol.% CNT, hardness =1.61 GPa	Hardness =1.18 GPa.

2.3.3 Corrosion study

Corrosion is known as one of the most significant reasons of degradation in industrial parts and therefore the methods of reducing corrosion and wear costs are being greatly investigated. Under this aspect, the focus is now shifting from synthesis to manufacture of advanced coatings having improved properties. To their exceptional electrical, thermal, and mechanical characteristics, carbon nanotubes (CNTs) also represent an extremely inactive for corrosion behavior. Therefore, addition of CNTs to composites has been indicated to improve corrosion resistance based on the chemically inert nature of CNTs, or by changing the protection mechanism to cation transport as in the case of conducting polymers. This chapter reviews on exploitation of CNTs as an alternative to enhance the efficiency of anticorrosion coatings with emphasis in the development of Cu/CNTs composites.

Chen et al. reported that the weight loss data, resulting from immersion for 240 h in 3.5 wt.% NaCl solution for three samples uncoated, pure nickel coated and CNTs-nickel coated plain carbon steel substrate as shown in Figure 2.4. It is interesting to notice that the presence of CNTs significantly decreased the corrosion rate for CNTs-Ni coated carbon steel. The corrosion resistance for the CNTs–Ni coating was seven times and three times as compared to the plain carbon and pure Ni coated samples, respectively (Chen et al. 2005).

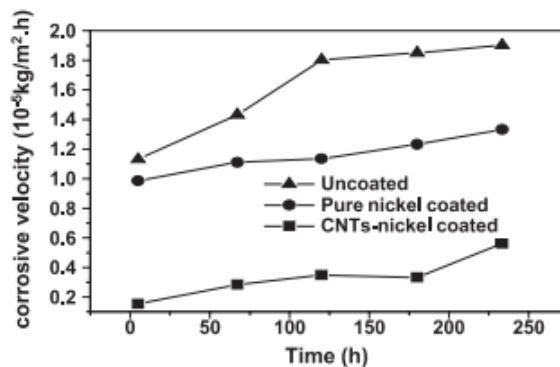


Figure 2.4: Variation of the corrosion rate (mass loss) with immersion time in 3.5wt% NaCl solution

Radhakrishnan et al. carried out salt spray corrosion on the Cu/CNT composite for 48 hrs. From this corrosion rate greatly decreases while increasing the volume % of CNT due to its corrosion resistive property. Corrosion resistance rate improved from 0.87gm/hr to 0.05gm/hr by adding 2vol% of CNT to Cu matrix (Radhakrishnan et al. 2016). In Mg/CNT and Al/CNT composites also the corrosion rate improved (Senthil Saravanan 2011; Endo et al. 2008). This improvement of corrosion rate is mainly because of two reasons.

1. By the addition of CNTs to the metal matrix, the composite exhibit water repellent property because the CNTs are hydrophobic in nature.
2. CNTs can slow down the formation of oxide layer and leads to improvement in corrosion resistance.

The corrosion properties of different metal/CNT composites are compared with pure metal and are shown in Table 2.3.

Table 2.3: Summary of studies on corrosion properties that used CNT

Author	Year	Mechanical Property	
		With CNT	Without CNT
Senthil Saranan et al.	2011	2% CNT in AA4032 alloy $I_{\text{corr}} [\text{mA}/\text{cm}^2] = 0.045$	$I_{\text{corr}} [\text{mA}/\text{cm}^2] = 0.399$
Radhakrishnan et al.	2016	Cu with 2% CNT, Corrosion rate = 0.05.	Corrosion rate (gm) = 0.87
X.Chen et al.	2005	Ni with 2% CNT, Corrosion velocity=0.12	Corrosion velocity=0.12

2.3.4 Thermal conductivity

Tuning of thermal conductivity has become an important parameter especially in state of the art engineering application. Carbon nano tubes (CNTs) is having unique nature of thermal conductivity, it is one of the material which shows extremely high thermal conductivity along the axial direction ($3000\text{W m}^{-1}\text{K}^{-1}$) (Cho et.al. 2010), and extremely

bad thermal conductivity along the transverse direction ($1-2 \text{ W m}^{-1}\text{K}^{-1}$). Therefore several scientists try to prepare metal/CNT composites with different process to enhance the thermal conductivity of composite. Many different processes do not give a high thermal conductive composite because of random alignment of CNTs and cluster formation of CNT or inhomogeneous distribution of CNT in the composite matrix (Chu et al. 2010) as shown Fig.2.5. Other researchers also reported when composite were prepared by powder technology route and other methods no change or almost negligible enhancement in thermal conductivity compared with pure metal (Kim et al. 2009; Gardea and Lagoudas 2014). Therefore, proper selection of process is an important factor to prepare high thermal conductive composites which can be used in heat exchangers or heat sink devices.

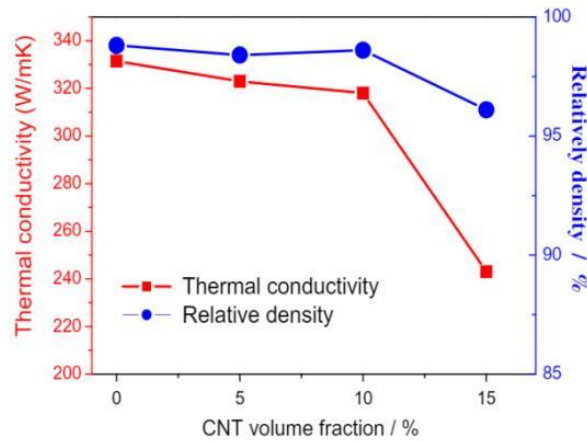


Figure 2.5: Relative density and Thermal conductivity of CNT/Cu composites verses CNT volume fraction

G. Chai and Q. Chen prepared the Cu/CNT composites by electrodeposition technique and measure thermal conductivity by measuring the temperatures at hot end and cold end as shown in set up Fig. 2.6(a). They reported that the thermal conductivity of pure Cu is 339 W/m-K ; As the CNT concentration in the electrolyte increases from 50 mgL^{-1} to 250 mgL^{-1} , the thermal conductivity also increased from 441 W/m-K to 651 W/m-K as shown in Fig. 2.6(b). The reason attributed to (1) Good interfacial bond between Cu and CNT, and (2) The low interfacial thermal resistance from both electrons (Cu) and phonons

(CNT) allowing high thermal conduction in Cu/CNT composite. A comparison study of thermal properties of the pure metal and metal/CNT composites are shown in Table 2.4.

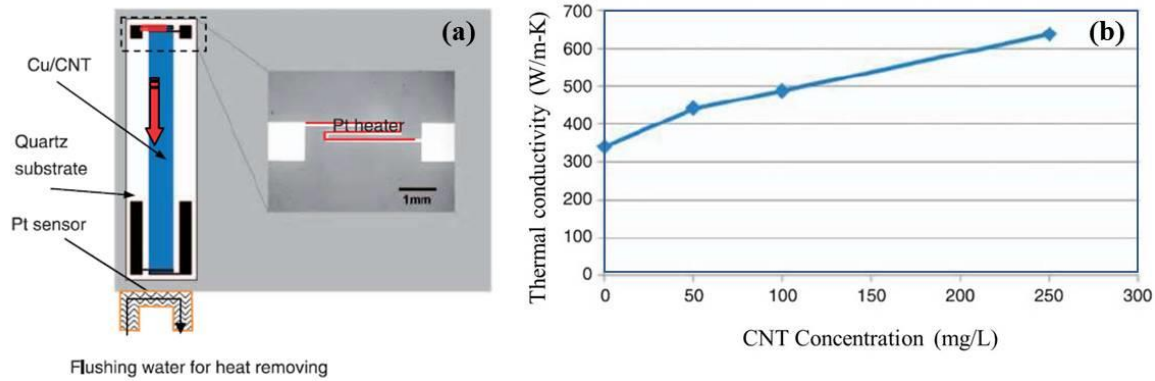


Figure 2.6: (a) Schematic diagram of the thermal conductivity measurement setup and an optical image of the Pt heater (inset) (b) Thermal conductivity (W/m-K) of CNT-Cu composites Vs. concentration of CNT (mgL^{-1}) in electrolyte

Table 2.4: Summary of studies on Thermal conductivity that used CNT

Author	Year	Thermal conductivity ($\text{Wm}^{-1}\text{K}^{-1}$)	
		With CNT	Without CNT
K.Chu et.al. (Powder tech. route)	2010	Cu+5 vol% CNT=325 Cu+10 vol% CNT=320 Cu+15 vol% CNT=242	Pure Cu =331
C. Kim et al. (Powder tech. route)	2009	Cu+Ni coated SWCNT=147	Pure Cu =402 Cu (83%)+Ni(17%)=150
Frank Gardia et al. (Powder tech. route)	2014	At 0.6% CNT, The pristine XD CNT =5.5% Oxidized XD CNT=4.3% Fluorinated XD CNT=2.5%	The neat epoxy =0.297
Susumu Arai et al. (Electrodeposition)	2006	Ni-0.7Wt.% MWCNT =109	Pure Ni =90 Ni coating =60

2.4 Mechanical properties of Zn/GO composite

2.4.1 Cohesion strength

The cohesive mechanical strength of the coating-substrate system is characterized by the critical load L_{C1} , defined as the minimum load at which the first damage occurs. The adhesion strength of coatings is characterized by L_{C2} , defined as the load at which the coating removed completely. The cohesive strength (L_{C1}) values of coatings were

measured using traction force vs. scratch length graph and also matched in the micrograph with that particular length of scratch. The adhesion strength (L_{C2}) was measured by subtracting the total thickness of the coating from profilometer depth curve and matched particular scratch length with normal load. For Ta_xO_y coating on Titanium alloy substrate samples as shown in Fig.2.7, when the scratch length is 0.65mm, continuous perforation and peeling of the Ta_xO_y coating occurs. The critical load L_{C2} is 5.42N which means that the binding strength of coating is 5.42N. While, ZnO- Ta_xO_y coatings have a binding strength of 41.58N at a scratch length of 4.99mm (Ding et al. 2019). In this study, the ZnO act as a good binding material which enhances the adhesion strength of Ta_xO_y coating to Ti alloy.

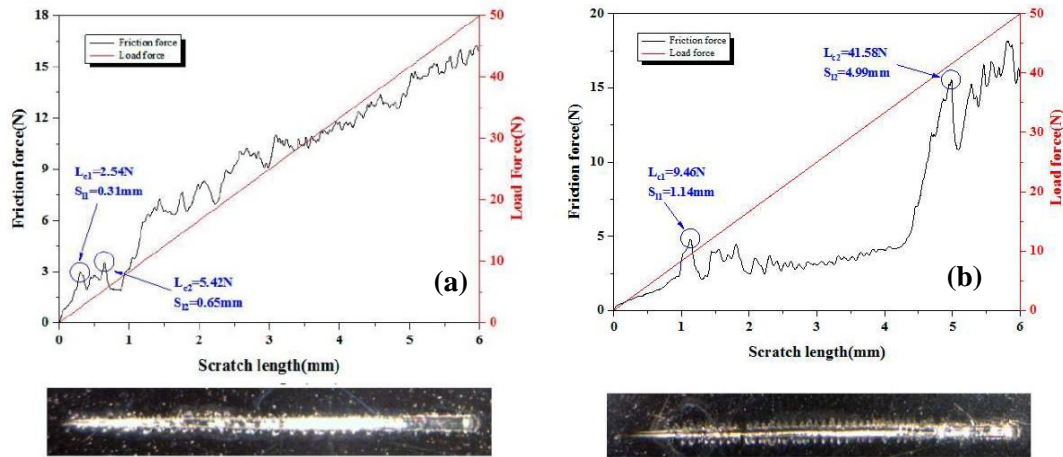


Figure 2.7: Friction force and load force as a function of scratch length for (a) Ta_xO_y (b) ZnO- Ta_xO_y coatings on Ti alloy along with Scratch starting position

The adhesion between the coating and substrate mainly depends on (i) friction (ii) coating – substrate properties (iii) coating thickness. H. Ollendorf and D. Schneider examined adhesion by ion plating deposition using different pre sputtering times on TiN films and recommended maximum time of 15 min for the ion plating process to get the good adhesion (Ollendorf and Schneider 1999). During the scratch test, the stresses demonstrated as a combination of (i) an indentation stress field, (ii) a frictional stress field and (iii) the residual (internal) stresses present in the coating (Sarangi et al. 2020; Ding et al. 2019) .

Zhang et al. (2020) successfully fabricated Ni/Graphene oxide nano composites using ultrasonic assisted electrodeposition technique. The results demonstrated that tribological properties of the composites were improved gradually with an increase in ultrasonic power. Additionally, the increased concentration of GO reduces the coefficient of friction of the composite coatings from 0.45 to 0.3 as shown in Fig. 2.8. When GO concentration increases from 0.1g/L to 0.3g/L, It is seen that the coefficient of friction decreases and the width of the wear track becomes narrower, which indicates the increase of wear resistance of the Ni/GO composite coatings. Mai et al. and Sun et al. also believed that the lubricating and transfer films can be adhered on the contact surface, and therefore lead to a decrease of coefficient of friction (Mai et al. 2018; Sun et al. 2015; Sarangi et al. 2020). The surfactant (CTAB, SDS), coating thickness and temperature contribute significantly to the roughness of the coatings by impact on the tribological behavior of the composite coating (Choi et al. 2022).

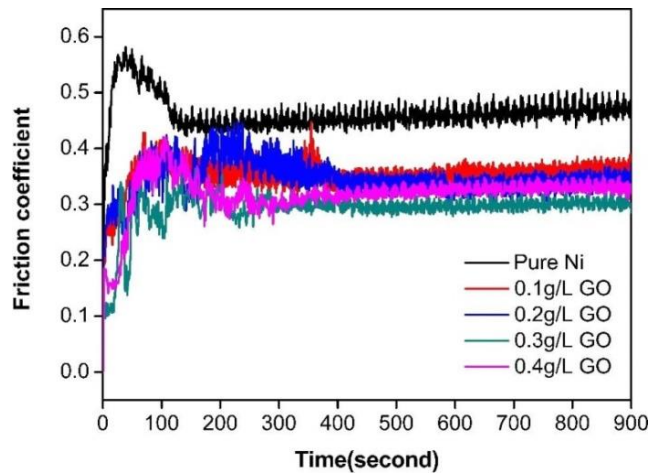


Figure 2.8: The friction coefficient of the nickel/GO composite coatings under the different concentrations of GO (0.1 ~ 0.4 g/L)

A detailed understanding of the tribological and adhesive properties is necessary to predict the behavior of the coatings in real applications. To meet this demand, Frictional behavior and interfacial adhesion of Zn/GO coating on stainless steel substrate were investigated by scratch testing. The critical load L_C determined by scratch tests is widely regarded as representative of the strength of the film and substrate (Randall et al. 2001; Randall et al. 2000). However, not all failures depend on the adhesion of the film to the

substrate but the mechanical properties of the coating and substrate, such as hardness and Young's modulus, surface roughness, friction between the sliding tip and the coated surface, coating thickness, and internal stress in the coating, will also play an important role (Bull et al. 1997; Ollendorf and Schneider 1999).

Laugier (M. T. Laugier 1984) then suggested that spallation of a coating during the scratch test could be represented using an energy balance approach whereby the energy $2E_{\text{surface}}$ required to create the new surfaces formed by spallation of the coating must be less than the release of elastic energy if the coating is assumed to relax totally when detached

$$2E_{\text{surface}} = E_{\text{applied}} + E_{\text{internal}}. \quad (1)$$

Where E_{applied} and E_{internal} are the stored elastic energies associated with the scratch test and the coating internal stress which might be tensile or more usually compressive in nature. Several scientists (Burnett et al. 1987; Je et al. 1986; Lin et al. 1996) reported that stored internal energy mechanism play an important role to detach the coating under the indenter.

2.4.2 Impact strength

Graphene has attracted great interest from both scientific and engineering fields in strengthening materials. The ballistic impact simulation was carried out using Molecular Dynamics (MD) simulation on Cu/monolayer graphene/Cu film by Yong-Chao et al. (2021) as shown in Fig. 2.9. The monolayer graphene film was created on copper (001) plane and the lattice mismatching was kept around 0.09%. The armchair and zigzag direction of graphene is beside the x and y- axes of Cu (001) plane.

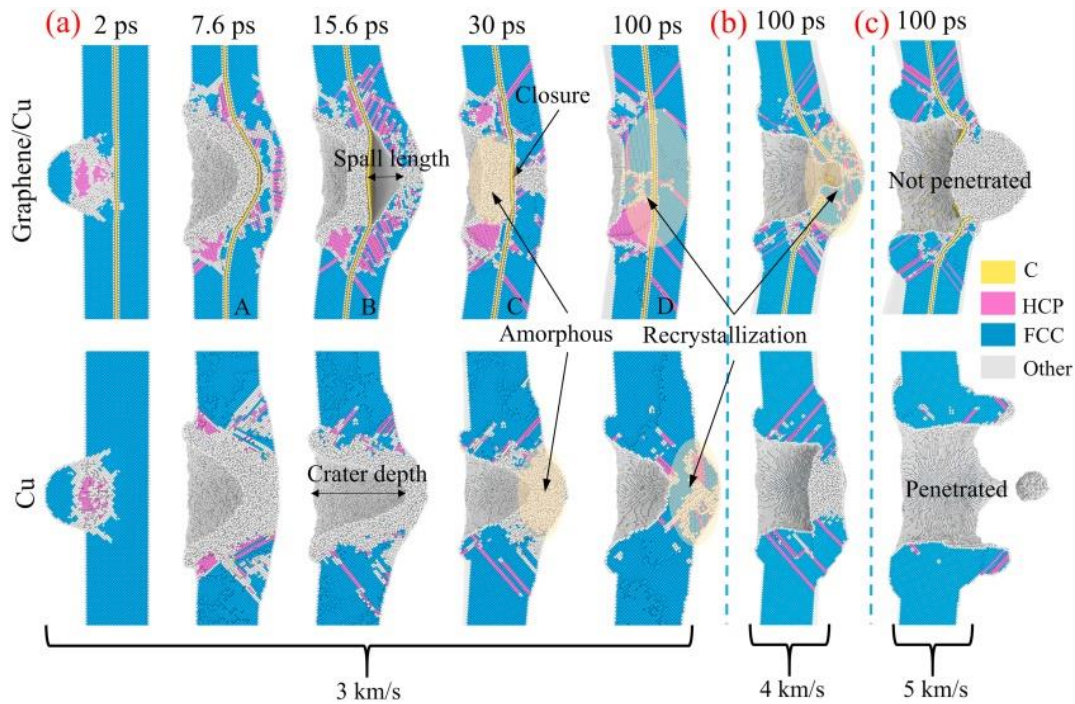


Figure 2.9: (a) Penetration process of the composite and the pure Cu sample at different times at 3 km/s. (b) Final penetration morphology at 100 ps of 4 km/s and (c) 5 km/s. Atoms are colored by structure types. The spall length is defined by the distance of graphene and lower Cu matrix surface. A, B, C, and D corresponds to the beginning, maximum, recover and final states of the spall length, respectively

Cu/graphene/Cu sandwich structure and Cu film were tested with ballistic impact of bullet at velocities of 3 km/s, 4km/s and 5km/s. Recrystallization process starts in the composite at a velocity 3 km/s, within 100 ps. However, when the incident velocity increases to 4 km/s (see Fig.2.9b), where the graphene layer has been destroyed, the composite sample still shows certain recrystallization which is found to dominate the recovery of structure to original layered structure. When the incident velocity increased to 5 km/s (see Fig.2.9c), the bullet penetrated completely into the pure Cu sample but not in the composite. This demonstrates the excellent performance of graphene in preventing the bullet penetration and promoting the damage self-healing (Wu et al. 2021). Long et al. conducted MD simulations to investigate shock response of Cu/graphene nano layered composites. Under parallel or normal shock loading, several phenomena are observed in

Cu/graphene nano layered composites, including deformation and spall damage of Cu, delamination of the nano-laminates, and wrinkling, fracture and perforation of graphene (Long et al. 2016).

The compressive impact tests can be performed at dynamic compressive loading by varying pressure and temperature for producing loadings at various rates through SHPB (Split Hopkinson pressure bars) tests to study the impact compressive damage evolution in composites. Experiments show how strain rate has a strong effect on the compressive strength. Some theoretical prediction of the compressive strength was also made based on the failure mechanism and test data. Some researchers have performed SHPB tests on carbon-fiber-reinforced particles (CFRP) composites and confirmed that the compression strength of samples is strongly dependent on strain rate. Fig. 2.10 (a) shows that as the volume fraction of CFRP increases, the compressive strength increases, however the Young's modulus of the composite shows no substantial difference under impact loading (Fig. 2.10 (b)) (James Lankford 1991; Yuan et al. 1998).

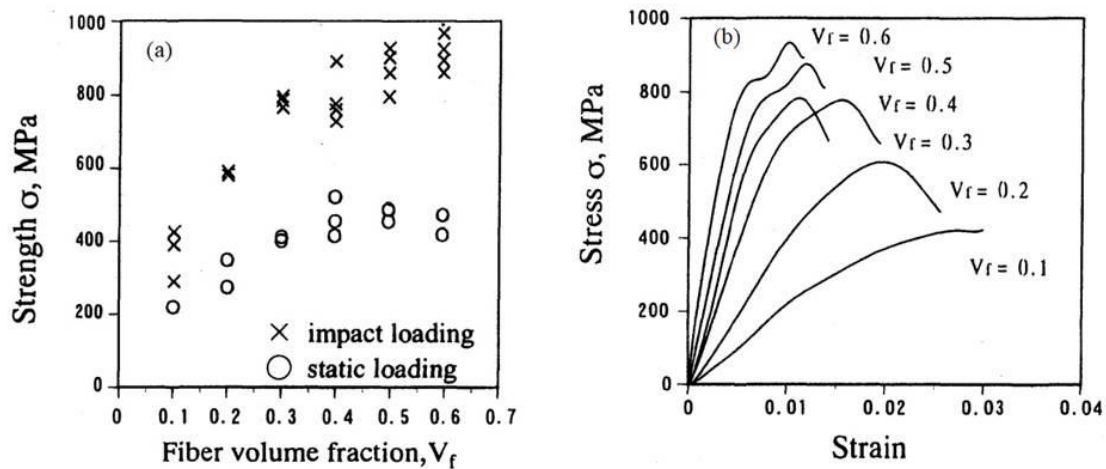


Figure 2.10: (a) Strength Vs. Fiber volume fraction (b) Stress-strain curves of GFRP and matrix under impact loading (strain rate $\sim 10^3 \text{ s}^{-1}$)

As well as the compression strength is also strongly dependent on temperature as per the literature survey. Skiba et al. 2020 prepared AlSi-PE abrasible coatings by thermal spray which can be used in aircraft engines to enhance the overall efficiency by reducing the

clearance between rotating blades and the casing. They measured dynamic compression of coatings on a SHPB at strain rates $>103 \text{ s}^{-1}$ from RT to 360°C . The temperature of coatings were measured by inserting two thermocouples at mid sample thickness and at surface each as shown in Fig. 2.11(a). They have reported that flow stresses decreased rapidly with increasing temperature and at 360°C , the flow stress was $>75\%$ lower than value at room temperature as shown in Fig. 2.11 (b). This trend is observed similarly in the previous literature (Li et al. 2021; Tripathi et al. 2020).

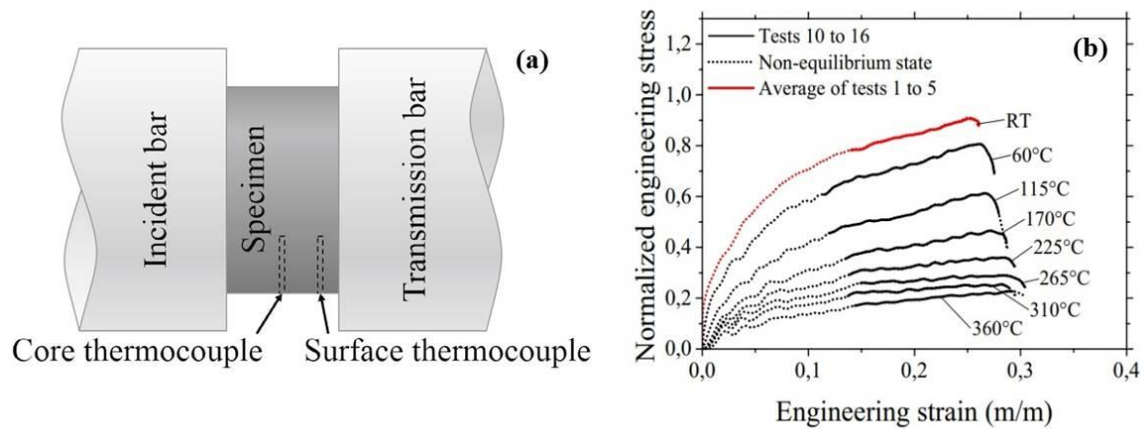


Figure 2.11: (a) Setup of specimen heating from the two thermocouples located in the specimen (b) Compressive Stress-strain curves of an AISi-PE abrasible from room temperature to 360°C for a strain rate of 1200 s^{-1}

2.4.3 Residual stress

The internal stresses during adhesion are the most significance function in materials as it can either boost or degrade performance. Few authors have investigated the origin of the residual stresses in coating and reported that the deposition process and material can play an important role in the residual stress (Oladijo et al. 2012). Stewart et al. worked with WC-17Co coatings which are deposited on steel substrate, and reported a tensile residual stresses of 219 MPa and standard error in the mean of 12 MPa (Stewart et al. 1998). Pina et al. prepared cermets by thermal spray technique with spray materials Inconel, Al_2O_3 , WC-12%Co on ceramic substrate and measured residual stresses using X-Ray Diffraction method. The results show that stresses calculated are compressive due to the relative

magnitude of the thermal expansion coefficients of the coating and substrate materials (Pina et al. 2003). Compressive stress coatings have been shown to provide better wear and scratch resistance, whereas tensile stress coatings perform poorly therefore, compressive stresses are usually the desired residual stresses compared to tensile stresses. Pejryd et al. reported the residual stress for a WC-Co coating which were prepared by plasma spray are of compressive in nature. The coated samples with compressive residual stresses in the substrate had longer substrate fatigue life (Pejryd et al. 1995). Oladijo et al.(2012) prepared composites by thermal spray technique with WC-17%Co on different metal substrates (Brass, Aluminium and Super-invar). They observed compressive stresses on as sprayed coating on brass and aluminium, whereas tensile stress was found on super-invar (alloy of iron and nickel) as shown in Fig. 2.12. The tensile stresses in super-invar might be due to its low thermal coefficient expansion. However, compressive stresses are beneficial, but excessive stresses can cause problems like buckling, which can lead to delamination.

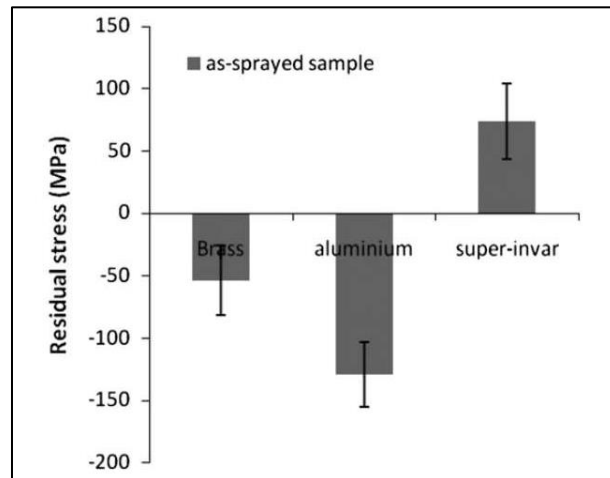


Fig. 2.12: Residual stresses of WC-Co coating on different substrates

2.5 Research Gap

Presently available metal nano composites with CNMs reinforcement were fabricated with complex and expensive methods. Also, getting the homogeneous mixture of CNMs and metal matrix is became a big challenge which is the main parameter to get improved properties in composites compared to pure metal coatings.

In current existing Cu/CNT and Zn/GO nano composites, it is difficult to achieve homogeneous distribution of CNMs in the metal matrix by the other techniques like powder technology, thermal spray, sputtering and even using molecular mixing method. To get the nanocomposites with improved properties, there are many challenges involved such as (1) homogeneous dispersion of CNTs/GO (2) chemical and structural stability of CNTs/GO (3) interfacial bond strength between CNT/GO and metal matrix (4) uniform coating on the Cu/stainless steel substrate.

To get the good interfacial bond strength between CNT/GO and metal matrix, the chemical structural stability of CNTs/GO and selection of fabrication technique are important. The preparation of Cu/CNT and Zn/GO nano composites with improvement in the thermal and mechanical properties is generally preferred nano composites for engineering applications which are currently unavailable in literature. Among the various fabrication techniques studied thus far, the electrodeposition technique appears to be the best method in which the metal ions ($\text{Cu}^{2+}/\text{Zn}^{2+}$) were trapped in between co-deposited CNT/GO uniformly.

Although several studies were conducted on the Cu/CNT composites, no work was carried out on the unidirectional heat transfer rate analysis. Also, the impact strength of Zn/GO coatings which were measured by SHPB experiments, were not explored. In addition, the cohesion strength and residual stress of Zn/GO coatings and their correlation with elevated temperature analysis were not done by any other researchers.

2.6 Objectives

The main objectives of the present investigation are to fabricate and characterize metal/carbon nano structure composites (Cu/CNT and Zn/GO) using electrodeposition technique to enhance the material properties such as tensile strength, hardness, thermal conductivity, corrosion resistance, strain rate, cohesion strength. The specific objectives based on the research gap of the work were decided as follows:

- Detailed study of tensile strength, hardness, corrosion of Cu/CNT composites at various concentration of CNT and comparison study with pure Cu coating.
- Heat transfer rate of Cu/CNT composites with different diameter (SWCNT (6 nm), MWCNT1 (16 nm), and MWCNT2 (170 nm)) and different concentrations.
- Effect of temperature on the cohesion strength of Zn/GO nanocomposites deposited on SS304 stainless steel.
- Effect of temperature and pressure on strain rate of Zn/GO nano composites using SHPB experiments.

CHAPTER 3

METHODOLOGY

In this study, the nano composites were prepared by reinforcing CNMs into metal substrate by electrodeposition technique. The quality of nano composites were prepared by this technique characterized by several techniques such as TEM, FESEM, XRD and Raman. The enhanced physical property such as heat transfer rate, tensile, hardness, corrosion, and impact strength were measured.

3.1 Materials

For preparation of electrolyte, analytical grade chemicals were used for Cu/CNT and Zn/GO coatings. Copper (II) sulphate pentahydrate ($\text{CuSO}_4 \cdot 5\text{H}_2\text{O}$) with 99% purity and Sulfuric acid, N-Cetyl-N,N,N-Trymethyl Ammonium Bromide GR (CETRIMIDE) $\text{C}_{19}\text{H}_{42}\text{BrN}$ (CTAB), MWCNT1 (OD: 6nm-13nm) and MWCNT2 (OD: 110nm-170nm) Sigma-Aldrich (Code: 698849 and 659258) have >95% purity. The SWCNT (OD: 1.4nm-2.2nm) received from PLATONIC of purity >85%. The GO (water dispersed) received from Graphenea have >95% purity (Code: GOSD19039). The electrolyte bath was prepared for Cu/CNT composites by Copper sulfate (CuSO_4), Sulfuric acid (H_2SO_4), and for Zn/GO composites by Zinc sulfate ($\text{ZnSO}_4 \cdot 7\text{H}_2\text{O}$), Sodium sulfate (Na_2SO_4) and Sodium chloride (NaCl).

3.2 Electrodeposition Technique

For dispersion of CNTs in 10 ml of De-ionized (DI) water, CNTs and CTAB well dispersed in 1:5 of weight ratio and homogenized using probe sonicator. The uniform dispersion of CNTs obtained with CTAB and good suspension is the key factor for homogeneous CNT distribution (Hui Li et al. 2017). The electrolyte bath was prepared by copper sulfate ($\text{CuSO}_4 \cdot 5\text{H}_2\text{O}$, 0.70M) and sulfuric acid (H_2SO_4 , 0.86M) dissolved in DI water until to reach pH of ~1. A magnetic stirrer was used for 15-20 minutes to get the uniform solution and further added dispersed CNT into Cu electrolyte and again sonicated for a few minutes. The DC power supply (KEYSIGHT Model No.N6761A)

was used to prepare composites using the electrodeposition technique. The MWCNT along with the Cu ions were electrodeposited on the Cu pipe/Cu fin/plate (cathode) in a copper electrolyte between two anodes for 60 min to get the coating uniformly throughout the surface of the Cu pipe as shown in Fig.3.1. A protective Cu coating of 5-10 μm was prepared on Cu/CNT coating surface to protect erosion of CNT from the surface, and the final coating of $\sim 75\mu\text{m}$ thickness was obtained.

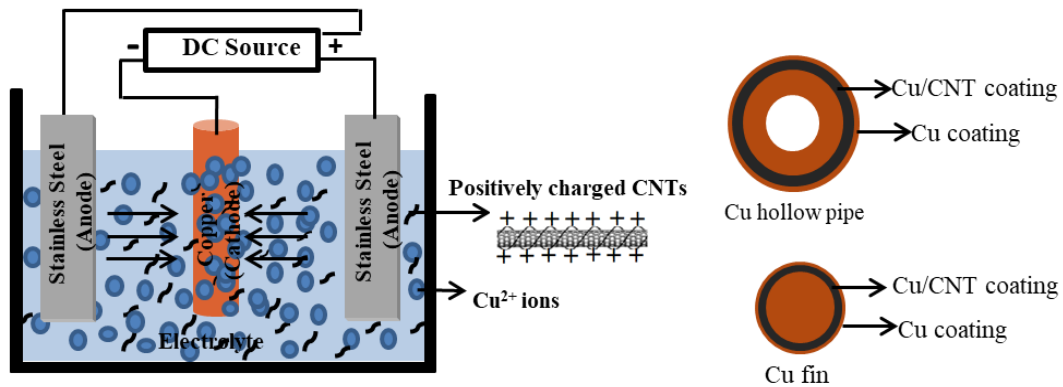


Figure 3.1: The schematic diagram of electrodeposition technique setup and the cross sectional view of Cu fins and Cu pipe samples

Table 3.1: Deposition parameters of Cu/CNT composites

Sample	Bath Composition	Concentration	Deposition Parameters
Tensile, Hardness and Corrosion study			Current density: 20-25 mAcm^{-2} , Deposition time: 30 min for tensile, hardness and corrosion experiments, 60 minutes for thermal experiments, pH : 1, Stirring speed: 200 rpm, Temperature : RT
Cu	CuSO_4	200 g/L	
	H_2SO_4	85 g/L	
Cu/MWCNT2	Cu + concentration of MWCNT2+CTAB	150 mgL^{-1} , 300 mgL^{-1} and 450 mgL^{-1} concentration of CNT, CNT: CTAB is 1:5	
Heat transfer rate study			
Cu/CNT (Cu fins)	Cu + concentration of SWCNT / MWCNT1 / MWCNT2+CTAB	300 mgL^{-1} concentration of CNT, CNT: CTAB is 1:5.	
Cu/MWCNT2 (Cu pipe)	Cu + concentration of MWCNT2+CTAB	150 mgL^{-1} , 300 mgL^{-1} , 450 mgL^{-1} , 600 mgL^{-1} , and 750 mgL^{-1} concentration of CNT, CNT: CTAB is 1:5	

Fig. 3.1 shows the cross sectional view of the Cu fins/pipe samples for heat transfer rate experiment. However for tensile, hardness and corrosion rectangular Cu plate of thickness 1mm was prepared. Table 3.1 listed all the required deposition parameters and conditions to prepare the Cu/CNT composites. Stainless steel plate was used as the anode and the current density was adjusted in the range of 20-30 mA/cm² through hull cell method.

The pure Zn coating and Zn/GO composite coatings were prepared using electrodeposition technique by varying the concentration of GO and coating time on SS304 stainless steel samples. The DC power supply (KEYSIGHT Model No.N6761A, U.S) was used to prepare composites. The GO along with the Zn⁺² ions were co-electrodeposited on the SS304 stainless steel (cathode) in an electrolyte bath. Fig. 3.2 shows the schematic diagram of electrodeposition to prepare Zn/GO nanocomposites along with the cross sectional view of the plate and cylindrical samples. Table 3.2 listed the deposition parameters to prepare the Zn/GO nano composites. Pure Zn plate (>99.9%) was used as the anode and the current density was adjusted in the range of 10-15 mA/cm² which is optimized through the hull cell method.

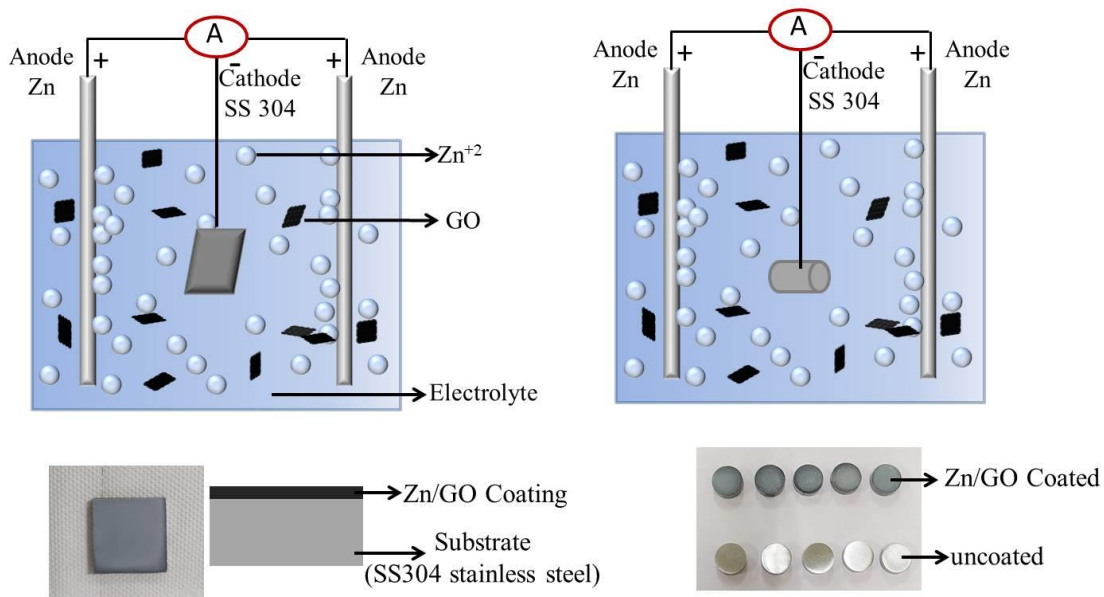


Figure 3.2: Schematic diagram of setup of electrodeposition technique along with the cross sectional view of samples

Table 3.2: Composition and Deposition parameters of Zn/GO composites

Sample	Bath Composition	Concentration	Operating Parameters
Zn	ZnSO ₄ .7H ₂ O	180 g/L	Current density: 10-15 mAcm ⁻² , Deposition time: 10min, 20min & 30min. pH : 5, Stirring speed: 200 rpm, Temp. : RT, 100°C, 200°C, 300°C, 350°C
	Na ₂ SO ₄	30 g/L	
	NaCl	1 g/L	
Zn/GO	Zn + concentration of GO+CTAB	4 mgL ⁻¹ , 8 mgL ⁻¹ , 20 mgL ⁻¹ and 40 mgL ⁻¹ concentration of GO, GO: CTAB is 1:1 & 1:2.	

3.3 Characterization of Cu/CNT Composites

3.3.1 Microstructural Study

The surface topography and the morphology of CNTs and Cu/CNT composites were studied by transmission electron microscope (TEM: JEOL-2100, Japan), scanning electron microscope (SEM: JEOL model JSM 6380 system) and field emission scanning electron microscope (FESEM: 7610FPLUS, JEOL, Japan).

3.3.2 X-Ray Diffraction

XRD is used to investigate the pure Cu coating, Cu/MWCNT2 composites for CNT concentrations of 150 mgL⁻¹, 300 mgL⁻¹ and 450 mgL⁻¹. XRD (JEOL X-ray diffractometer, DX-GE-2 P, Japan) was performed with Cu-K α radiation of 0.154 nm wavelength and scanning rate at 2° per min. The basic law involved in the diffraction method of structural analysis is the Bragg's law as following equation (2)

$$2d\sin\theta = n\lambda, \quad (2)$$

where, 'n' is the order of diffraction.

' λ ' is the wavelength of the X-rays.

'd' is the spacing between consecutive parallel planes

' θ ' is the angle of incidence.

3.3.3 Tensile test

In order to test the tensile strength of the Cu/CNT composites, Dog-bone shape samples were prepared according to ASTM standard E8-EM using the water jet machine. Figure 3.3(a) shows the dimensions of tensile test samples in millimeter and Figure 3.3 (b) shows the prepared tensile test samples. The Cu/CNT composites strength, Young's modulus, and ductility can be determined from the results of a tensile test. The data collected during a tensile test includes load or force as a function of length change (Δl). These data are then subsequently converted into stress and strain. The stress-strain curve is analyzed further to the extract properties of materials, such as yield strength, Tensile strength etc.

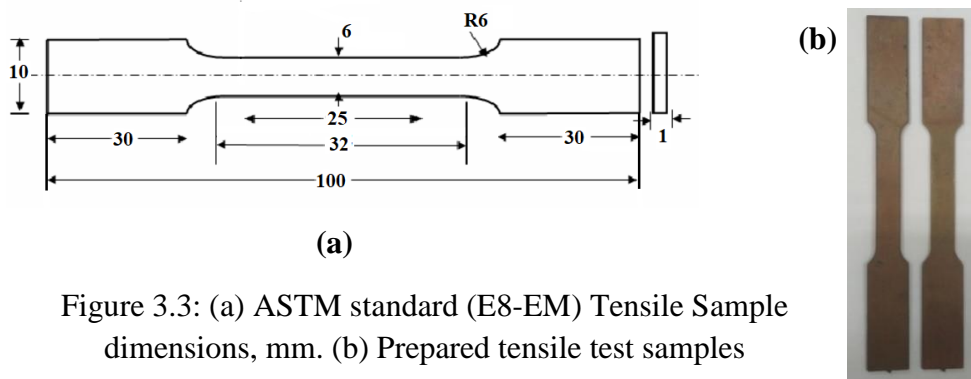


Figure 3.3: (a) ASTM standard (E8-EM) Tensile Sample dimensions, mm. (b) Prepared tensile test samples

3.3.4 Micro Hardness

The hardness of materials is usually determined by indentation. It consists in quantifying the resistance of a surface to the penetration of an indenter. Several methods have been developed to measure hardness and the main ones are Rockwell, Brinell, Vickers and Knoop hardness test. Each method differs from the others by a specific geometry and size of the indenter, has by its specific equation, and presents also specific load conditions. In the present study the hardness of Cu/CNT composites has been calculated by Vickers hardness method using following equation (3)

$$H=1.854F/d^2, \quad (3)$$

where, d = Average diagonal length in mm, F = force used in gf.

3.3.5 Corrosion study

Electrochemical corrosion behavior of pure Cu coating and Cu/CNT coating studied using biologic series SP-150 potentiostat with three-electrode system. The saturated calomel electrode (SCE) is used as a reference electrode, a platinum electrode as a counter electrode, Cu/CNT composite coating (exposed area of 1.0 cm^2) as a working electrode with the electrolyte 3.5 wt% NaCl.

3.3.6 Thermal experiments

The heat transfer rate experiments were conducted on copper fins coated with SWCNT, MWCNT1, and MWCNT2 at 300 mgL^{-1} concentration in natural (without fan) and forced (with fan) convection. The heat transfer rates were compared with copper fins with copper coating of the same thickness, as shown in Figure 3.4 (a). The Cu/CNT composite with the best thermal conductivity was chosen and measured at different concentrations of CNTs (150 mgL^{-1} , 300 mgL^{-1} , 450 mgL^{-1} , 600 mgL^{-1} and 750 mgL^{-1} , respectively) in natural and forced convection. To measure the heat transfer rate, we made two identical acrylic boxes ($7\text{cm} \times 7\text{cm} \times 5\text{cm}$) and cover with an equal amount of insulator to prevent heat loss. Hot water baths of around 80°C were poured into both acrylic boxes, which were then immediately coated with CNTs and only Cu pipes were inserted. After that, the insulator-covered lid was properly placed on the boxes to prevent heat loss. The heat transfer rate measurement system was designed so that heat can pass from inside to outside through the specimen in an axial direction, then heat transferred in a transverse direction after reaching the top side, as shown by the arrows in the schematic diagram in Figure 3.4(b). Heat transfer rate data was collected using the KEITHLY 2700 MULTIMETER instrument (accuracy of 0.001°C). The heat transfer measurement system is depicted in Figure 3.4(b) with schematic diagrams in both the transverse and axial directions. The heat transfer rates of the specimens were measured to a precision of 0.1°C using a k-type thermocouple sensor probe. Small fans were also arranged to observe the heat transfer rate in forced convection.

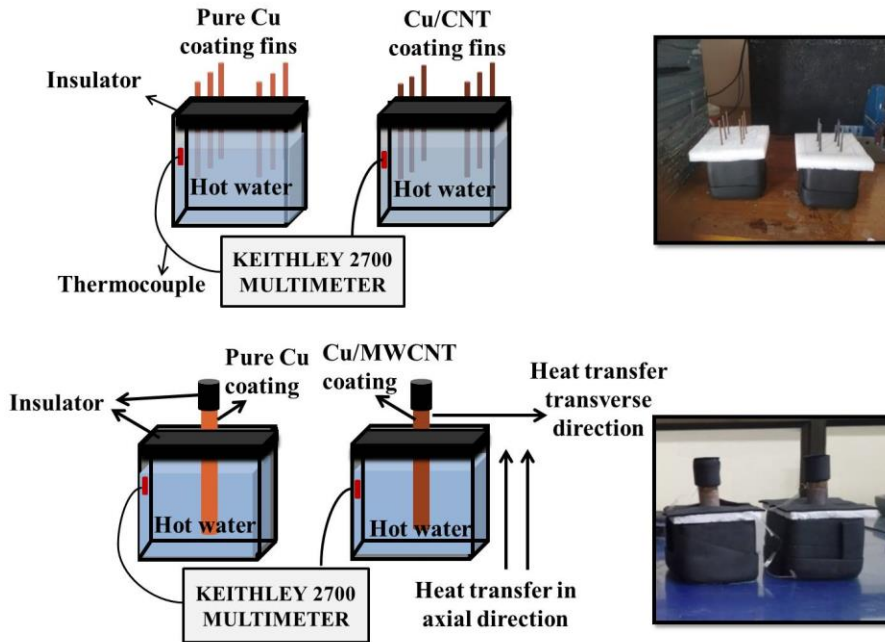


Figure 3.4: Schematic diagrams of setup of the Heat transfer using (a) Cu fins (b) Cu pipe in axial & transverse direction along with original images

The amount of heat transferred per unit of time in a material is called the rate of heat flow, and it is usually measured in watts (joules per second). The flow of thermal energy caused by thermal non-equilibrium is known as heat. The equation of heat flow is given by Fourier's Law of heat conduction is expressed by

Rate of heat flow = - (heat transfer coefficient) × (area of the body) × (variation of the temperature) / (length of the material).

The formula can be written for the rate of heat flow as:

$$\frac{Q}{\Delta t} = -kA \frac{\Delta T}{\Delta x} . \quad (4)$$

Where, Q = net heat transfer (joules J), Δt = time taken, ΔT = difference in temperature between the cold and hot sides, Δx = thickness of the material conducting heat (distance between hot and cold sides), k = thermal conductivity, and A = surface area of the surface emitting heat.

The total heat transferred per unit time is calculated using the basic overall heat transfer equation which is given by

$$q = UA\Delta T \quad (5)$$

$$q = \frac{Q}{t}, \quad (6)$$

where, U = overall heat transfer coefficient ($\text{Jm}^{-2}\text{s}^{-1}\text{C}^{-1}$), ΔT = mean temperature difference, q = heat transfer rate and t = duration of heat transfer.

The peltier generated heat was transferred through the specimen, and equation (5) and (6) were used to calculate the rate of heat transfer (q) through the specimen.

3.4 Characterization of Zn/GO Composites

The pure Zn and Zn/GO coated on a stainless steel substrate of $1\text{cm}\times 1\text{cm}$ dimension were characterized using FESEM along with EDS (GEMINI 300, Carl Zeiss, and Germany). XRD (Empyrean 3rd Gen, Malvern PANalytical, Netherlands) studies have been done to know the phases present in the coatings with $\text{Co-K}\alpha$ radiation of 0.1789 nm wavelength and at $2^\circ/\text{min}$ scanning rate. The quality of the obtained GO and carbon structure of Zn/GO coatings were characterized by Raman spectroscopy using Confocal Raman Microscope (Compact Raman Spectrometer, Renishaw, UK) at 532 nm wavelength. The Zn/GO coated samples were prepared at various coating timings of 10 min. , 20 min. and 30 min. and measured the coating thickness by Digimatic Micrometer (Mitutoyo Corporation).

3.4.1 Scratch tests

Adhesion measurements were performed using the Universal Scratch Testing equipment by applying an incremental load from 2N to 30N on the coating surface. Scratch test was carried out by utilizing the sophisticated model scratch tester (TR- 101, DUCOM, Netherlands) with a $200\text{-}\mu\text{m}$ diamond tip. Progressive load mode of the scratch test was performed on the surface of the coating with a loading range from 2N to 30N with the scratch velocity $0.1\text{mm}/\text{sec}$. The scratch tests have been done on Zn/GO coatings as a

function of GO concentration, coating time, temperature and also observed at the different surfactant ratio with the GO. Temperature dependent (RT, 100°C, 200°C, 300°C & 350°C) scratch test experiments were performed on Zn/GO coated samples which measure temperature dependent adhesion capacity. During the scratch measurement, the coefficient of friction, frictional force, penetration and scratch length values were recorded to determine the scratch-resistant behavior of the coatings. Interfacial adhesion was characterized using the critical normal load at the point when both an abrupt change in normal displacement and also match with crack initiation in the coating observed in the microscope. Moreover, microscope which is attached to the equipment was used to observe and collect the images of the scratched surfaces.

3.4.2 Impact tests

All the samples for SHPB experiment were obtained from the SS304 steel rod by precision cutter accurately after that polished cross sectional surfaces with emery paper. Impact measurements were performed using the SHPB by varying the pressure and temperature on SS304 stainless steel cylindrical samples by utilizing the SHPB impact testing machine (Artis Technologies and Services, Bangalore). The dynamic compressive load was applied on uncoated and coated samples by the SHPB apparatus by holding the sample between the incident bar and transmission bar. The striker bar comes from the pressure chamber and hits the incident bar with a certain velocity which mainly depends on the pressure as shown in Figure 3.5.

The SHPB experiments were conducted at a various pressure (2 bar, 2.5 bar, 3 bar, 3.5 bar and 4 bar) and temperatures (RT, 100°C, 200°C, and 300°C) on uncoated and Zn/GO coated of stainless steel samples. Three experiments were performed at each condition of pressure and temperature, and an average value of three samples was considered as the final result.

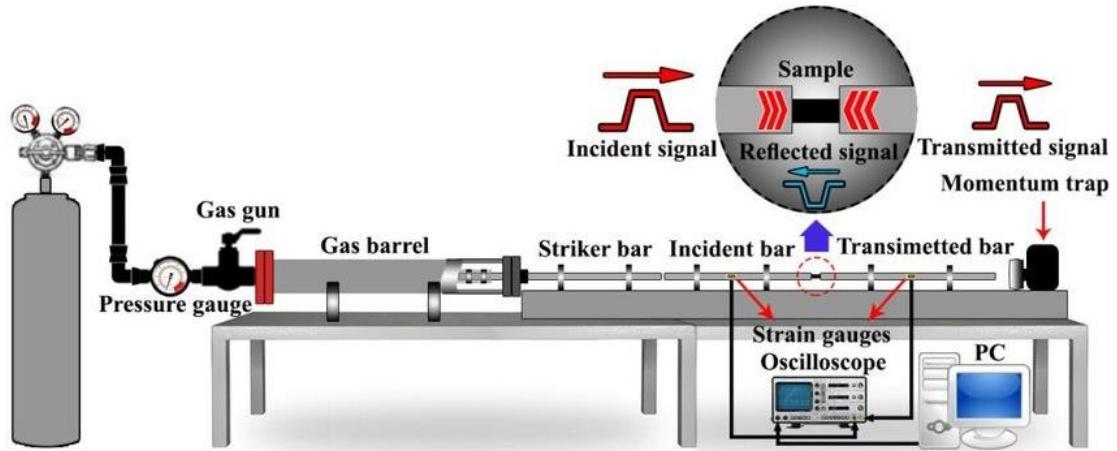


Figure 3.5: Schematic arrangement of SHPB experiment setup

The incident strain (ϵ_T), reflected strain (ϵ_r), strain rate ($\dot{\epsilon}$), and stress (σ) in the specimen are calculated using the following equations based on the waves propagation which were detected by strain gauges (Acharya et al. 2019; Tasdemirci et al. 2010).

$$\epsilon_{engg} = -\frac{2C_0}{L} \int_0^t \epsilon_r dt \quad (7)$$

$$\sigma_{engg} = E_0 \frac{A_0}{A_s} \epsilon_T \quad (8)$$

$$\dot{\epsilon} = -\frac{2C_0}{L} \epsilon_r \quad (9)$$

$$\epsilon_I(t) + \epsilon_r(t) = \epsilon_T(t), \quad (10)$$

where C_0 is the Elastic wave velocity in the bar, A_s and L are the cross-sectional area ($113.14 \times 10^{-6} \text{ m}^2$) and height of the specimen ($5 \times 10^{-3} \text{ m}$), E_0 and A_0 are the Young's modulus and cross-sectional area of the bar respectively. $\epsilon_t(t)$ = Time dependent transmitted strain, $\epsilon_r(t)$ = Time dependent reflected strain, $\epsilon_I(t)$ = Time dependent incident strain.

The elastic wave velocity (C_0) can be calculated by using following formula

$$E = (C_0)^2 \times \rho_{\text{material}} \quad (11)$$

Where, E is the Young's modulus ($205 \times 10^9 \text{ Pa}$), and ρ_{material} is density (8000 kgm^{-3}) of pure SS304 stainless steel

The true strain (ϵ_{true}) and true stress (ϵ_{stress}) are calculated by following equations

$$\varepsilon_{true} = -\ln \varepsilon_{engg} \quad (12)$$

$$\sigma_{true} = \sigma_{engg} (1 - \varepsilon_{engg}) \quad (13)$$

The microstructures of the samples before and after various dynamic pressure and elevated temperature tests were examined by the FESEM. The uncoated samples were polished (emery paper and an automatic polishing machine) and then etched (electrochemical etchant with 10% oxalic acid) for micrographic observation. The Zn/GO coated samples directly after the impact tests were observed under the microscope.

3.4.3 Residual stresses

The diffraction collection was done using the XRD equipment (Empyrean 3rd Gen, Malvern PANalytical, Netherlands). Residual stress measurements were performed in psi-geometry, which means that the sample was tilted around an axis parallel to the plane of the diffractometer on the Zn/GO coatings by using XRD with Co-K α radiation. The Pearson VII method in stress plus software was used to analyze the residual stresses in coatings. Due to the high Zn phase in composite coatings, the residual stress measurements were focused on only the Zn Bragg peak. The lattice plane (201) ($2\theta = 105^\circ$) was selected to observe the variation of diffraction angle for the selected plane at different tilt angles Ψ . The displacement of 2θ peak was reflected the change of (201) lattice plane spacing d . The relations of the 2θ and $\sin^2\Psi$ in different Zn/GO composite coatings were deduced at $2\theta = 105^\circ$ (namely, the increasing value of the $\sin^2\Psi$ was 0, 0.1, 0.2, 0.3, 0.4, 0.5). Once the d -spacing and $\sin^2\Psi$ values were obtained from the XRD at different angle, its slope was solved by the least-two-multiplicative method, The elastic constants $S_1 = -2.778 \times 10^{-6}$ MPa, $1/2S_2 = 1.204 \times 10^{-5}$ MPa and Poisson's ratio = 0.30 were used to convert strain into stress measurements (Randall et al. 2000; Mathabatha et al. 2016) and then the residual stress was solved by the following equation (14)

$$\sigma_\phi = \frac{m}{d_o} \frac{E}{1+\nu} \quad (14)$$

Where, m = slope of d -spacing vs. $\sin^2\Psi$, E = Youngs modulus, ν = poissions ratio, d_o = initial d - spacing.

CHAPTER 4

RESULTS AND DISCUSSION

4.1 Cu/CNT nano composites

4.1.1 TEM and FESEM micrographs

TEM micrographs of MWCNT1 and MWCNT2 and FESEM micrographs of SWCNT were observed after probe sonication with 1:5 ratio of surfactant and confirmed that no agglomeration in the CNTs and also presence of minimal metallic impurities which is shown in Figure 4.1. Using ImageJ software the diameters of SWCNT, MWCNT1 and MWCNT2 were measured at different places of along the length of CNT. The average diameter of SWCNT, MWCNT1 and MWCNT2 were measured as 6.06nm, 163.3nm, and 17.85nm respectively.

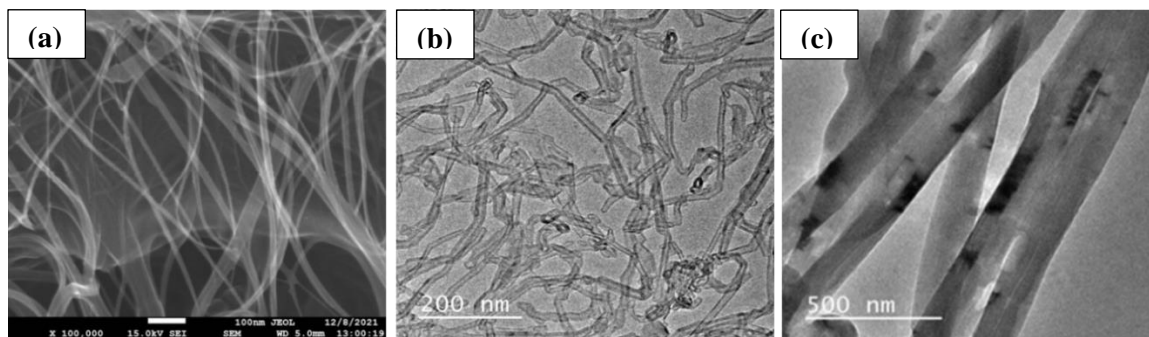


Figure 4.1: (a) FESEM image of SWCNT, TEM micrographs of (b) MWCNT1 and (c) MWCNT2

4.1.2 SEM Micrographs

Scanning electron microscopy (SEM) images of Cu/CNT composite are shown in Figure 4.2. In this, the MWCNTs are deposited by electro deposition technique along with the copper on copper plate with 1cm×1cm dimensions. The SEM image shows the morphology of Cu/MWCNT2 composites for 150 mgL⁻¹, 300 mgL⁻¹, 450 mgL⁻¹, 600 mgL⁻¹, 750 mgL⁻¹ concentrations. The increasing the concentration of MWCNT2 from

150 mgL⁻¹ and 750 mgL⁻¹ more MWCNT2 were deposited at the constant area. A group of MWCNTs can form a randomly oriented depending on concentration of MWCNT.

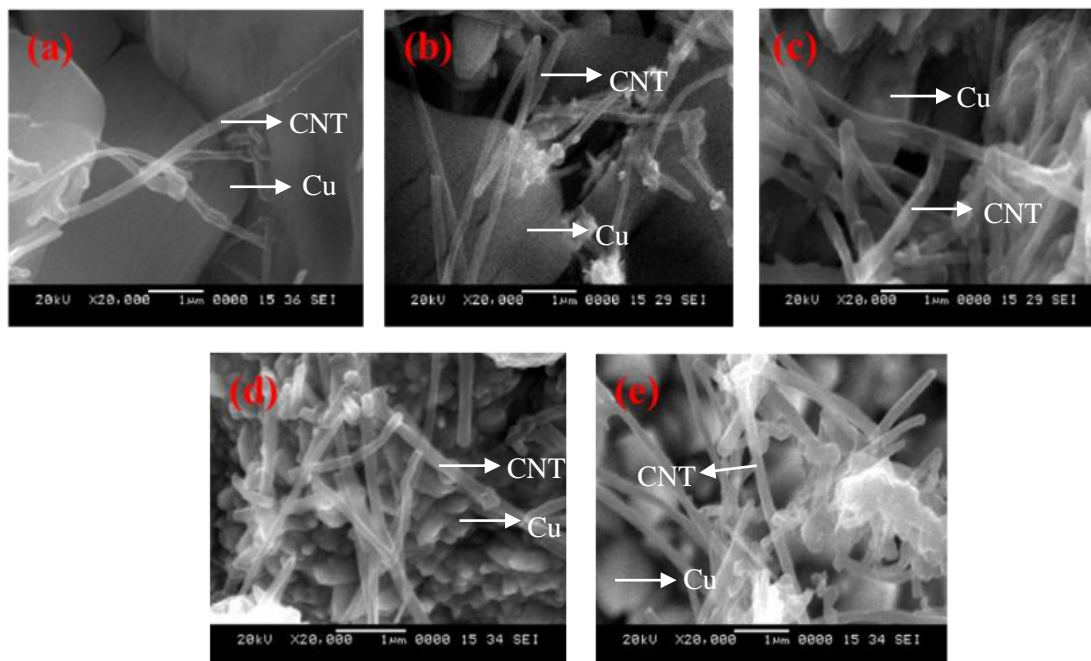


Figure 4.2: SEM images of Cu/MWCNT2 (a) 150 mgL⁻¹, (b) 300 mgL⁻¹, (c) 450 mgL⁻¹, (d) 600 mgL⁻¹, and (e) 750 mgL⁻¹

The Cu/CNT composites were prepared at 300 mgL⁻¹ concentration, same deposition parameters and same area of 1cm×1cm. The FESEM images of pure Cu, Cu/SWCNT, Cu/MWCNT1 and Cu/MWCNT2 were shown in Figure 4.3 (a-d). The spherical copper deposits incorporating MWCNTs were observed as per literature (Arai et al. 2007). The homogeneous deposition obtained throughout the sample and most of the CNTs in the matrix were observed along the lateral direction.

The EDS analysis has been carried out in order to validate the presence and to reveal the distribution of CNTs in samples. The EDS of Cu/SWCNT, Cu/MWCNT1 and Cu/MWCNT2 coatings have been studied by using FESEM equipped with EDS analyzer. SEM-EDS scan region of Cu/SWCNT, Cu/MWCNT1 and Cu/MWCNT2 coatings surface was smooth and distributed evenly with CNTs. The area of coatings 2mm×2mm selected at 5 various places of sample and performed EDS. The average mass fractions

(wt.%) and atomic fractions (at.%) of chemical elements on the coating surface were shown individually in Table 4.1. At the same deposition parameters, the Weight% of C have been observed for Cu/SWCNT, Cu/MWCNT1 and Cu/MWCNT2 coatings as 8.4%, 7.58% and 7.06% respectively. The Cu/SWCNT has highest percentage/number of SWCNT in comparison with MWCNT1 and MWCNT2.

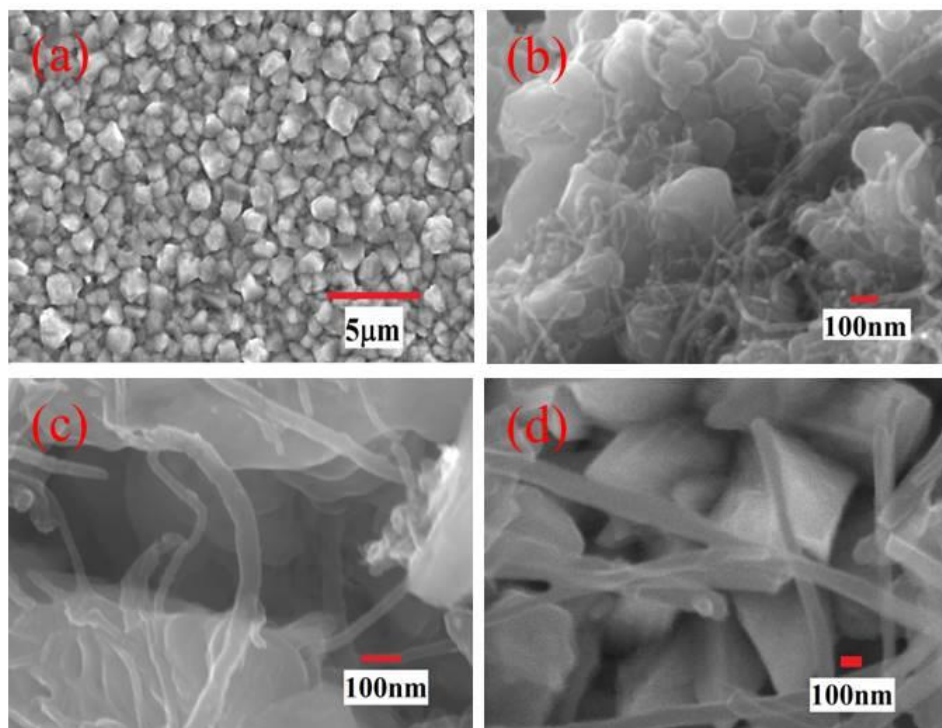


Figure 4.3: The FESEM micrographs of (a) Pure Cu, (b) Cu/SWCNT, (c) Cu/MWCNT1 and (d) Cu/MWCNT2 at 300 mgL^{-1} concentration at same deposition parameters

The reason attributed to lighter in weight CNTs deposited more in number. Because at the same current density all the CNTs experience equal amount of electromotive force as a result lighter weight of CNTs or smaller diameter CNTs will deposit more on Cu surface as EDS suggest. The rate of incorporation into the metal deposit is influenced by particle size. According to the findings, as the nanoparticle size becomes smaller, more can be incorporated into a metal deposit per unit volume (Low et al. 2006).

Table 4.1: FESEM-EDS data of (a) Cu/SWCNT, (b) Cu/MWCNT1 and (c) Cu/MWCNT2 nanocomposites

Elements	Cu/SWCNT		Cu/MWCNT1		Cu/MWCNT2	
	Wt.%	At.%	Wt.%	At.%	Wt.%	At.%
C	8.4	29.5	7.58	26.72	7.06	27.52
O	4.76	12.14	6.04	14.98	1.76	5.18
Cu	86.26	57.58	85.4	57.14	91.06	67.12
S	0.6	0.78	0.98	1.16	0.14	0.18

Figure 4.4 shows the cross sectional micrographs of Cu/MWCNT1 coating which is observed through FESEM. From the micrograph, coating thickness observed as 75.78μ for 60min coating time. Also CNTs were present between the Cu crystals randomly in different direction. Most of the CNTs observed axial direction to the in plane of the surface and very few were in out of plane in axial direction to the surface as shown in Figure 4.4(b). Most of CNTs deposit axially to the plane and very few deposit perpendicularly to the plane because of the low electromotive force acting on the cross section of the CNTs due low surface area, as illustrated in the schematic view of Figure 4.4(c).

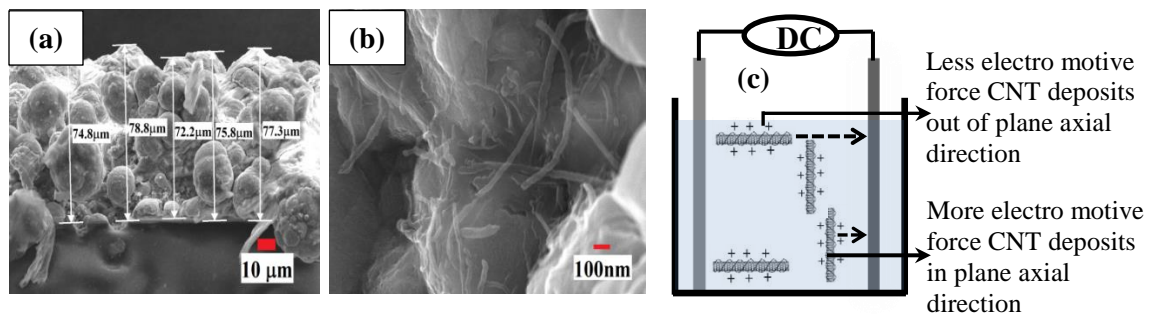


Figure 4.4: FESEM images of cross section view of Cu/MWCNT1 coating (a) coating thickness (b) CNTs alignment in Cu matrix (c) Schematic view of CNT deposition

4.1.3 XRD

The pure Cu coating and Cu/MWCNT composites using MWCNT2 were characterized by XRD. From Figure 4.5, the XRD patterns confirmed the existence of MWCNT in the Cu matrix. For pure Cu coating, the peaks were observed at 2θ about 43.51° , 50.38° , 73.98° and 89.9° ; it matches with the JCPDS file no. 01-071-4610. Further, extra peaks were noticed on the reinforcements of MWCNT at 2θ values of 26.66° corresponding to (002) plane of carbon which matches with the JCPDS file no. 00-041-1487. From the XRD pattern in the Figure 4.5, it is also observed that the Cu (111) plane is slightly shifted towards higher angle due to MWCNT concentration increased in the matrix (Das et al. 2015; Karolina et al. 2018).

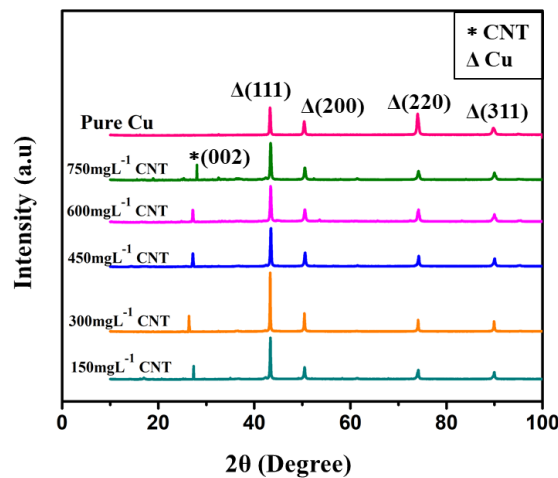


Figure 4.5: Representative XRD profiles of Cu and Cu/MWCNT2 composite

4.1.4 Tensile Test

The MWCNT deposited along with Cu onto dog bone sample using an electrodeposition technique in an electrolyte bath. The testing was performed at a strain rate of 0.2mm/min. Figure 4.6 shows stress-strain curve of tensile tests at room temperature for Cu/CNTs composite. It can be seen that for the composites, the tensile strength increases with an increase in the volume fraction of CNTs. The ultimate strength and Yield strength of pure copper and Cu/MWCNT composites was mentioned in Table 4.2. The tensile strength of pure Cu is about 270 MPa. The observed strain is 22%, 27%, 28% and 30% for pure Cu,

and Cu/MWCNT composites at 150 mgL⁻¹, 300 mgL⁻¹ and 450 mgL⁻¹ concentrations of CNT respectively. As the amount of CNTs in electrolyte increases, the resultant tensile strength is increased 8%, 13% and 25% for 150 mgL⁻¹, 300 mgL⁻¹ and 450 mgL⁻¹, respectively. The reason for the increase in strength is due to the CNT has much higher tensile strength compared to Cu, also due to better interfacial bonding between Cu-CNT and deposited Cu atom on Cu substrate. Even after tensile test measurement, there is no peeling of the deposited material (Cu/CNT coating) from the Cu substrate which confirms that a better Cu deposited on Cu substrate, which means the loading was evenly distributed between the substrate and composite.

Table 4.2: Tensile Strength values of pure Cu and different concentrations of Cu/MWCNT nano composites

Sample	Yield Strength (MPa)	Tensile Strength (MPa)	Strain
Pure Cu	222	276	22%
Cu/MWCNT (150 mgL ⁻¹)	247	294	27%
Cu/MWCNT (300 mgL ⁻¹)	262	312	28%
Cu/MWCNT (450 mgL ⁻¹)	286	344	30%

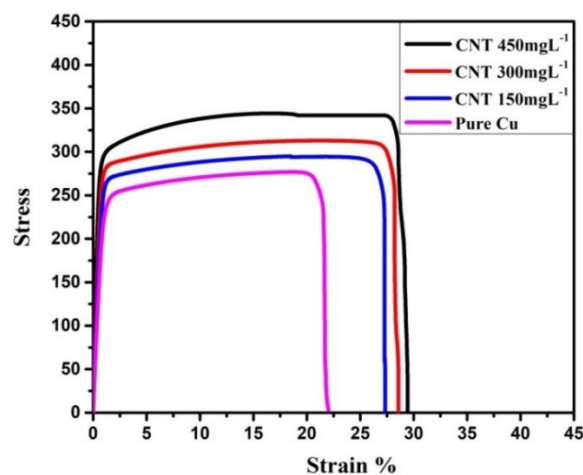


Figure 4.6: Stress strain curve of pure Cu and different concentrations of Cu/MWCNT composites at 150 mgL⁻¹, 300 mgL⁻¹ and 450 mgL⁻¹

4.1.5 Micro Hardness Test

Micro hardness (HV) of Cu/CNT composites was measured using a (Micro Hardness Tester (FM-800)) micro HV indenter with a load of 500 gf for a dwelling time of 10s. Ten indentations on different parts of each sample were measured and their averaged hardness values were calculated. The hardness obtained for pure Cu is 118.68 HV, whereas for Cu/MWCNT composites are 24%, 36% and 47% higher than pure copper for 150 mgL^{-1} , 300 mgL^{-1} and 450 mgL^{-1} , respectively which are given in Figure 4.7 and Table 4.3. This indicates that the CNT coating yielded a relatively harder surface than Cu substrate because of MWCNT has hardness value around 25GPa. However in case of powder technology route, it is noted that by fabricating Cu/MWCNT the composite yield only 32% of hardness due to presence of micro voids and agglomerates in the composite (Darabi et al. 2020). Whereas in our study, it is observed that by altering the coating fabrication process and parameter it yields a dense CNT coating with a high degree of uniformity and distribution in Cu matrix which results in a relatively much harder coating.

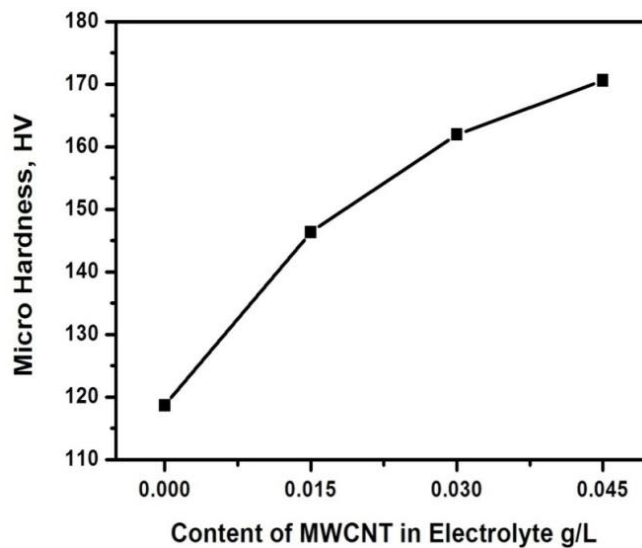


Figure 4.7: The Microhardness values variation with content of MWCNT in electrolyte

Table 4.3: Hardness values of pure Cu and different concentrations of Cu/MWCNT composites

S. No.	Hardness (HV)	Increment
Pure Cu coating	118	NA
Cu/MWCNT (150 mgL ⁻¹)	146	24 %
Cu/MWCNT (300 mgL ⁻¹)	162	36 %
Cu/MWCNT (450 mgL ⁻¹)	174	47 %

4.1.6 Corrosion study

4.1.6.1 AC-impedance measurements

The corrosion resistance of pure Cu and Cu/MWCNTs composite coating was calculated by AC-impedance measurements. Electrochemical impedance parameters were fitted using Z-fit analysis in EC lab software and experimental data were fitted with electrical circuits called “equivalent circuits”. This circuit represents various components that relate to electrochemical, chemical or physical reactions with the metal and environments. Nyquist plots were obtained in the 3.5 wt. % NaCl solution for pure copper and Cu/MWCNT are shown in Fig. 4.8(a). Similarly, Bode Plots in the form of modulus of impedance and phase angle with respect to frequency are shown in Fig. 4.8(b). The impedance parameters were obtained by best fitting all the experimental data using an equivalent circuit which is shown in Fig.4.6 and the impedance kinetics such as solution resistance (R_s), film resistance (R_1), charge transfer resistance (R_2), constant phase elements (Q1 and Q2), values of the exponent ‘n’ recorded as shown in Table 4.4.

Nyquist plots shown in Fig. 4.8(a), clearly indicates a significant variation of semicircle radius for pure copper and composites by using a various amount of CNT as reinforcements such as 150 mgL⁻¹, 300 mgL⁻¹ and 450 mgL⁻¹. The larger capacitive loop was produced by Cu/MWCNT coating and pure Cu shows smaller capacitive loop. Fig. 4.8b shows the Bode plots which is good representation of electrochemical impedance

behavior as it indicates directly modulus of impedance and phase angle with given frequency ranges. A higher modulus of impedance indicates the stability of passivity and shift of phase angle towards -90° to 90° indicates the uniform formation of passive film. Modulus of impedance decreases as concentration of MWCNT decreases from 450 mgL^{-1} to 150 mgL^{-1} at lower frequency. Total coating resistance or polarization resistance ($R_p=R_1+R_2$) calculated by fitting electric circuit (as shown in Fig.4.9) and are shown in Table 4.4, clearly indicates that the higher amount of reinforcement of CNT (450 mgL^{-1}) in Copper has shown that a significant increment with respect to lower CNT concentration (150 mgL^{-1} and 300 mgL^{-1}) and without CNT. The obtained results are found be better for good passivation and resistance to corrosion by increasing the CNT in the matrix of copper.

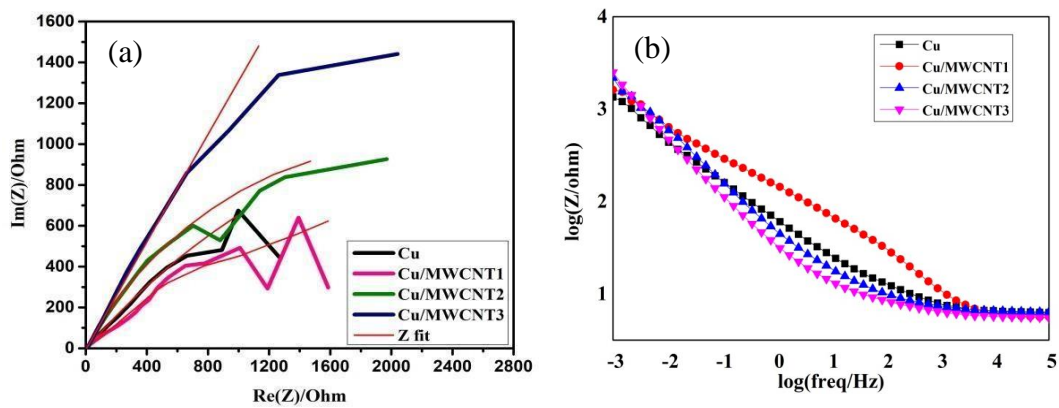


Figure 4.8: (a) Nyquist plots (b) $\log(\text{Freq/Hz})$ vs. $\log Z/\text{ohm}$ Bode plot of a pure copper coating and Cu/CNT samples in 3.5wt% NaCl solution

Table 4.4: Electrochemical AC impedance studies of pure Cu and Cu/MWCNT

Sample	$R_{sol}/\Omega\text{cm}^2$	$R_1/\Omega\text{cm}^2$	$Q_1 \times 10^{-6} \text{ S}^n/\Omega\text{cm}^{-2}$	n_1	$R_2/\Omega\text{cm}^2$	$Q_2 \times 10^{-6} \text{ S}^n/\Omega\text{cm}^{-2}$	n_2	$R_p = R_1 + R_2$
Pure Cu	6.379	27.83	4.43	0.62	3268	3.65	0.66	3333
Cu/MWCNT1	5.324	50.9	5.24	0.54	3827	4.04	0.78	3900
Cu/MWCNT2	5.874	11.48	7.09	0.42	5010	5.36	0.86	5000
Cu/MWCNT3	5.563	8.402	3.38	0.44	8962	8.93	0.89	9000

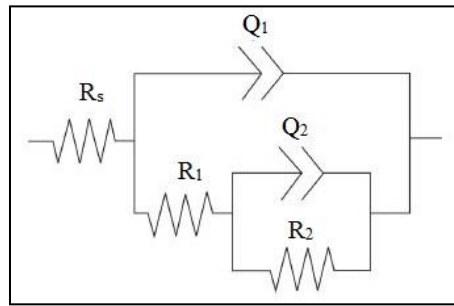


Figure 4.9: Equivalent circuits for curve fitting of Pure Cu and Cu/CNT composites

4.1.6.2 Tafel polarization studies

Electrochemical corrosion plots of Cu/CNTs in the solution of 3.5 wt.% NaCl solution are shown in Fig 4.10. Corrosion kinetics parameters such as corrosion potential (E_{corr}), corrosion current density (i_{corr}) and corrosion rates were calculated using Tafel slope of the curves for pure copper and MWCNT composite coatings are tabulated in Table 4.5. E_{corr} of Cu/CNT composites have shown a positive shift towards noble potentials as compared pure copper coating indicating that a spontaneous passive film formation the surface of composite as compared to pure copper. Corrosion current density (i_{corr}) decreased for Cu/MWCNTs coatings compare to that of pure copper coating (Table 4.4). This is due to the presence of uniformly distributed MWCNTs on the Cu matrix.

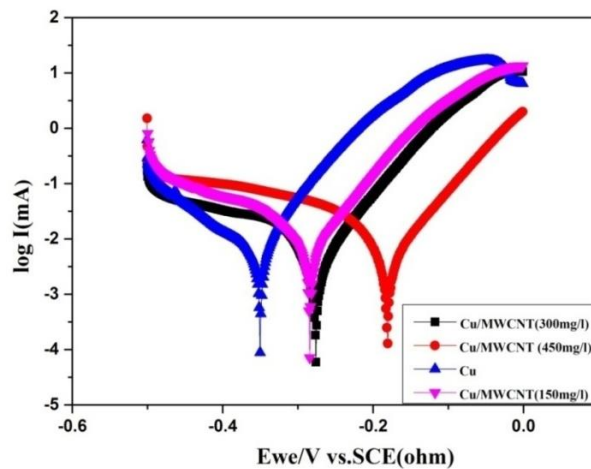


Figure 4.10: Tafel polarisation plots of pure Cu and Cu/MWCNT coatings

It was also observed from these corrosion results that corrosion rate for pure Cu is 0.07 mmpy (mm/year), however, Cu/MWCNT (450 mgL⁻¹) composites has 0.02 mmpy which is significantly lower values suggesting that Cu-MWCNTs nano-composite coating had higher corrosion resistance than the pure Cu coating. A resistance against to the corrosion and high passivity is due to the presence of uniformly distributed MWCNTs on the Cu matrix. It decreases the grain size of copper coating that suppressed the active surface area of Cu/MWCNTs nano-composite coatings. Also, the presence of cracks and ultra-micro holes could be filled by addition of CNT in to the matrix of pure copper (Ramaliangam et al, 2017).

Table 4.5: Corrosion current density and corrosion potential of pure Cu and Cu-MWCNTs composite coating obtained from Tafel Polarization studies in 3.5%NaCl Solution

Material	Amount of MWCNT(mg/L)	E _{corr} (v) vs. SCE	I _{corr} ($\mu\text{A cm}^{-2}$)	Corrosion rate/mmpy
Pure Cu coating	0	-0.340	3.24	0.07
Cu/MWCNT1	150	-0.268	2.30	0.04
Cu/MWCNT2	350	-0.253	2.29	0.03
Cu/MWCNT3	450	-0.190	1.09	0.02

4.1.7 Heat transfer rate experiments

4.1.7.1 Experiments using Cu fins

Heat transfer characteristics of prepared samples are tested for natural (without fan) as well as forced convection (with fan). The experiments are carried out on pure copper fins, and copper fins with coating of SWCNT, MWCNT1 and MWCNT2 at 300 mgL⁻¹ concentration with and without fan. Among all these samples the MWCNT2 shows highest cooling rates of 21.46°C/hr and 28.83°C/hr for natural and forced convection, respectively as shown in Fig.4.11. The heat transfer rates for all the samples are shown in Table 4.6. Due to larger diameter, the number of MWCNT2 deposition is less compared

to smaller diameter CNTs at same operating conditions as observed in EDS results (Table 4.1) as well as SEM images (Fig.4.3 b-d). This can also be observed in SEM images (Fig.4.3b-d). Due to the higher thermal resistance between tangled CNT-CNT in transverse direction, the results showed less heat transfer for Cu/MWCNT1 and Cu/SWCNT as explained with detailed mechanism in Fig.4.11.

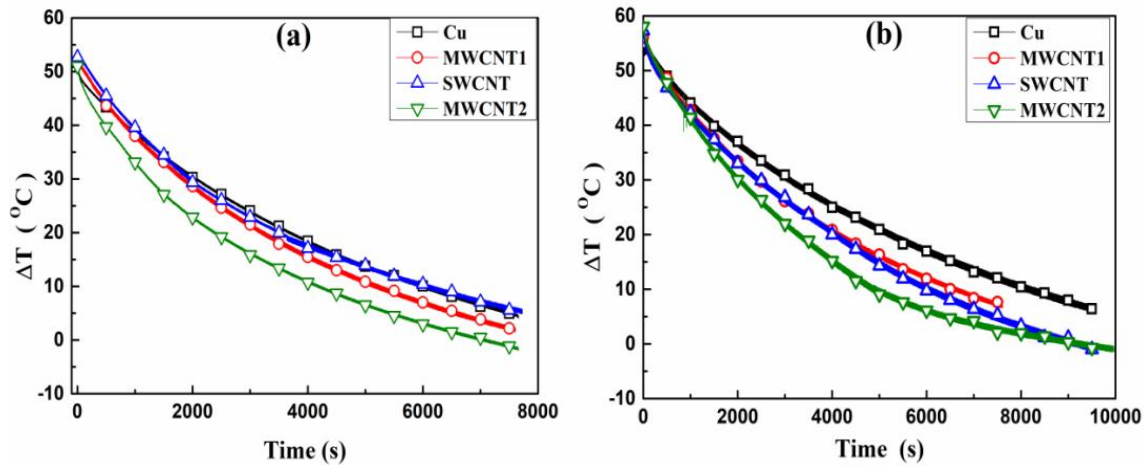


Figure 4.11: The cooling rate curves of Cu, SWCNT, MWCNT1 and MWCNT 2 coated on copper pipe (a) without fan and (b) with fan

Table 4.6: The heat transfer rate values of Cu, SWCNT, MWCNT 1 and MWCNT2 composites

Sample Type	Cooling rate (°C/hr)	Cooling rate (°C/hr)
	Natural convection	Forced convection
Pure Cu	12.6	14.4
SWCNT	15.94	20.37
MWCNT 1	16.23	21.96
MWCNT 2	21.46	28.83

In aligned CNTs, some researchers reported a high CNT-CNT contact thermal interface resistance. They observed that as the CNT density increases, the intercalation structure's heat transfer efficiency decreases due to the extensive CNT-CNT contact (Ji et al. 2016;

Marconnet et al. 2011). Also due to the large diameter and less amount of CNTs deposited on the matrix, MWCNT2 shows a higher heat transfer rate compared to SWCNT and MWCNT1. Hence, MWCNT2 is chosen for further study of varying concentration of CNT from 150 mgL^{-1} to 750 mgL^{-1} to comprehend the heat transfer behavior in axial as well as in transverse direction.

4.1.7.2 Experiments using Cu Pipe

The heat transfer rates are measured for Cu/MWCNT2 composite, prepared at different CNT concentrations as mentioned in Table 3.1. These experiments are carried out with and without fan, and values are compared with pure copper coating. The heat transfer rate graphs of Cu/MWCNT2 composites with pure copper plotted as shown in Fig.4.12 same is presented in the form of ratio $Q_{\text{CNT}}/Q_{\text{Cu}}$ in Fig. 4.13. The $Q_{\text{CNT}}/Q_{\text{Cu}}$ values at 450 mgL^{-1} are observed to be maximum compared to all other concentrations considered in the study for natural as well as forced convection. At low concentration (150 mgL^{-1} and 300 mgL^{-1}), the composites show less conductivity due to lack of conductive network of CNTs (Fig.4.14a). As the CNT concentration increases to from 150 mgL^{-1} to 450 mgL^{-1} the $Q_{\text{CNT}}/Q_{\text{Cu}}$ value increases from 1.12 to 1.41 in natural convection and 1.18 to 1.47 in forced convection, by increasing the concentration of CNT in Cu matrix. However, from 450 mgL^{-1} to 750 mgL^{-1} the $Q_{\text{CNT}}/Q_{\text{Cu}}$ value decreases from 1.41 to 1.08 in natural convection and 1.47 to 1.17 in forced convection. This shows the optimum number of CNT or better CNT network is required for achieving a high heat transfer in above prepared sample. As shown in Fig. 4.14b the optimum number of the CNTs on sample is deposited in axial direction which results in better electrons and phonons contribution in high thermal conduction (Fig.4.14b). As heating wall thickness can influence the heat transfer (Magrini et al. 1975), at same thickness of coating ($76 \mu\text{m}$), the Edward et al. reported that CNT-Cu composite achieved higher heat transfer rate by 1.24 times of pure Cu coating (using cold spray process), where as in present study we have achieved up to 1.41 and 1.47 times of pure Cu for natural and forced convection respectively (Edward et al. 2013). At 600 mgL^{-1} and 750 mgL^{-1} concentration of CNT, the $Q_{\text{CNT}}/Q_{\text{Cu}}$ values are less compared to 450 mgL^{-1} . As the number of CNTs deposited at higher concentration,

are more, the resistance between CNT-CNT gets increased and CNT starts working as an insulator which is depicted in Fig.4.11c (Aliyu and Srivastava 2021).

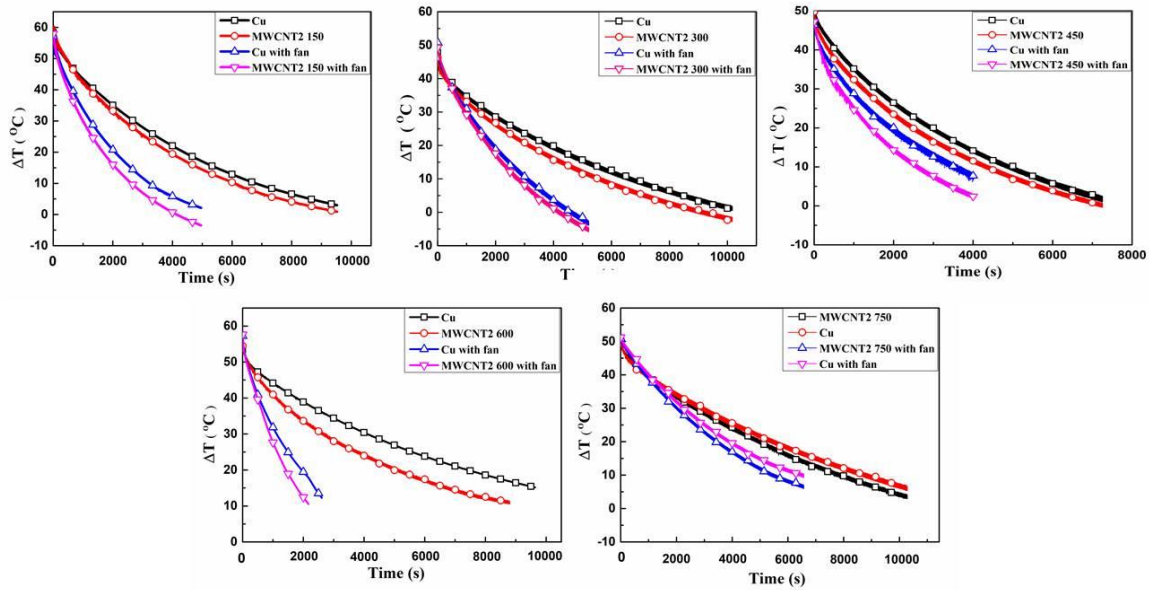


Figure 4.12: The heat transfer rate curves of Cu/MWCNT2 at different concentrations of (a) 150 mgL^{-1} , (b) 300 mgL^{-1} , (c) 450 mgL^{-1} , (d) 600 mgL^{-1} and (e) 750 mgL^{-1} coated on copper pipe without fan and with fan

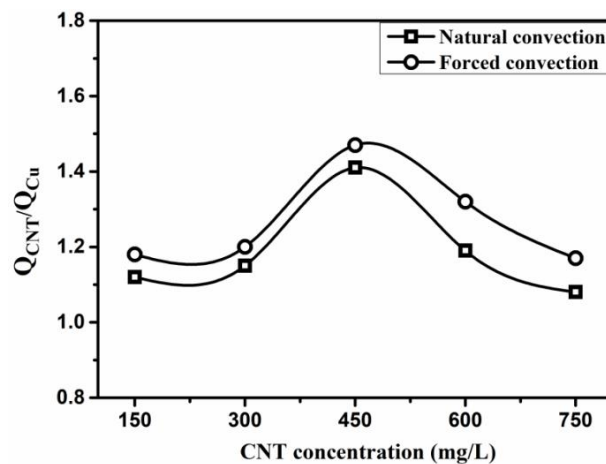


Figure 4.13: The $Q_{\text{CNT}}/Q_{\text{Cu}}$ values of Cu/MWCNT2 coatings at various concentrations of CNT in natural and forced convection

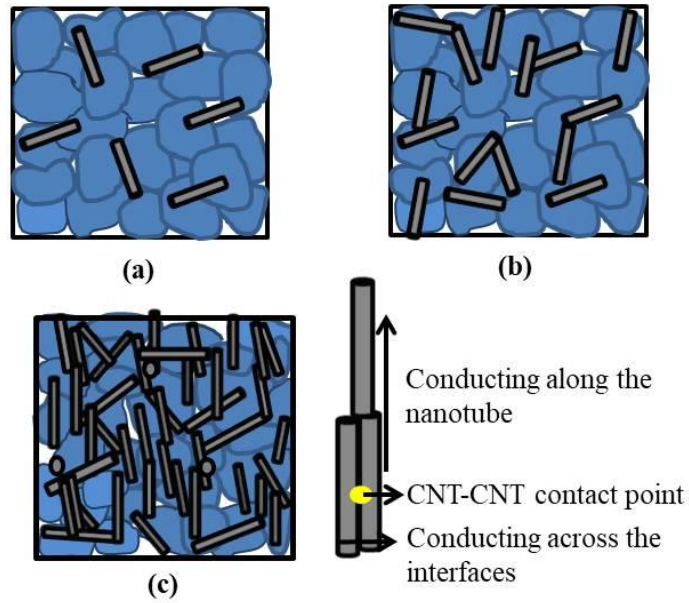


Figure 4.14: Schematic diagram of Cu/MWCNT2 composite at (a) 150 mgL^{-1} , (b) 450 mgL^{-1} concentrations of CNT (c) 750 mgL^{-1} , CNT-CNT contact region and its thermal conduction mechanism

The CNTs act as an insulator across its transverse direction, so the heat transfer would be through the Cu atoms in the transverse direction of the CNTs (Fig.4.11c). The fundamental theory of energy transport states that a material's total thermal conductivity is determined by the energy carrier's electrons and phonons. Electrons dominate the energy transmission through copper, while phonons are dominant in CNTs. As a result, the total thermal conductivity of Cu/MWCNT2 composites enhances due to the effect of both electrons and phonons energy carriers. Because of the uniform dispersion of CNTs and the good interfacial bonding between Cu and CNTs, both electrons (Cu) and phonons (CNT) can contribute to the thermal conduction mechanism of a Cu/MWCNT2 composite (G. Chai and Q. Chen 2010; Mandal and Mondal 2018). The incredible effects of phonon conduction in the fabricated nanocomposites at 450 mgL^{-1} concentration could be attributed to the optimum number of CNTs align in the preferential direction (axial direction) of MWCNT, resulting in higher thermal conductivity (Mandal and Mondal 2018; Darabi et al. 2020).

4.2 Zn/GO nano composites

4.2.1 FESEM Micrographs

FESEM micrographs of pure Zn coating and Zn/GO composites are shown in Fig. 4.15. FESEM micrographs corresponding to Fig. 4.15a display the surface morphology of pure Zn coating as fibrous morphology which is similar to that reported by Rekha and Srivastava (2019). The FESEM micrograph of the Zn/GO nanocomposites (Fig. 4.15b) reveals the uniformly dispersed GO across the Zn matrix and no agglomeration of GO is observed in the matrix (Azar et al. 2020). The homogeneous deposition of the sample has created a uniform, compact, and crack-free morphology. The incorporation of GO into the Zn matrix alters the fibrous morphology of Zn coating (Fig. 4.15a) to a laminate structured morphology (Fig. 4.15b).

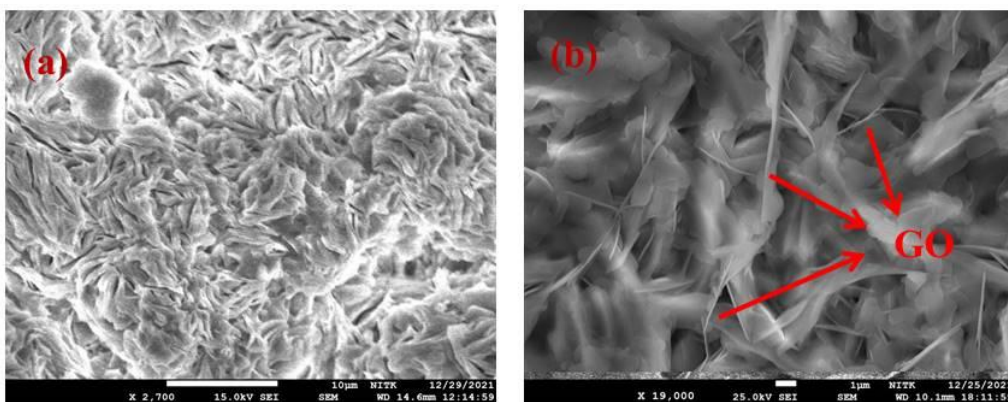


Figure 4.15: FESEM micrographs of (a) Pure Zn and (b) Zn/GO nanocomposites of 4 mgL^{-1} GO with 1:2 of GO:CTAB

The EDS analysis was carried out to determine chemical composition of Zn/GO composites. Fig. 4.16 shows the EDS spectrum of Zn/GO composite at 4 mgL^{-1} GO concentration in the electrolyte. The EDS was performed on $27 \mu\text{m}$ thickness of Zn/GO coating on stainless steel substrate. The mass fractions of chemical elements on the coating (wt. %) are as follows: Zn 70.27, C 2.41, O 13.45, S 3.89, and others 9.99; and an atomic fraction (at. %): Zn 40.69, C 7.60, O 31.81, S 4.59, and others 15.41 as shown in Fig. 4.16 (a). The Zn concentration is the highest, followed by O

and other ones. The area of the coating selected as $16 \mu\text{m}^2$ as shown in Fig. 4.16 (b) micrograph of coating.

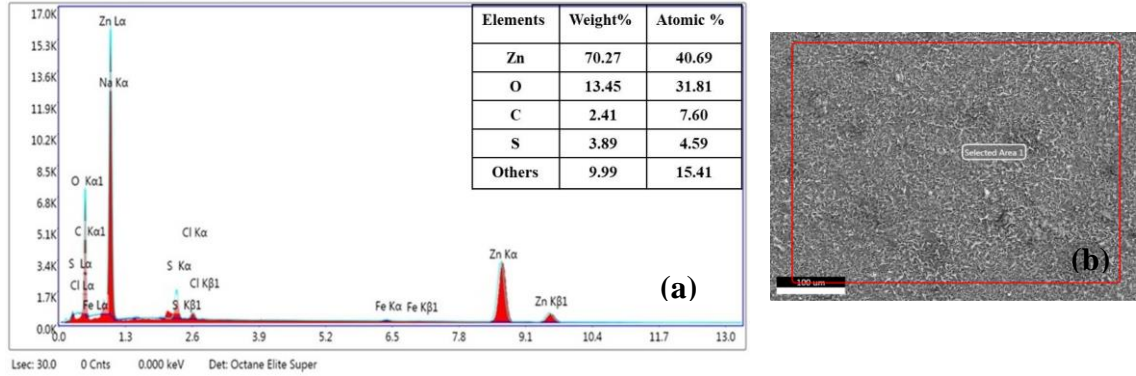


Figure 4.16: (a) EDS Spectra of Zn/GO composite along with elements with (b) micrograph image

4.2.2 XRD

The XRD patterns obtained for pure GO coating and Zn/GO nanocomposites with various GO concentrations are illustrated in Fig. 4.17. The diffraction peak of GO was observed at 10.54° corresponds to (001) as shown in Fig. 4.17(a) which is consistent with literature (Rekha and Srivastava 2019; Zhang et al. 2020).

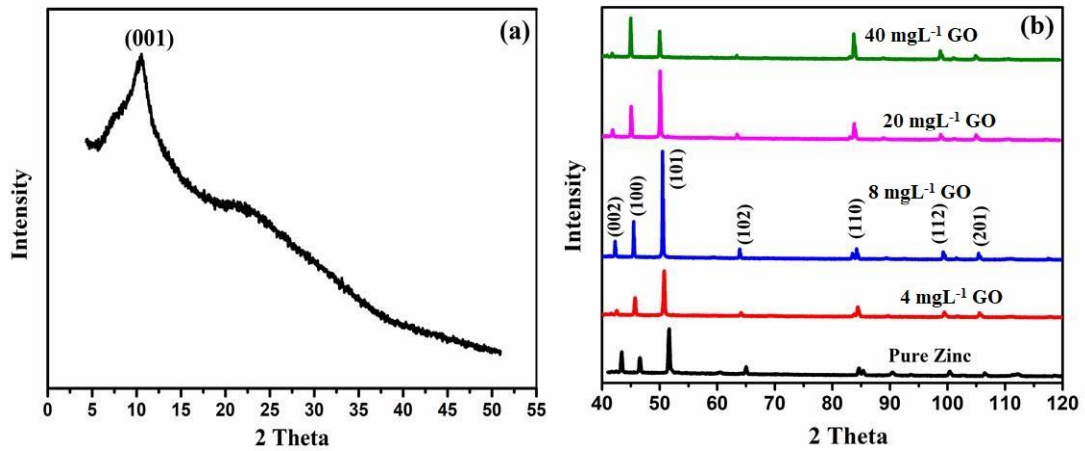


Figure 4.17: X-Ray Diffraction profiles of (a) pure GO (b) pure Zn coating and Zn/GO nanocomposites at various concentrations of GO and 1:2 of GO:CTAB

Fig. 4.17 (b) shows the XRD of Zn/GO composite where, the diffraction peaks indexed to (002), (100), (101), (102), (110), (112) and (201) planes matched well with the phase of Zn (JCPDS File Ref. Code: 00-004-0831). There is a significant displacement of (101) peaks (as shown in Fig. 4.18), indicating that the presence of a reinforcement in the coating promotes a distortion of its lattice parameters. The shifting of diffraction peak towards to lower angles is due to internal stress caused by reinforcement of small sized carbon structure into Zn matrix. However, graphene oxide diffraction peak was not noticed in Zn/GO composite diffraction profile. Absence of GO characteristic peak in the diffraction pattern of nanocomposite is caused by low amount of embedded graphene sheets. Hence, to confirm about the presence of GO in nanocomposite, Raman spectroscopy test was carried out on the Zn/GO nanocomposites.

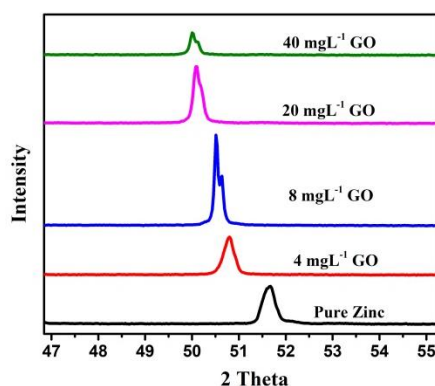


Fig. 4.18: The diffraction peak shift of Zn/GO composite at various concentrations of GO

4.2.3 Raman spectroscopy

Raman spectroscopy provides the information about carbon products based on the inelastic scattering of a molecule irradiated by a monochromatic light source. Fig. 4.19 shows Raman spectra of GO and Zn/GO composites in the range of 100-3000 cm^{-1} . The D band and G band in the spectra (Fig. 4.16) represent the disorder bands and the tangential bands, respectively (Johra et al. 2014). The D vibration band which is formed by j-point phonons of A_{1g} symmetry, and the G vibration band formed from the first-order scattering of E_{2g} phonons by sp^2 carbon atoms. In general, the D-band and G-band for pure GO can be seen at 1350 cm^{-1} and 1580 cm^{-1} respectively, whereas in our study it is observed at 1344.7 cm^{-1} and 1602.6 cm^{-1} . The reason for the shift of D-band and G-

band attributed to (1) phonon confinement caused by the defects (5–7–7–5 and 5–8–5 defect structure) (2) functional groups (3) structural distortions (4) changes in the laser frequency (Kudin et al. 2008). The D-band and G-band of Zn/GO composites were noticed at 1340.2 cm^{-1} and 1588.4 cm^{-1} respectively. The shifts in G-bands and D-bands in the nanocomposite are due to ionization energies of the metals as well as charge transfer energies between metal particles and graphene oxide. Also, suggested that the GO functionalization altered the structural vibrations of the Zn/GO composites (Xu et al. 2011; Tian et al. 2012; Kabiri et al. 2017). Small peaks in Zn/GO composite spectra at 460 cm^{-1} , 638 cm^{-1} , and 1000 cm^{-1} are corresponding to ZnO present in the coating at small quantity due to the oxidation of Zn (Gultekin and Akbulut et al. 2016; Li et al. 2020).

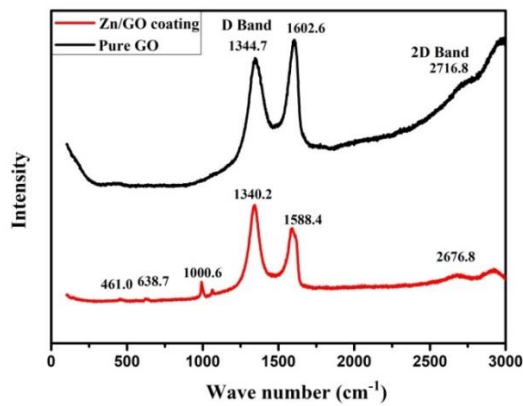


Figure 4.19: Raman spectra of (a) pure GO and (b) Zn/GO composite coatings

A broad 2D band was observed at 2716.8 cm^{-1} for pure GO which is shifted to the lower wavenumber of 2676.8 cm^{-1} for Zn/GO coating. Depending on the presence of oxygen-containing functional groups, the location of the 2D band is shifted (Johra et al. 2014; Hidayah et al. 2017). The broadening of the 2D band is attributed to the number of layers with defects in the graphene oxide. The presence of GO signature in the Raman spectra of Zn/GO nanocomposite is strongly confirmed that composite contains a significant amount of graphene oxide which was not visible in case of XRD analysis. The I_D/I_G for GO and Zn/GO composite is 0.89 and 1.27, respectively. In the case of Zn/GO composite $I_D/I_G > 1$, the reason is attributed to defect structure in GO and the addition of oxygen-

containing functional groups during electrodeposition process (Hidayah et al. 2017; Azar et al. 2020).

4.2.4 Scratch test results

The scratch tests have been performed at different test conditions as mentioned in section 3. The given scratch length was 5 mm, as displayed in Fig. 4.20. Fig. 4.20 (a & b) shows the plot of traction force and normal load with the scratch length for the Zn/GO nanocomposite with ratio of GO: CTAB::1:1 and at 4 mgL^{-1} GO concentration for a coating time of 10 min. The abrupt change in the graph occurred during the early stage of the test. The typical macrograph at 4X magnification of total length of the scratch is presented in Fig.4.20 (c). The cohesive strength (L_{C1}) of Zn/GO nanocomposites was measured using traction force vs. scratch length graph and also matched in the micrograph with that particular length of scratch as shown in Fig. 4.20 (c). The coating failure starts with cracks in coating during scratch track which is shown in Fig.4.20 (d).

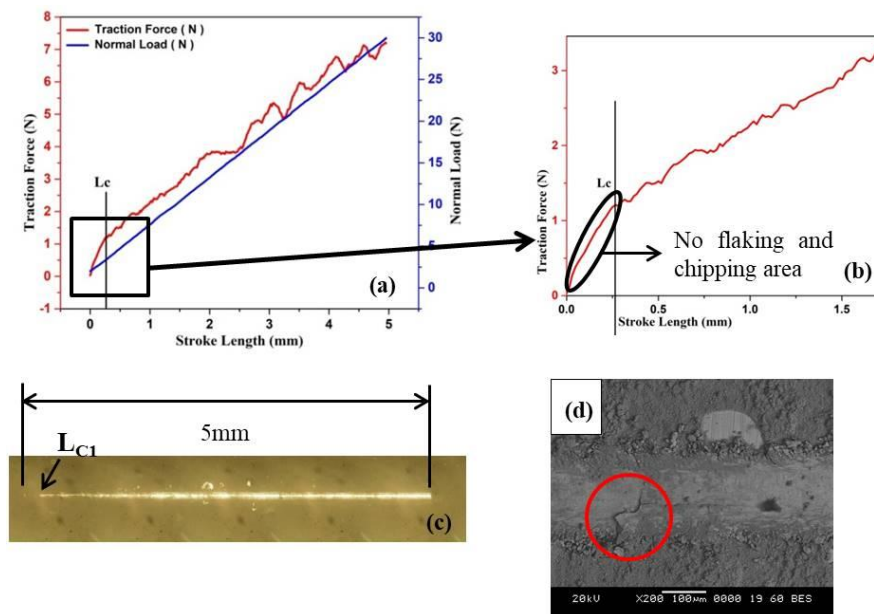


Figure 4.20:(a) Frictional force during progressive scratch on Zn/GO nanocomposite of 4 mgL^{-1} GO with 10 min coating time (b) inset in (a) showing area of no flaking and chipping (c) Macrograph of 5 mm length of scratch (d) Optical image of coating cracks in the scratch track at 200X

The cohesive strength (L_C) values for pure Zn coated on the stainless steel substrate were calculated as 2.216 N, 2.619 N, and 2.662 N for 10 min, 20 min, and 30 min, respectively. The L_C values for all Zn/GO nanocomposites with different GO concentrations, time, and the ratio of surfactant are measured as mentioned in above procedure and listed in Table 4.7.

The relationship between L_C values and coating time of pure Zn coating and various Zn/GO composites are depicted in Fig. 4.21. Compared to the 1:1 ratio, the 1:2 ratio of GO: CTAB Zn/GO nanocomposite shows higher L_C values. The higher quantity of CTAB allows it to counter more effectively the attractive interactions between graphene nanosheets and make them stable in aqueous conditions (Nazari et al. 2019). Out of all the 1:2 ratio of GO:CTAB Zn/GO nanocomposites, 30 min coated composites have the higher L_C values. Valli reported that critical load L_C is strongly dependent and increases with an increase in coating thickness from 2 μm to 15 μm by scratch test (Valli 1986). The experiments were also designed to observe L_C values with respect to temperature and residual stresses for the Zn/GO nanocomposite sample coated for 30 min with a 1:2 ratio of GO:CTAB.

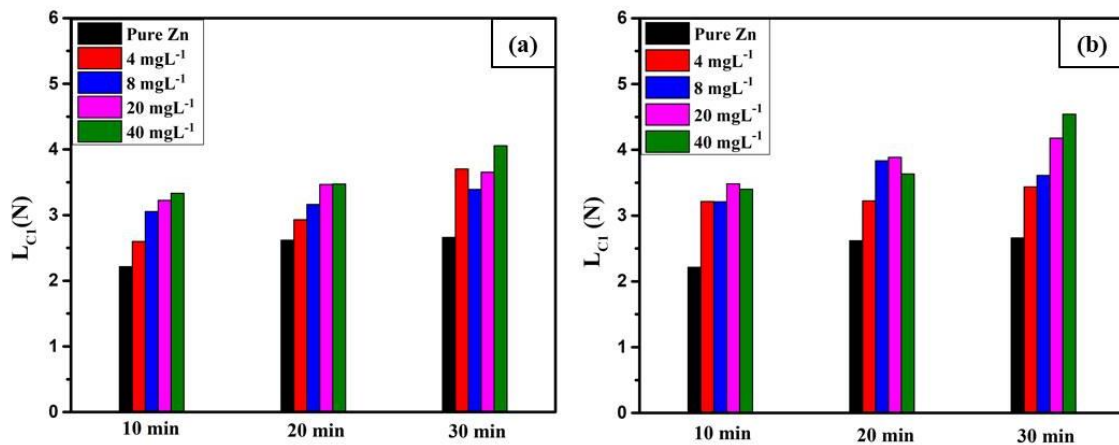


Figure 4.21: L_C values of Pure Zn and Zn/GO composites of GO concentration of 4 mgL⁻¹, 8 mgL⁻¹, 20 mgL⁻¹ and 40 mgL⁻¹ with (a) 1:1 (b) 1:2 ratio of GO:CTAB

Table 4.7: The critical load (L_{C1}) values for Zn/GO composites with different GO concentration, time and ratio of surfactant

Sample No.	GO	GO:CTAB	Time (min.)	L_{C1}
1	4	1:1	10	2.599
2			20	2.928
3			30	3.704
4		1:2	10	3.213
5			20	3.225
6			30	3.436
7	8	1:1	10	3.053
8			20	3.161
9			30	3.391
10		1:2	10	3.21
11			20	3.833
12			30	3.611
13	20	1:1	10	3.225
14			20	3.467
15			30	3.653
16		1:2	10	3.483
17			20	3.885
18			30	4.177
19	40	1:1	10	3.331
20			20	3.472
21			30	4.056
22		1:2	10	3.401
23			20	3.635
24			30	4.54

Figure 4.22 summarizes the results of the effect of temperature on L_C for 30 min coating time with 1:2 ratio of GO: CTAB, for 40mgL^{-1} of Zn/GO nanocomposites. The scratch tests conducted for these samples are mentioned in section 3. Table 4.8 shows the L_C values at different temperatures for Zn/GO composites. It must be noticed that the L_C values decreased with increasing temperature, gradually from RT to 350°C . The coating

properties were affected by temperatures and the coating remained intact until the indenter can break it away and reveal the substrate, as observed for samples at more than 300°C temperature (Jaume et al. 2014). However, Zn matrix softening is unlikely to be the sole determinant of failure load. Maledi et al. (2017) confirmed that as the temperature is increased, the residual stresses decreased in Zn coatings. It is expected that changes in the residual stress at the elevated temperature along with softening of the matrix together decide L_C values.

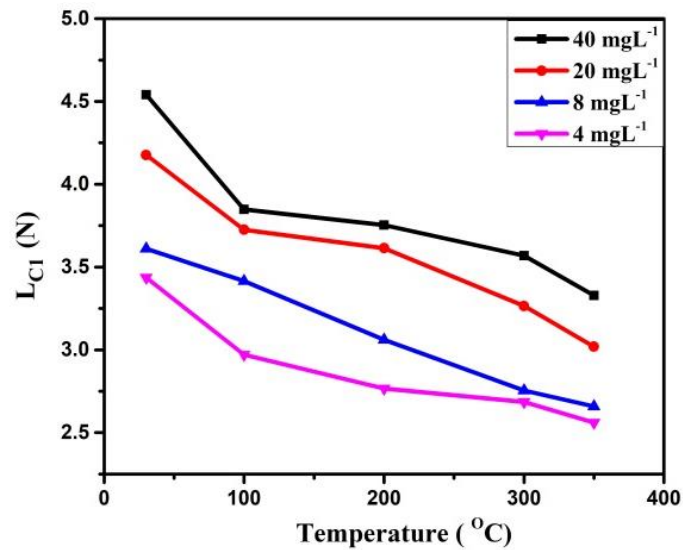


Figure 4.22: The critical load (L_c) values for Zn/GO composites with different GO concentration and 1:2 ratio of GO and CTAB at RT, 100°C, 200°C, 300°C & 350°C

Table 4.8: The L_C values for Zn/GO composites with different GO concentration and 1:2 ratio of GO and CTAB

GO (Concentration)	Cohesion strength (L_C)				
	RT	100°C	200°C	300°C	350°C
40 mgL ⁻¹	4.54	3.725	3.614	3.568	3.329
20 mgL ⁻¹	4.177	3.738	3.653	3.265	3.019
8 mgL ⁻¹	3.611	3.416	3.061	2.755	2.659
4 mgL ⁻¹	3.436	2.971	2.767	2.685	2.561

Fig. 4.23 shows the relation between coefficient of friction and graphene concentration. With the increase in the GO concentration, the friction coefficients of almost all composites increase in the initial run-in period due to the lack of proper contact between the tip and coating surface. As the proper contact is achieved between the tip and coating surface a steady-state regime from 0.1 to 0.3 is observed for all Zn/GO coated samples. The coefficient of friction between the above ranges is considered as a smooth surface. This is because of presence of GO in the matrix which act as a lubricating agent (Sarangi et al. 2020). The introduction of alloy elements in the Ni-B, Ti_xAl_xN , and Ti_6Al_4V matrix promotes an increase in adhesive strength by providing strong resistance to cracking and spallation under scratch testing (Masseoud et al. 2021; Ding et al. 2019; Artur et al. 2021). The driving forces for coating film damage in the scratch test can be a combination of elastic-plastic indentation stresses, frictional stresses, and residual internal stresses (Viktor P. Astakhov).

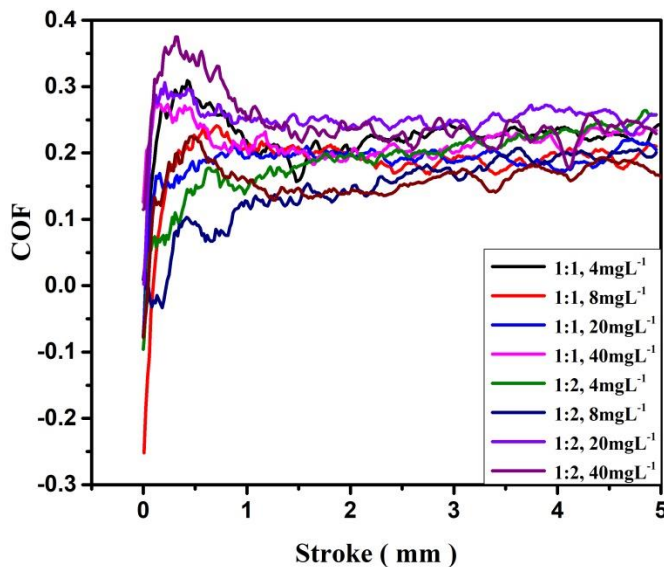


Figure 4.23: Curves of coefficient of friction with an increase of Scratch length for Zn/GO composites of increasing GO concentration with 1:1 & 1:2 ratio of GO:CTAB of coating time of 30 minutes

The coefficient of friction (COF) variation has been observed with respect to coating time and temperature at 40 mgL^{-1} concentration of GO as shown in Fig. 4.24. In case of GO:CTAB ratio, the coefficient of friction increasing linearly with coating time at both 1:1 and 1:2 of GO:CTAB. In these two cases, the 1:2 of GO:CTAB shows higher coefficient of friction compared to 1:1 of GO:CTAB (Fig. 4.24 a). This means the 1:2 of GO:CTAB composites surface have higher roughness due to higher GO present in the matrix compare to 1:1 of GO:CTAB composites for the same time of coatings. From Fig. 4.24 a, it is concluded that 12 min of coating with 40 mgL^{-1} GO (1:2 of GO:CTAB ratio) in the electrolyte will provide better scratch resistance with good surface finish.

The experimental results shown in Fig. 4.24 b indicate that temperature has a significant impact on the tribological behavior of the composite coating. For the same 1:2 ratio of GO:CTAB, 40 mgL^{-1} Zn/GO composites, the coefficient of friction shows a decreasing trend with increasing temperature. There is a sudden decrement observed in the COF upto 200°C whereas after 200°C COF remain nearly stable. This is because after 200°C , COF maintains stable because of the poor adhesion of GO in the Zn matrix after Zn reaches to half of its melting point. On the other side from RT to 200°C the reduction in the COF is due to overall temperature effect on the coated effect.

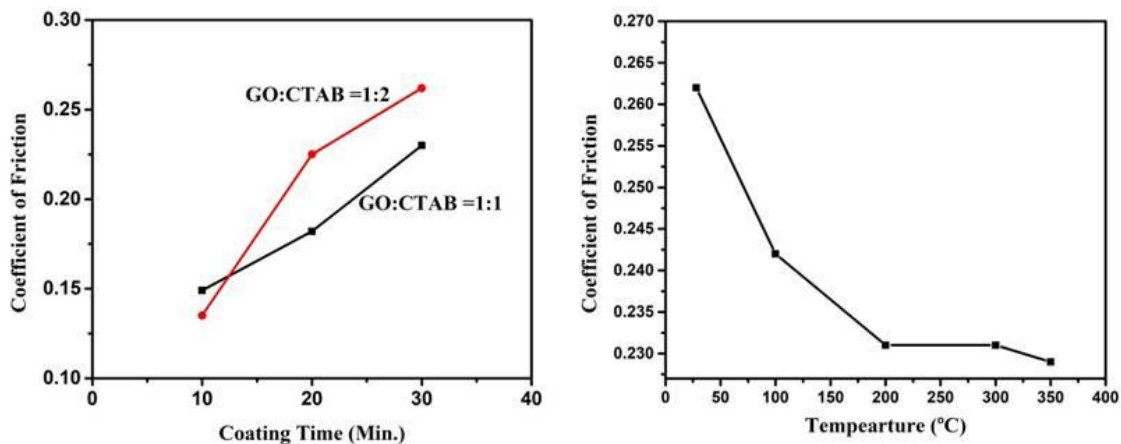


Figure 4.24: Coefficient of Friction variation with (a) coating time and (b) temperature at 40 mgL^{-1} concentration of GO

4.2.5 Impact strength

4.2.5.1 Deformation under varying pressure

The impact tests have been performed at test conditions as mentioned in section 3.4.2. The dynamic compressive loading was applied by varying pressure of 2 bar, 2.5 bar, 3 bar, 3.5 bar, and 4 bar for producing loadings at various rates through SHPB tests. The impact tests were carried out on uncoated stainless steel 304 and Zn/GO coated stainless steel 304 samples. The compressive stress and toughness of the material were examined due to the presence of GO coating on the stainless steel. The samples are positioned between the incident bar and transmitter bar, the striker bar is propelled by high-pressure gas gun and hits the incident bar. Grease is applied on the cross-sectional surface of the incident and transmitter bars to minimize the friction between sample and bars during the strike. The deformation history of the specimen is extracted from the produced signals in the strain gages which are mounted on the incident and transmission bars. Three tests were performed at each pressure condition; the final result was the average value of three samples.

Coating on stainless steel selected at 40 mgL^{-1} concentration of GO because it has shown good adhesion strength as per section 4.2.4. Figure 4.25 represents the averaged true stress-true strain curves of deformed pure stainless steel (Fig. 4.25 a) and Zn/GO coated samples (Fig. 4.25 b). It is observed from the graph that true stress-true strain curves significantly depend on pressure. Obtained true stress-true strain plots shows that at the same pressure impact, the Zn/GO coated stainless steel observed high maximum compression stress and high toughness compared to uncoated stainless steel samples. This is a good depiction of the stainless steel's high strength, i.e. resistance to indentation, due to the presence of GO in coating layer. The maximum stress values were calculated by taking average of three impact test at each pressure value of uncoated and Zn/GO composites samples from engineering stress and engineering strain were shown in Table 4.9. As the pressure increases from 2 bar to 4 bar the maximum compression stress of uncoated stainless steel and Zn/GO nano composites are increased by 721 MPa to 1121 MPa and 887 MPa to 1242 MPa respectively. Zn/GO composite shows that 10.7% increase in compressive strength at 4bar in comparison with uncoated sample. However,

in case of strain at constant thickness of GO coating on steel shows a significant increase in coated steel sample. The overall percent increase in strain for Zn/GO coated steel sample from 2bar (strain value: 20.7%) to 4 bar (strain value: 29.1%) pressure is 40.5%. This phenomenon was explained by Chen et al. (2021) that the strain in plastic deformation region strongly dependent on thickness of the coating. In our case we have performed the SHPB test at constant thickness which shows the increase in a strain as increase of impact pressure.

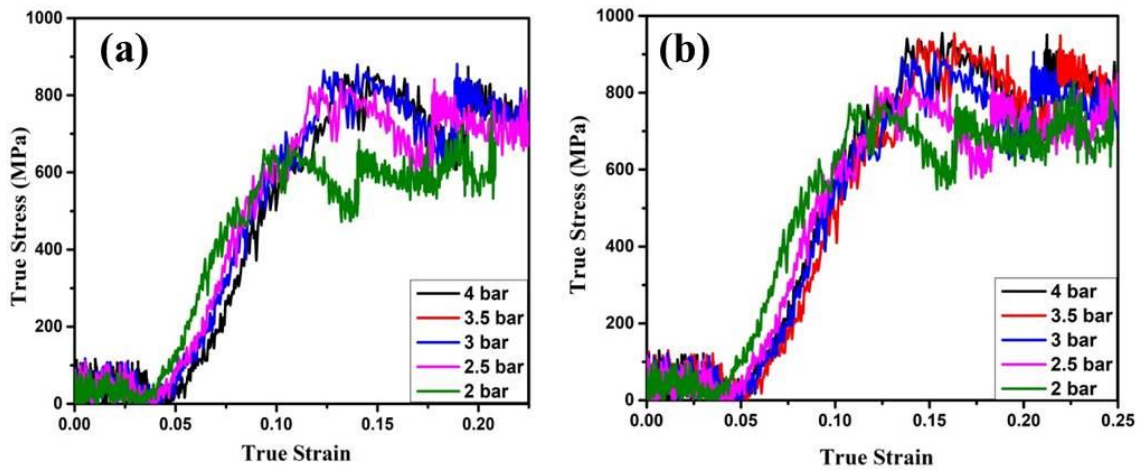


Figure 4.25: True stress-true strain plots obtained from uncoated and Zn/GO coated stainless steel samples at various pressures

The toughness is measured using stress-strain curve for all the uncoated and Zn/GO coated samples and reported in the Table 4.9. A significant change is observed in toughness from 2 bar to 4 bar pressure in both uncoated and Zn/GO coated conditions. From 2 bar to 4 bar pressure, almost 212% increase in toughness observed for uncoated samples. In the case of Zn/GO coated samples from 2 bar to 4 bar pressure, 105% increase in toughness observed. At the pressure 4bar, the Zn/GO coated samples have shown 22.9% higher toughness compared to uncoated samples due to the presence of GO in the coating. Higher toughness values observed for Zn/GO coatings samples for all pressures compared to uncoated samples. From the result, It is clearly understand that the presence of GO in the Zn matrix makes the coating tougher because of its unique structure. The bi-layered GO structure is stronger than diamond on impact which is

proved by Cellini et al. 2018. In our study due to the presences of few bi-layered GO and few layered GO flakes in the coating which makes composite stronger and tougher. Because of this reason, considerable improvement in maximum stress and toughness observed under impact loading in Zn/GO composite.

Table 4.9: The maximum stress and toughness values for uncoated and Zn/GO coated samples under various pressures

Pressure	Pure SS samples		Zn/GO coated	
	Maximum stress (MPa)	Toughness (MJm ⁻³)	Maximum stress (MPa)	Toughness (MJm ⁻³)
2bar	721	50	887	94
2.5bar	924	77	945	110
3bar	975	110	1046	143
3.5bar	1021	121	1203	166
4bar	1121	157	1242	193

Strain rate is the rate of deformation caused by strain in a material with respect to time. The strain rates are extremely dependent on the tensile strength and toughness properties of materials (Janjia Cui et al. 2019). The strain rates were calculated by using the equation 7, 8 & 9 as discussed in experimental techniques section 3.4.1 and plotted with respect to time as shown in Fig. 4.26. For the impact at gun pressure of 4bar, the observed strain rate values for uncoated samples are in the range of 1700-5200 s⁻¹. Whereas for Zn/GO coated samples at 4bar pressure, the strain rate values are in the range of 1800-5700 s⁻¹. The increased strain rates in the Zn/GO coated samples compared to pure stainless steel are due to interfacial bonding properties of hard coating layer of Zn/GO on the stainless steel substrate. As the stress increases the strain rate also increases in the composites which is good accordance with the literature (Hui et al. 2021; Yuan J et al. 1998). The higher strain rates are also having significant effect on microstructural changes in the both uncoated and Zn/GO coated samples under impact loading.

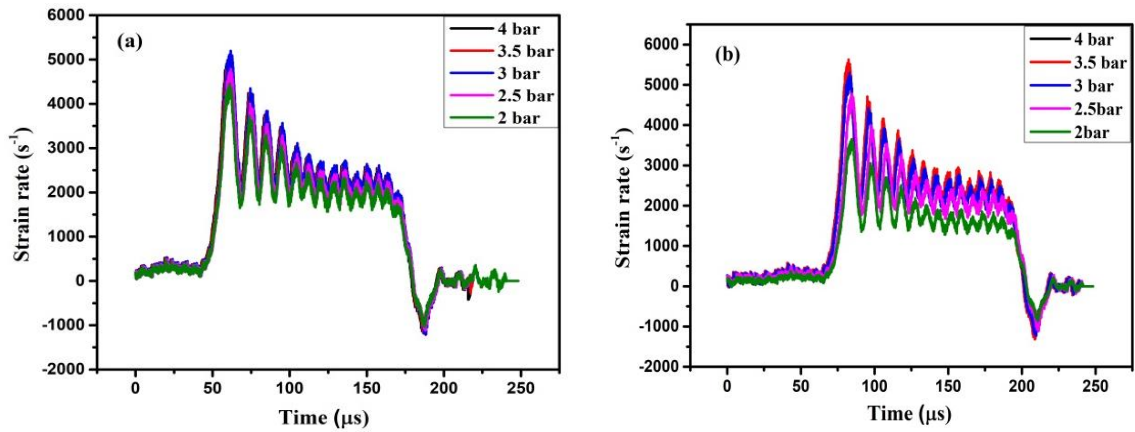


Figure 4.26: Strain rate vs. time plots obtained from (a) uncoated and (b) Zn/GO coated stainless steel samples at various pressures

4.2.5.2 Deformation under varying temperature

The dynamic compressive loading was applied by the varying temperature of 100°C, 200°C, and 300°C respectively at various pressures (2bar, 3bar & 4bar) through SHPB tests. These tests were carried out on Zn/GO coated and uncoated stainless steel samples and results were compared with samples that tested at room temperature (RT). The true stress-true strain plots to observe the variations of maximum stresses and toughness along with the temperature were presented at 2bar, 3bar, and 4bar in Fig.4.27 (a), (b) and (c) respectively. At constant pressure, from 100°C to 300°C, the maximum stress and toughness decreased compared to the RT as shown in Fig.4.28 and Fig.4.29. All the maximum stress and toughness values of Zn/GO coated samples were compared with the uncoated stainless steel samples which were listed in Table 4.10.

Based on the experimental results, the maximum stress and toughness of uncoated as well as Zn/GO coated stainless steel samples declines by increasing the temperature from RT to 300°C as shown in Fig. 4.27. As pressure increases from 2 bar to 4 bar, for Zn/GO coated sample the maximum stress decreased by 25%, 28% and 32% from RT to 300°C. Whereas, in case of uncoated and Zn/GO coated samples it is observed that the maximum stress and toughness value shows significant change from RT to 100°C. However there is no significant change is observed in all the samples when temperature raise from 100°C

to 300°C. Which shows that the presence of GO in the Zn matrix does not give any benefit on impact compressive stress and toughness value at elevated temperature.

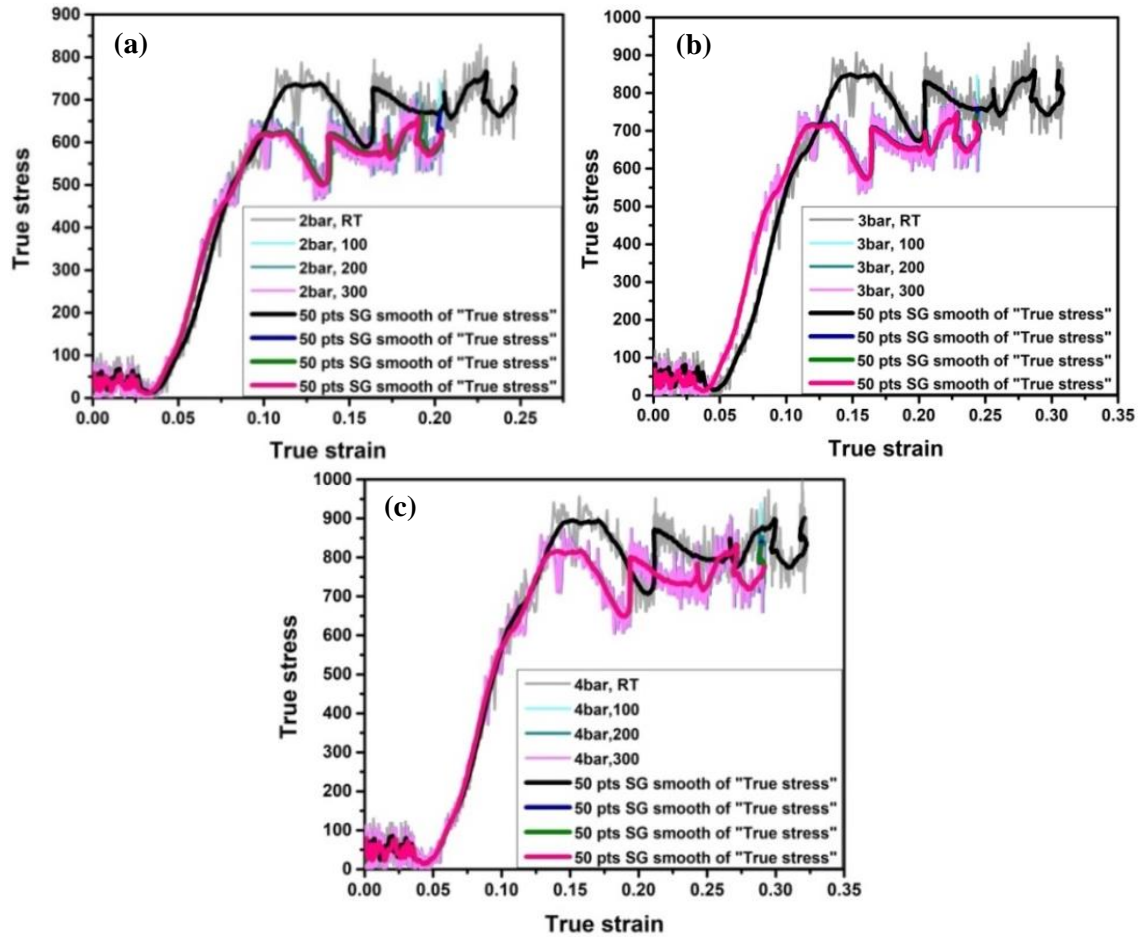


Figure 4.27: The true stress-true strain plots of Zn/GO coated samples at gun pressure of (a) 2bar (b) 3bar and (c) 4bar respectively by varying the temperature

4.2.5.3 Microstructural study of the Zn/GO coating after impact

Post-impact tests analysis were performed by FESEM in order to understand the mechanism of the Zn/GO coating effect on strength of the stainless steel under impact loading. Visual inspection and optical microstructures confirms that no cracks in the Zn/GO coating as shown in Fig. 4.28. It was observed after the impact at surface level which indicates the coating on the stainless steel is having good adhesion with the substrate. Fig. 4.29 shows the FESEM micrographs of transverse cross section of pure

stainless steel and Zn/GO coated stainless samples before and after impact loading of 4bar pressure. Fig. 4.29a shows the pure stainless steel cross sectional micrograph before impact loading which is taken as reference to compare changes with impact loading samples.

Table 4.10: The maximum stress values of Zn/GO coated and uncoated stainless steel samples

Pressure	Temperature	Uncoated		Zn/GO coated	
		Maximum Stress (MPa)	Toughness (MJm ⁻³)	Maximum Stress (MPa)	Toughness (MJm ⁻³)
2bar	RT	721	50	887	94
	100°C	658	80	669	83
	200°C	662	83	662	84
	300°C	663	84	657	84
3bar	RT	975	110	1046	143
	100°C	755	115	754	116
	200°C	755	116	746	115
	300°C	747	115	745	114
4bar	RT	1121	157	1242	193
	100°C	855	140	840	156
	200°C	830	153	833	156
	300°C	827	155	833	158

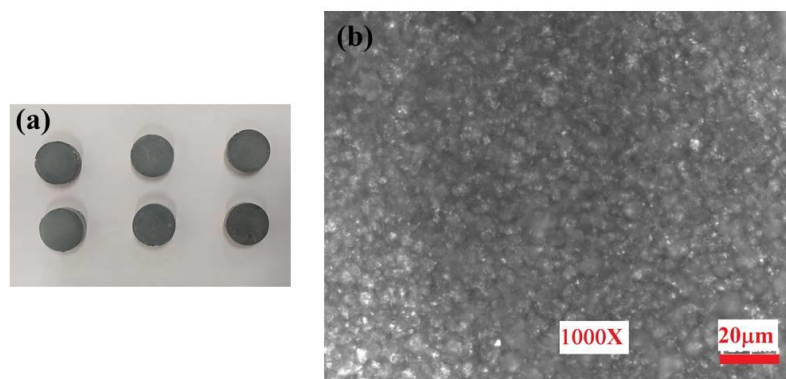


Figure 4.28: The (a) visual picture and (b) microstructure of Zn/GO coating on stainless steel after SHPB experiment

Fig. 4.29 (a) shows a good clear grain boundary without any twin formation, whereas under impact loading clear grain boundary and large number of twins were observed and spacing between the twins was 260 nm as shown in Fig.4.29(b). In case of Zn/GO coated sample less number of twins with twin spacing 170 nm was observed as shown in Fig.4.29(c). As can be seen in Fig. 4.29(d), there were significantly fewer twins observed at 300°C and 4bar pressure than at RT.

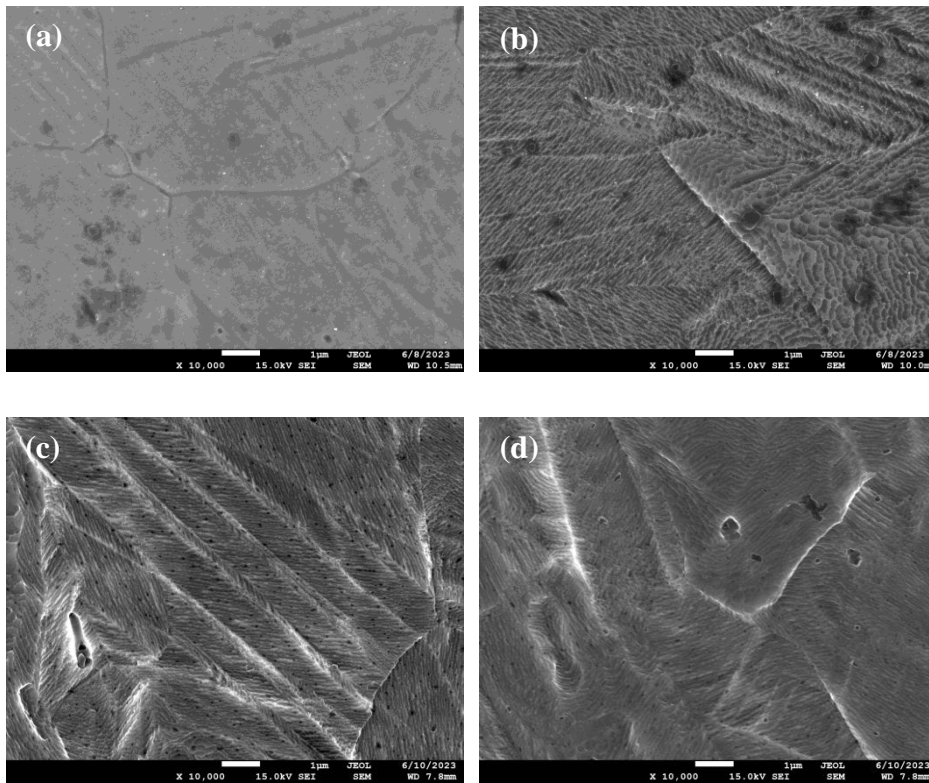


Figure 4.29: The FESEM microstructures of (a) unimpacted (b) impacted stainless steel (c) Zn/GO coated stainless steel (d) at 300°C samples after the impact pressure of 4bar

4.2.6 Residual stresses

The residual stresses in the pure Zn coating and Zn/GO nanocomposites were examined through $\sin^2\psi$ method. The residual stresses are calculated for the Zn phase because it acts as a matrix in the coating. The residual stress experiments have been done at 5 different points in each sample and analyzed through stress plus software to get the

accurate average value of residual stress in the sample. Table 4.11 shows the residual stress values of Zn/GO nanocomposites with 1:2 ratio of GO:CTAB at different concentrations of GO, coated for 30 min. In all samples, the observed residual stresses are compressive in nature. As reported by Oladijo et al. (2012), the compressive stresses are beneficial compared to tensile stresses, but excessive compressive stresses can cause problems like buckling, which can lead to coating delamination. Compressive stresses in the coatings have been shown to provide better wear (Mathabatha et al. 2017), coating adhesion, and mechanical properties (Oladijo et al. 2018).

Table 4.11 presents values of the residual stresses of Zn/GO nanocomposites. It is observed that as the concentration of GO increases the residual stresses decreased and were found least for 40 mgL^{-1} GO of Zn/GO nanocomposite. Also, Shokrieh et al. concluded that the amount of residual stress depends on the concentration of graphene in carbon epoxy composites (Shokrieh and Kondori 2020). The addition of graphene in the matrix contributes to the release of residual stress; as reported in Ti6Al4V and carbon/epoxy laminated composites (Shokrieh and Kondori 2020; ZhouFan et al. 2019). Jalal et al.(2022) and Anna Goral et al. (2017) concluded that the incorporation of Al_2O_3 nanoparticles reduced the level of residual stresses in the Ni film. The residual stresses in 4 mgL^{-1} concentration of GO of Zn/GO nanocomposites are observed to be low compared to the trend. This low value in residual stresses could also be caused by the following reasons.

1. The kinetic impact behavior of the Zn^{2+} ions and GO platelets in the electrolyte changes depending on its composition.
2. A slight difference in the surface roughness of the substrate during deposition plays main role in nucleation; coating growth and entrapment GO into the coating. All contributes to residual stresses.

Table 4.11: Residual stress values of Zn/GO composites coatings at various GO concentrations

Sample No.	GO concentration (mgL ⁻¹)	Average residual stress ((r ₁₁ + r ₂₂)/2) (MPa)
1	Pure SS304 steel	-340.7
2	Pure Zn	-32.14
3	4	-13.52
4	8	-20.24
5	20	-15.54
6	40	-11.48

The critical load data observed in the scratch test is associated with the residual stress values for the Zn/GO nanocomposites. It is observed that L_{C1} values decrease for the coating with higher residual stress. The pure Zn coating which is observed to have higher residual stress values exhibits low adhesive and cohesion strength. Similarly, Zn/GO nanocomposites with GO concentration of 40 mgL⁻¹ have less residual stress and higher adhesion and cohesion strength. Laugier et al. (1984) analyzed the scratch adhesion process from the fracture mechanics perspective and associated the critical load in the scratch test with the development of critical stored elastic energy necessary to overcome the formation of a free surface. By this, we can confirm that the compressive stresses developed prior to the indenter would be expected to increase compressive stresses and result in coating failure at lower critical loads (White et al. 1993).

CHAPTER 5

CONCLUSIONS AND SCOPE OF FUTURE WORK

5.1 CONCLUSIONS

In this study we have focused on preparation of metal/carbon nanomaterial composites by electrodeposition technique. We have prepared two types of metal/ CNMs composites namely, Cu/CNT and Zn/GO composites. The composite physical property was evaluated by several test methods. The conclusion for individual metal/CNMs is discussed below

(a) Cu/CNT Composites

1. Good quality Cu/CNT composites were prepared successfully using electrodeposition technique. This composite shows remarkable tensile strength, hardness and corrosion resistance. After the tensile test, the Cu/CNT coating still intact with the substrate means that the bonding of Cu atom with substrate as well as CNT with Cu atom is extremely good. This signifies that load transfer among the Cu matrix and CNT is good.
2. We demonstrated that electrodeposited Cu/CNT composite is capable of achieving good heat transfer rate. In the electrochemical bath CNTs which is axially aligned with the electrode have better chance to deposit along the axis of electrode. As a result better heat transfer rate was achieved.

(b) Zn/GO Composites

1. High quality Zn/GO nanocomposites prepared successfully using electrodeposition technique and high adhesion strength achieved with 1:2 ratio of GO and CTAB recorded at 1g concentration of GO because of the alignment and distribution of GO in the Zn matrix.
2. The Zn/GO composite impact test experiments reported that compression stress and toughness values are strongly dependent on pressure and temperature. It shows that 10.7% increase in compressive strength at 4bar in comparison with uncoated sample and no significant change observed at higher temperatures. The

post-impact microstructures confirmed that the Zn/GO coating layer has strong interface bonding with the steel surface.

5.2 SCOPE OF FUTURE WORK

- Experimental investigations can be carried out on Cu/CNT or GO by electroless deposition to improve heat transfer rate in the nanocomposites. Because the electroless deposition also includes atomic level deposition on the substrate which can give homogeneity good interfacial bonding between CNMs and metal.
- In this study the Zn/GO nanocomposites prepared by multi-layer graphene oxide and observed impact resistance by increasing the pressure from 2 bar to 4 bar. There is a future scope by using bi-layer of graphene which can give better impact resistance than multi-layer GO. The reason attributed to bi-layer graphene is more stronger than diamond on impact which is proven by several scientists.
- Further study includes changing the different surfactant with at various concentrations can improve the dispersion of CNMs in the electrolyte and expected in better physical properties of nanocomposites.

LIST OF PUBLICATIONS

1. K. Divya Bharathi, M. R. Rahman, Sunita Choudhary, and S. B. Arya “Development and characterization of Cu/MWCNT composite prepared by electrodeposition technique” AIPC (SCOPUS) 2247, 040019 (2020); DOI: 10.1063/5.0010560
2. K Divya Bharathi, M. R. Rahman, Ajay Kumar Yadav, Rudramurthy BV and Devadas Bhat P “Optimized heat transfer rate in Cu/CNT nanocomposite prepared by electrodeposition technique” ECS Advances, (2023) 2 01001 DOI: 10.1149/2754-2734/acb2dd
3. Presented in International conference on Smart and Sustainable Developments in Materials, Manufacturing and Energy Engineering (SME-2019), NITTE, NMAM Institute of Technology 23rd-24th May, 2019.
4. K Divya Bharathi, M. R. Rahman¹, Udaya Bhat K, Devadas Bhat P “Effect Of Temperature On The Cohesion Strength Of Zn/GO Hybrid Nano Films Deposited On 304 Stainless Steel Using Electrodeposition Technique” (submitted)
5. K Divya Bharathi, M. R. Rahman¹, Sharnappa Joldarashi, Udaya Bhat K, Devadas Bhat P “Combined effect of elevated temperature and pressure on high strain rates of Zn/GO nanocomposite by SHPB for armor applications” (submitted)

REFERENCES

- Aliyu, A., and Srivastava, C. (2021). "Correlation between growth texture, crystallite size, lattice strain and corrosion behavior of copper-carbon nanotube composite coatings." *Surf. Coatings Technol.*, 405(September 2020).
- Arai, S., Saito, T., and Endo, M. (2007). "Low-Internal-Stress Nickel Multiwalled Carbon Nanotube Composite Electrodeposited from a Sulfamate Bath." *J. Electrochem. Soc.*, 154(10), D530.
- Azar, M. M. K., Gugtapeh, H. S., & Rezaei, M. (2020). Evaluation of corrosion protection performance of electroplated zinc and zinc-graphene oxide nanocomposite coatings in air saturated 3.5 wt.% NaCl solution. *Colloids and Surfaces A: Physicochemical and Engineering Aspects*, 601, 125051.
- Bull, S. J. (1991). "Failure modes in scratch adhesion testing." *Surf. Coatings Technol.*, 50(1), 25–32.
- Berndt, C. C., & Lavernia, E. J. (1998). Thermal spray processing of nanoscale materials-A conference report with extended abstract. *Journal of Thermal Spray Technology*, 7(3), 411.
- Chai, G., Sun, Y., & Chen, Q. (2008). Mechanical properties of carbon nanotube–copper nanocomposites. *Journal of Micromechanics and Microengineering*, 18(3), 035013.
- Chai, G., Chen, Q., (2010) "Characterization study of the thermal conductivity of carbon nanotube copper nanocomposites." *Journal of composite materials* (44) 2863-2873.
- Cheng, B., Bao, R., Yi, J., Li, C., Tao, J., Liu, Y., Tan, S., and You, X. (2017). "Interface optimization of CNT/Cu composite by forming TiC nanoprecipitation and low interface energy structure via spark plasma sintering." *J. Alloys Compd.*, 722, 852–858.
- Choi, J. H., Dhakal, D. R., Kshetri, Y. K., Chaudhary, B., Joshi, B., Lee, S. W., & Kim, T. H. (2022). "Role of surfactants on particle deposition, wear, and corrosion behavior of TaC particle incorporated electroless nickel-phosphorus coating." *Progress in Natural Science: Materials International*, 32(5), 655-663.

- Chu, K., Wu, Q., Jia, C., Liang, X., Nie, J., Tian, W., Gai, G., and Guo, H. (2010). "Fabrication and effective thermal conductivity of multi-walled carbon nanotubes reinforced Cu matrix composites for heat sink applications." *Compos. Sci. Technol.*, 70(2), 298–304.
- Cui, J., Wang, S., Wang, S., Li, G., Wang, P., & Liang, C. (2019). The effects of strain rates on mechanical properties and failure behavior of long glass fiber reinforced thermoplastic composites. *Polymers*, 11(12), 2019.
- Daoush, W. M., Lim, B. K., Mo, C. B., Nam, D. H., & Hong, S. H. (2009). Electrical and mechanical properties of carbon nanotube reinforced copper nanocomposites fabricated by electroless deposition process. *Materials Science and Engineering: A*, 513, 247-253.
- Darabi, M., Rajabi, M., and Nasiri, N. (2020). "Microstructural, mechanical and thermal properties of microwave sintered Cu-MWCNT nanocomposites." *J. Alloys Compd.*, 822, 153675.
- Delavari, M., Salarvand, A., Rahi, A., and Shahri, F. (1970). "The effect of powder metallurgy process parameters on mechanical properties of micro and nano-iron powder." *Int. J. Eng. Sci. Technol.*, 3(9), 86–94.
- Ding, Z., He, Q., Ding, Z., Liao, C., Chen, D., and Ou, L. (2019). "Fabrication and performance of ZnO doped tantalum oxide multilayer composite coatings on Ti6Al4V for orthopedic application." *Nanomaterials*, 9(5).
- Endo, M., Hayashi, T., Itoh, I., Kim, Y. A., Shimamoto, D., Muramatsu, H., Shimizu, Y., Morimoto, S., Terrones, M., Iino, S., and Koide, S. (2008). "An anticorrosive magnesium/carbon nanotube composite." *Appl. Phys. Lett.*, 92(6), 90–93.
- Fan, Z., Zhang, K., Liu, J. Y., Hu, M., & Yang, C. F. (2020). Microstructure and mechanical properties of Ti6Al4V alloy and sapphire joint brazed with graphene-AgCuTi. *Materials Research Express*, 6(12), 1265k4.
- Fatemi, S. M., and Foroutan, M. (2016). "Recent developments concerning the dispersion of carbon nanotubes in surfactant/polymer systems by MD simulation." *J. Nanostructure Chem.*, 6(1), 29–40.

- Fauchais, P. (2004). "Understanding plasma spraying." *J. Phys. D. Appl. Phys.*, 37(9).
- Guo, H., Zhou, Z., Gu, M., Yu, A., Ling, X., & Yao, W. (2021). "Preparation of impact-resistant functional polyurea coatings and effect of γ -ray irradiation on its microstructure and performance." *Progress in Organic Coatings*, 161, 106521.
- García-Aguirre, C. A., Domínguez-Ríos, C., Torres-Sánchez, R., Román-Aguirre, M., Holguín-Momaca, J. T., and Aguilar-Elguézabal, A. (2015). "Microstructure and transmission electron microscopy characterization of electroless Ni-B thin films deposited on MWCNTs." *Surf. Coatings Technol.*, 282, 107–114.
- Gardea, F., and Lagoudas, D. C. (2014). "Characterization of electrical and thermal properties of carbon nanotube/epoxy composites." *Compos. Part B Eng.*, 56, 611–620.
- Gültekin, D., and Akbulut, H. (2016). "Raman studies of ZnO products synthesized by solution based methods." *Acta Phys. Pol. A*, 129(4), 803–805.
- Hidayah, N. M. S., Liu, W. W., Lai, C. W., Noriman, N. Z., Khe, C. S., Hashim, U., and Lee, H. C. (2017). "Comparison on graphite, graphene oxide and reduced graphene oxide: Synthesis and characterization." *AIP Conf. Proc.*, 1892.
- Hong, R., Ji, J., Tao, C., Zhang, D., and Zhang, D. (2017). "Fabrication of Au/graphene oxide/Ag sandwich structure thin film and its tunable energetics and tailorable optical properties." *AIMS Mater. Sci.*, 4(1), 223–230.
- Huang, J. H., Yu, K. J., Sit, P., and Yu, G. P. (2006). "Heat treatment of nanocrystalline TiN films deposited by unbalanced magnetron sputtering." *Surf. Coatings Technol.*, 200(14–15), 4291–4299.
- Hwang, J., Yoon, T., Jin, S. H., Lee, J., Kim, T. S., Hong, S. H., and Jeon, S. (2013). "Enhanced mechanical properties of graphene/copper nanocomposites using a molecular-level mixing process." *Adv. Mater.*, 25(46), 6724–6729.
- James Lankford, J. (1993). "Characterization of Mechanical Damage Mechanisms in Ceramic and Polymeric Matrix Composite Materials."
- Je, J. H., Gyarmati, E., & Naoumidis, A. (1986). "Scratch adhesion test of reactively

sputtered TiN coatings on a soft substrate." *Thin Solid Films*, 136(1), 57-67.

Ji, T., Feng, Y., Qin, M., and Feng, W. (2016). "Thermal conducting properties of aligned carbon nanotubes and their polymer composites." *Compos. Part A Appl. Sci. Manuf.*, 91, 351–369.

Johra, F. T., Lee, J. W., & Jung, W. G. (2014). Facile and safe graphene preparation on solution based platform. *Journal of Industrial and Engineering Chemistry*, 20(5), 2883-2887.

Kabiri, S., Degryse, F., Tran, D. N. H., Silva, R. C. Da, McLaughlin, M. J., and Losic, D. (2017). "Graphene Oxide: A New Carrier for Slow Release of Plant Micronutrients." *ACS Appl. Mater. Interfaces*, 9(49), 43325–43335.

Karolina.Jurkiewicz, Mirosława Pawlyta, and Andrzej Burian (2018) "Structure of carbon materials explored by local transmission electron microscopy and global powder diffraction probes." *C 4*, no. 4: 68.

Kim, D. H., Kim, Y. S., Wu, J., Liu, Z., Song, J., Kim, H. S., Huang, Y. Y., Hwang, K. C., and Rogers, J. A. (2009). "Ultrathin silicon circuits with strain-isolation layers and mesh layouts for high-performance electronics on fabric, vinyl, leather, and paper." *Adv. Mater.*, 21(36), 3703–3707.

Kim, K. T., Cha, S. I., Hong, S. H., & Hong, S. H. (2006). Microstructures and tensile behavior of carbon nanotube reinforced Cu matrix nanocomposites. *Materials Science and Engineering: A*, 430(1-2), 27-33.

Kudin, K. N., Ozbas, B., Schniepp, H. C., Prud'homme, R. K., Aksay, I. A., and Car, R. (2008). "Raman spectra of graphite oxide and functionalized graphene sheets." *Nano Lett.*, 8(1), 36–41.

Li, A., Yu, J., Lin, J., Chen, M., Wang, X., and Guo, L. (2020). "Increased O 2p State Density Enabling Significant Photoinduced Charge Transfer for Surface-Enhanced Raman Scattering of Amorphous Zn(OH)₂." *J. Phys. Chem. Lett.*, 11(5), 1859–1866.

Li, L., Bao, R., Yi, J., Liu, L., & Mao, S. (2018). Preparation of CNT/Cu nano composite

powder with uniform dispersion and strong interface bonding by SP method. *Powder Technology*, 325, 107-112.

Li, L., Wang, R., Zhao, H., Zhang, H., and Yan, R. (2021). “Combined effects of elevated temperatures and high strain rates on compressive performance of S30408 austenitic stainless steel.” *Structures*, 34(June), 1–9.

Lim, B. K., Mo, C. B., Nam, D. H., and Hong, S. H. (2010). “Mechanical and electrical properties of carbon nanotube/Cu nanocomposites by molecular-level mixing and controlled oxidation process.” *J. Nanosci. Nanotechnol.*, 10(1), 78–84.

Lin, C. H., Wang, H. L., and Hon, M. H. (1996). “The effect of residual stress on the adhesion of PECVD-coated aluminum oxide film on glass.” *Thin Solid Films*, 283(1–2), 171–174.

Lin, Z., Mcnamara, A., Liu, Y., Moon, K. S., & Wong, C. P. (2014). Exfoliated hexagonal boron nitride-based polymer nanocomposite with enhanced thermal conductivity for electronic encapsulation. *Composites Science and Technology*, 90, 123-128.

Long, X. J., Li, B., Wang, L., Huang, J. Y., Zhu, J., and Luo, S. N. (2016). “Shock response of Cu/graphene nanolayered composites.” *Carbon N. Y.*, 103, 457–463.

Low C.T.J., Wills R.G.A., Walls F.C " Electrodeposition of Composite Coatings containing Nano particles in a metal deposit" *Surface Coatings and Technology* 201, 371-383 (2006)

M Y, R., and Srivastava, C. (2019). “Microstructure and corrosion properties of zinc-graphene oxide composite coatings.” *Corros. Sci.*, 152(March), 234–248.

Mai, Y. J., Zhou, M. P., Ling, H. J., Chen, F. X., Lian, W. Q., and Jie, X. H. (2018). “Surfactant-free electrodeposition of reduced graphene oxide/copper composite coatings with enhanced wear resistance.” *Appl. Surf. Sci.*, 433, 232–239.

Marconnet, A. M., Yamamoto, N., Panzer, M. A., Wardle, B. L., and Goodson, K. E. (2011). “Thermal conduction in aligned carbon nanotube-polymer nanocomposites with high packing density.” *ACS Nano*, 5(6), 4818–4825.

- Masseoud, M., Antar, Z., Fridrici, V., Barletta, M., & Elleuch, K. (2021). Tribological properties of Ni-B-TiO₂ sol composite coating elaborated by sol-enhanced process: abrasive wear and impact wear. *Journal of Materials Research and Technology*, 13, 857-871.
- Mathabatha, M. H., Popoola, A. P. I., and Oladijo, O. P. (2017). "Residual stresses and corrosion performance of plasma sprayed zinc-based alloy coating on mild steel substrate." *Surf. Coatings Technol.*, 318, 293–298.
- Md Ali, A., Omar, M. Z., Hashim, H., Salleh, M. S., and Mohamed, I. F. (2021). "Recent development in graphene-reinforced aluminium matrix composite: A review." *Rev. Adv. Mater. Sci.*, 60(1), 801–817.
- Muench, F. (2021). "Electroless Plating of Metal Nanomaterials." *ChemElectroChem*, 8(16), 2993–3012.
- Muxi, L., Yuhong, Z., Liwen, C., Jianquan, L., Ting, Z., & Hua, H. (2018). Research progress on preparation technology of graphene-reinforced aluminum matrix composites. *Materials Research Express*, 6(3), 032002.
- Oladijo O.P, Venter A.M., Cornish L.A, Sacks N " X-Ray Diffraction Measurement of Residual stress in WC-Co thermally sprayed coatings onto metal substrates" *Surf. Coatings Tech.* 206, 4725-4729 (2012).
- Oladijo O.P, Mathabatha M.H, Popoola A.P.I., Ntsoane T.P " Characterization and Corrosion Behavior of Plasma Sprayed Zn-Sn alloy coating on mild steel" *Surf. Coatings Tech.* 352, 654-661 (2018).
- Ollendorf, H., & Schneider, D. (1999). "A comparative study of adhesion test methods for hard coatings." *Surface and Coatings Technology*, 113(1-2), 86-102.
- Patzke, G. R., Krumeich, F., and Nesper, R. (2002). "Oxidic nanotubes and nanorods - Anisotropic modules for a future nanotechnology." *Angew. Chemie - Int. Ed.*, 41(14), 2446–2461.
- Pejryd, L., Wigren, J., Greving, D. J., Shadley, J. R., and Rybicki, E. F. (1995). "Residual

stresses as a factor in the selection of tungsten carbide coatings for a jet engine application.” *J. Therm. Spray Technol.*, 4(3), 268–274.

Pina, J., Dias, A., and Lebrun, J. L. (2003). “Study by X-ray diffraction and mechanical analysis of the residual stress generation during thermal spraying.” *Mater. Sci. Eng. A*, 347(1–2), 21–31.

Rohatgi, P. (1991). Cast aluminum-matrix composites for automotive applications. *Jom*, 43, 10-15.

Pujante, J., Vilaseca, M., Casellas, D., and Riera, M. D. (2014). “High temperature scratch testing of hard PVD coatings deposited on surface treated tool steel.” *Surf. Coatings Technol.*, 254, 352–357.

Radhakrishnan. P., Arun Kumar K.,(2016) "Corrosion And Hardness Behaviour Of Copper Metal Matrix Composite." *IJARMATE*, Vol. 2, Special Issue 12 2454-9762.

Randall, N. X., & Consiglio, R. (2000). "Nanoscratch tester for thin film mechanical properties characterization." *Review of Scientific Instruments*, 71(7), 2796-2799.

Randall, N. X., Favaro, G., & Frankel, C. H. (2001). "The effect of intrinsic parameters on the critical load as measured with the scratch test method." *Surface and Coatings Technology*, 137(2-3), 146-151.

Rasel Das, Sharifah Bee Abd Hamid, Md Equb Ali, Seeram Ramakrishna, and Wu Yongzhi. "Carbon nanotubes characterization by X-ray powder diffraction—a review." *Current Nanoscience* 11, no. 1 (2015): 23-35.

Rawal, Suraj P. "Metal-matrix composites for space applications." *Jom* 53, no. 4 (2001): 14-17.

Salvetat, J. P., Bonard, J. M., Thomson, N. H., Kulik, A. J., Forro, L., Benoit, W., & Zuppiroli, L. (1999). "Mechanical properties of carbon nanotubes." *Applied Physics A*, 69, 255-260.

Sarangi, C. K., Sahu, B. P., Mishra, B. K., & Mitra, R. (2020). "Pulse electrodeposition and characterization of graphene oxide particle-reinforced Ni–W alloy matrix

nanocomposite coatings." *Journal of Applied Electrochemistry*, 50, 265-279.

Senthil Saravanan, M. S., Kumaresh Babu, S. P., and Sivaprasad, K. (2014). "Mechanical properties and corrosion behavior of carbon nanotubes reinforced AA 4032 nanocomposites." *Exp. Tech.*, 38(1), 48–52.

Skiba, S., Faure, L., Philippon, S., and Papisidero, J. (2020). "Experimental Investigation of the Mechanical Behavior of an AlSi-PE Abradable Coating at High Strain Rates for a Large Range of Temperatures." *J. Dyn. Behav. Mater.*, 6(2), 213–223.

Stewart, D. A., Shipway, P. H., and McCartney, D. G. (1998). "Influence of heat treatment on the abrasive wear behaviour of HVOF sprayed WC-Co coatings." *Surf. Coatings Technol.*, 105(1–2), 13–24.

Sun, W. chang, Zhang, P., Zhao, K., Tian, M. miao, and Wang, Y. (2015). "Effect of graphite concentration on the friction and wear of Ni-Al₂O₃/graphite composite coatings by a combination of electrophoresis and electrodeposition." *Wear*, 342–343, 172–180.

Tian, J., Liu, S., Li, H., Wang, L., Zhang, Y., Luo, Y., Asiri, A. M., Al-Youbi, A. O., and Sun, X. (2012). "One-step preparation of ZnO nanoparticle-decorated reduced graphene oxide composites and their application to photocurrent generation." *RSC Adv.*, 2(4), 1318–1321.

Tian, W. M., Li, S. M., Wang, B., Chen, X., Liu, J. H., & Yu, M. (2016). Graphene-reinforced aluminum matrix composites prepared by spark plasma sintering. *International Journal of Minerals, Metallurgy, and Materials*, 23, 723-729.

Tran, T. Q., Lee, J. K. Y., Chinnappan, A., Jayathilaka, W. A. D. M., Ji, D., Kumar, V. V., and Ramakrishna, S. (2020). "Strong, lightweight, and highly conductive CNT/Au/Cu wires from sputtering and electroplating methods." *J. Mater. Sci. Technol.*, 40, 99–106.

Treacy, M. M. J., Ebbesen, T. W., and Gibson, J. M. (1996). "Exceptionally high Young's modulus observed for individual carbon nanotubes.pdf."

Trinh, P. Van, Bui, H. T., Tran, B. T., Tu, N. Van, Le, D. Q., Than, X. T., Chuc, N. Van, Doan, D. P., and Phan, N. M. (2011). "The effect of sintering temperature on the

mechanical properties of a Cu/CNT nanocomposite prepared via a powder metallurgy method.” *Adv. Nat. Sci. Nanosci. Nanotechnol.*, 2(1).

Tripathi, M., Parthasarathy, S., Kumar, D., Chandel, P., Sharma, P., and Roy, P. K. (2020). “Strain rate sensitivity of polyurea coatings: Viscous and elastic contributions.” *Polym. Test.*, 86(November 2019), 106488.

Wang, J., Chen, G., Wang, M., and Chatrathi, M. P. (2004). “Carbon-nanotube/copper composite electrodes for capillary electrophoresis microchip detection of carbohydrates.” *Analyst*, 129(6), 512–515.

Wang, L., Yang, Z., Cui, Y., Wei, B., Xu, S., Sheng, J., .& Fei, W. (2017). Graphene-copper composite with micro-layered grains and ultrahigh strength. *Scientific Reports*, 7(1), 1-10.

Wang, P., Cao, Q., Wang, H., Liu, S., Chen, Y., and Peng, Q. (2021). “CNT-sandwiched copper composites as super thermal conductors for heat management.” *Phys. E Low-Dimensional Syst. Nanostructures*, 128(August 2020).

White, R. L., Nelson, J., & Gerberich, W. W. (1993). "Residual Stress Effects in the Scratch Adhesion Testing of Tantalum Thin Films." *MRS Online Proceedings Library (OPL)*, 308.

Wu, Y. C., Shao, J. L., and Zhan, H. (2021). “Damage and self-healing characteristics of monolayer graphene enhanced Cu under ballistic impact.” *Mech. Mater.*, 155(September 2020).

Xu, T., Zhang, L., Cheng, H., and Zhu, Y. (2011). “Significantly enhanced photocatalytic performance of ZnO via graphene hybridization and the mechanism study.” *Appl. Catal. B Environ.*, 101(3–4), 382–387.

Yang, J., and Schaller, R. (2004). “Mechanical spectroscopy of Mg reinforced with Al₂O₃ short fibers and C nanotubes.” *Mater. Sci. Eng. A*, 370(1–2), 512–515.

Yang, Y. L., Wang, Y. D., Ren, Y., He, C. S., Deng, J. N., Nan, J., Chen, J. G., and Zuo, L. (2008). “Single-walled carbon nanotube-reinforced copper composite coatings

prepared by electrodeposition under ultrasonic field.” *Mater. Lett.*, 62(1), 47–50.

Yuan, J., Takeda, N., Song, D. Y., & Waas, A. M. (1999). "Experimental study on dynamic compressive failure of unidirectional CFRP composites." *Journal of the Society of Materials Science, Japan*, 48(9Appendix), 202-205.

Yue, S. Y., Ouyang, T., and Hu, M. (2015). “Diameter Dependence of Lattice Thermal Conductivity of Single-Walled Carbon Nanotubes: Study from Ab Initio.” *Sci. Rep.*, 5(October), 1–8.

Zhang, H., Zhang, N., and Fang, F. (2020). “Fabrication of high-performance nickel/graphene oxide composite coatings using ultrasonic-assisted electrodeposition.” *Ultrason. Sonochem.*, 62, 104858.

Zhang, P., Cai, Z., & Xiong, W. (2007). "Influence of Si content and growth condition on the microstructure and mechanical properties of Ti–Si–N nanocomposite films." *Surface and Coatings Technology*, 201(15), 6819-6823.

Zhou, S. M., Zhang, X. B., Ding, Z. P., Min, C. Y., Xu, G. L., & Zhu, W. M. (2007). "Fabrication and tribological properties of carbon nanotubes reinforced Al composites prepared by pressureless infiltration technique." *Composites Part A: Applied Science and Manufacturing*, 38(2), 301-306.

BIO-DATA

Name: K Divya Bharathi
Father's Name: K. Venkat Swamy
Mother's Name: K. Prameela
Date of Birth: 24-06-1992
Nationality: Indian
Marital Status: Married



Permanent Address:

Flat No. G-4, Srishti Heights, Narsingi Village, Gandipet Mandal, Rangareddy District,
Hyderabad, Telangana -500089

Contact Details: Mobile Number: +91-9581138322, 9959514361

E-mail id: k.divya.212@gmail.com

Academic Qualification:

Master of Technology (Research) in Metallurgical and Materials Engineering from
National Institute of Technology Rourkela, Rourkela, Odisha, India (2016)

Bachelor of Technology in Metallurgical and Materials Engineering from Mahatma
Gandhi Institute of Technology (Affiliated to JNTU Hyderabad), Gandipet, Hyderabad,
Telangana, India (2013)

Research Publications:

Articles in International Journals: 02

Articles in Conference Proceedings: 02